University of Alberta

Refractometric sensing with fluorescent-core microcapillaries

by

C. P. Kyle Manchee

A thesis submitted to the Faculty of Graduate Studies and Research
in partial fulfillment of the requirements for the degree of

Master of Science

Department of Physics

Abstract

A capillary-type fluorescent-core microcavity refractive index sensor based on whispering gallery mode (WGM) resonances is presented. The device consists of a glass microcapillary with a thin layer of fluorescent silicon quantum dots (QDs) coated on the channel surface. The high index of the QD layer confines the electric field near the capillary channel and causes the development of WGMs in the fluorescence spectrum. Refractometric sensing was achieved in these fluorescent-core microcapillaries (FCMs) by pumping aqueous sucrose solutions through the capillary while measuring the fluorescence WGMs with a spectrometer. A finite-difference frequency-domain model was developed and used to study the performance of the FCMs. While the observed refractometric sensitivity and detection limit of the current device were inferior to competing technologies, FCMs offer other practical advantages, such as straight-forward fabrication, robust samples, and minimal instrumental requirements, all of which make FCMs an appealing technology for integration with lab-on-a-chip devices.

Acknowledgements

My time in Edmonton at the University of Alberta has been a very special experience. Over the past two years I have seen some wonderful parts of this country and had experiences that will stay with me for a long time. There are many people in my life who have helped make this experience as memorable as it has.

First I would like to thank my supervisor, Dr. Al Meldrum. He has been encouraging, patient, engaging, and truly helpful throughout my entire time here. I am very grateful to have had the privilege to work under his guidance. Next, I would like to thank all of my past and present lab-mates Ross Lockwood, Shalon McFarlane, Josh Silverstone, Yanyan Zhi, Dr. Vanessa Zamora, and Dr. Pablo Bianucci. Your expertise has helped me grow as a researcher, but more importantly you made it fun to come into work every day. What an awesome group. I wish you all the very best in your future endeavours (some coming sooner than others). Thank you to my "chemical" collaborator Dr. Jon Veinot, and his entire group, for making me feel welcome in the lab, on group outings, and in extra curriculars. In particular, I would like to thank (soon to be Dr.) Jose Rodriguez who taught me everything I know about cleaning, drying, and dipping small pieces of glass. My work would be nothing without your help. Thanks to Xiongyao Wang for TEM work and Nakeeran Ponnampalam for assistance with ellipsometry. A big thank you to technicians Don Mullins and Tony Walford who helped get my experiments up and running. Thank you to Alberta Innovates and the Natural Sciences and Engineering Research Council of Canada for funding this research.

My "co-workers" and friends here in Edmonton deserve a special thank you. Shawn Compton, Amelia Walker, Mike Reid, Laura Poole, Marco Taucer, Dr. Joel Kelly, Melanie Hoffman, Nick Arkell; whether it was on (many) ski trips, at shows and festivals, over a coffee, and probably a few beer, the time I have spent with you only enriched my life.

To my "long distance" support crew, my family and friends back in Ontario, thank you for staying with me through the years. My parents Penny and Philip, and sisters Jess and Hailey, are the most supportive and loving family one could hope for. I just wish we weren't so far away, but at least that makes for some incredible visits. Finally, and most importantly, I would like to thank my partner Sarah Regli. As a friend, co-worker, collaborator, supporter, and confidant you have helped me get through two degrees. It's been one hell of an adventure; I can't wait for the next chapter!

Contents

List of Tables

List of Figures

List of Abbreviations

CCD	charge-coupled device
DL	detection limit
DOS	density of states
EM	electromagnetic
FCM	fluorescent-core microcapillary
FDFD	finite-difference frequency-domain
FDTD	finite-difference time-domain
FSR	free spectral range
FWHM	full-width at half-maximum
HPS, sHPS	HSQ precursor solution, s = stock
HSQ	hydrogensilsesquioxane
ID	inner diameter
LCORR	liquid-core optical ring resonator
LED	light-emitting diode
LOC	lab-on-a-chip
MIBK	methyl isobutyl ketone
NC	nanocrystal
PE	polythylene (tubing)
PL	photoluminescence
POC	point-of-care
QD	quantum dot
RIU	refractive index unit
RS	refractometric sensitivity
SEM	scanning electron microscopy
SERS	surface enhanced Raman spectroscopy
SGS	self-guiding spectrograph
Si-NC	silicon nanocrystal
SPR	surface plasmon resonance

SPW	surface plasmon wave
TE_z	transverse electric
TEM	transmission electron microscopy
TIR	total internal reflection
TM_z	transverse magnetic
Type-II	FCM with capillary inner diameter $100\,\mu$m
Type-I	FCM with capillary inner diameter $25\,\mu$m
VASE	variable angle spectroscopic ellipsometry
WGM	whispering gallery mode

List of Symbols

a_B	Bohr exciton radius
β	WGM axial propagation constant
$B_{\lambda,T}(\lambda)$	black body intensity
c	speed of light in vacuum $= 2.99792458 \times 10^8\,\mathrm{m/s}$
C	molar concentration
d	film thickness, also d_f
ε_0	permittivity of free space $= 8.85418782 \times 10^{-12}\,\mathrm{F/m}$
ε_r	relative permittivity of material
E_g	band gap energy
$\mathbf{E}$	electric field
γ	Lorentzian linewidth
$\gamma(\nu)$	variable Lorentzian linewidth
h	Planck's constant $= 6.62606957(29) \times 10^{-34}\,\mathrm{J \cdot s}$
$\hbar$	reduced Planck constant $= 1.054571726(47) \times 10^{-34}\,\mathrm{J \cdot s}$
$\mathbf{H}$	magnetic field
$H_l^{(1)}(x)$	Bessel function of the third kind
$I(\nu)$	spectral lineshape
$I_{\lambda,T}(\lambda)$	Planck's law of blackbody radiation intensity
$J_l(x)$	Bessel function of the first kind
$k, \mathbf{k}$	wavenumber, wavevector
κ	extinction coefficient
l	WGM azimuthal number
λ	wavelength
m	mass

M	molar mass
n	refractive index
$\tilde{n}$	complex refractive index, $\tilde{n} = n + i\kappa$
ν	frequency
Q	quality factor
r	radius, or radial parameter
$r_{\perp,\parallel}$	reflection coefficient
ρ	WGM radial number
$R_{\perp,\parallel}$	power reflection coefficient
$S(\lambda),\ S(\nu)$	spectral intensity
t	time
$t_{\perp,\parallel}$	transmission coefficient
T	temperature
$T_{\perp,\parallel}$	power transmission coefficient
θ_c	total internal reflection critical angle
v	phase velocity
V	volume
ω	angular frequency
W	mass fraction (weight percent $= W \times 100\%$)

Chapter 1

Introduction: Microfluidic sensing for lab-on-a-chip technologies

1.1 The need for integrated microscale sensors

As the natural environment of many biological and chemical systems, the fluidic-phase (liquid and/or gas) is a desirable platform for experimentation, facilitating both *in vitro* and *in vivo* studies. Accordingly, a vast array of analytical techniques, including chromatography (gas phase and high pressure liquid phase), voltammetry, spectroscopy, and microscopy, have been developed or adapted to manipulate, detect, and analyze samples in the gas or liquid phase. And, while many such techniques are commonly used to analyze samples with volumes on the order of millilitres—a natural and convenient volume scale to work with— there has been much emphasis over the past half-decade to develop or expand analytical techniques that have the capacity to sample volumes one thousand to one million times smaller; such is the field of microfluidics.

Microfluidics, as a field, deals with the handling of small amounts of fluids, typically microlitres or nanolitres, and encompasses all aspects of such systems including devices, controls, fluid transport, and physical phenomena [1, 2]. Though some novel research is undoubtingly conducted in fundamental microfluidic techniques, microfluidics is more commonly viewed and referred to as a tool or platform used to aid in the development and research of other chemical and biological systems. It has its roots in the 1950s, when, as part of the development of inkjet printing, there was a significant push to develop techniques

for dispensing small amount of liquids [3].

Today the use of microfluidics is far more widespread. Though the fields and applications can be vastly different, the underlying premise of a microfluidic system is fairly straightforward. Typically, analyte fluids are guided through a small chip via a series of micro-channels (Fig. 1.1). Such chips (often only a few cm^2 in size) and channels ($\sim 1 - 1000\,\mu$m in width) are fabricated using microfabrication and lithography techniques from a variety of materials, including glass, silicon, organic or inorganic polymers such as polydimethylsiloxane, and metals (typically used as electrodes) [4, 5]. Depending on the application, the chip may be designed to mix, treat, react, or otherwise probe the analyte fluids. After this function is complete, the final product is "read-out" or detected. This essentially shrinks a "bench top" experiment down to the micron scale. A significant breakthrough in microfluidics occurred in 1979 with the development of a miniaturized on-chip gas chromatograph by Terry *et al.* [6] at Stanford University. For the first time, a complex chemical analysis, usually performed by a large machine, was executed on a single 5 cm silicon chip. This would become known as the first lab-on-a-chip (LOC) device.

18 mm
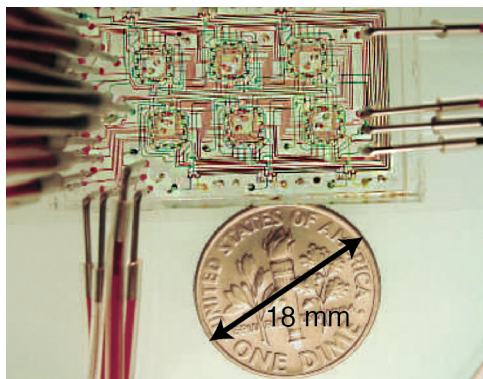
Figure 1.1: Microfluidic devices can incorporate hundreds of fluidic channels and mixing chambers on a single chip a few centimeters in size. The device pictured was used to study the growth of microbial populations. The colour contrast comes from dyes which have been pumped through the fluidic pathways. Modified from Ref. [7].

While most chemical and biological processes and interactions remain unchanged when scaled down to this size, some physical properties and phenomena do change. As a result, microfluidic systems offer several benefits and opportunities. The most obvious benefit is the ability to sample small fluid volumes [8]. This enables testing in situations where only a small amount of sample exists, such as in many forensic applications, and when the sample is very expensive or precious. Often, the cost of testing and the amount of chemical waste

is greatly reduced. Other benefits include an increased surface-area-to-volume ratio, which increases the degree of interaction of the analyte with the system surface, allowing for rapid heating and cooling and precise regulation of reaction conditions [4, 5, 9], laminar flow, *i.e.,* flow without mixing,[1] and multiplexing or parallelization [8, 11]. Parallelization allows for the testing of hundreds or thousands of analyte combinations at once, and has become important in the field of drug development where thousands of combinations of drugs must be tested individually. Such testing is difficult and time consuming to perform serially, but the use of a microfluidic chip could enable complete analyses to be performed in the time of a single experiment [10].

The successful miniaturization of experiments using microfluidic systems—facilitated by the rapid progression of microfabrication techniques, the same technology which has enabled the development of MEMS devices in accordance with Moore's law [12]—has stimulated interest in further integrating all aspects of a laboratory onto a single chip. The goal of LOC devices is to extract the components of a full laboratory that are necessary in performing a specific function or test, and miniaturize them onto a single autonomous unit [13, 14]. LOC devices enable analyte treatment, manipulation and processing, detection, and even signal readout without necessitating a formal laboratory setting or highly trained personnel. As such, LOC devices are of interest in areas of biomedical diagnostics and testing as they can provide state-of-the-art analysis at a fraction of the cost, and in a fraction of the time required for laboratory analysis. This enables the use of LOC-based devices for point-of-care (POC) monitoring and early detection of diseases, including cancers, and to aid in health-care monitoring and delivery to remote areas and communities, where it would be otherwise unavailable [15, 16]. Indeed, several first-generation LOC devices are commercially available and more are on the horizon [17].

A significant hurdle in the development of LOC devices is the incorporation of microscale sensors and detectors that can provide adequate sensitivity and resolution, and that are compatible with the microfluidic system. Of particular interest are those which can detect the presence and/or concentration of biomolecules, since such sensors can be integrated into LOC devices serving the high-profile fields of biohazard detection, public heath, biosecurity, and food safety.

---

[1]More precisely, mixing is diffusion-limited on the micro-scale [10].

1.2 Traditional optical sensing on the microscale

One of the greatest advantages of LOC/microfluidic devices also gives rise to one of the greatest challenges in biomolecular detection: small sample volumes. The reduction in sample volume leads to fewer analyte molecules interacting with the detection system, resulting in decreased detector signal and low sensitivity. This causes electrochemical detection methods such as potentiometry to be ineffective for many LOC applications.[2] Mass spectrometry, a popular analytic technique on the macroscale, generally requires expensive equipment and is not straight-forward to miniaturize to LOC scales, inhibiting the development of a portable, self-contained device [19]. Optical transduction has emerged as an appealing group of methods for biomolecular sensing, providing benefits such as rapid detection, natural scalability to small dimensions, non-destructive sampling, high throughput capabilities, and microfabrication/microfluidic compatibility [20, 21]. Several structures and methods are being explored for microfluidic optical sensing, including labelled fluorescence, surface plasmon resonance devices, surface enhanced Raman spectroscopy, anti-resonant reflection optical waveguides, interferometers, micro-chromatographs, and optofluidics [22–26].

1.2.1 Labeled fluorescence detection

Fluorescence detection involves the use of a fluorescent molecule (*i.e.*, fluorophore) as an indicator for the target molecule. The interaction of the fluorophore and target molecule may be passive or active. That is, the fluorophore may actively bond to the target molecule and the fluorescence intensity from the sample can be calibrated to the concentration of the target molecule. Alternatively, the target molecule may alter the fluorescence of the fluorophore, resulting in an enhancement, quenching, or other modification that can be calibrated to its concentration in the solution [27]. A significant degree of sample processing is often required for the labeling of a target molecule with a fluorophore [28]. While such processing creates a high degree of specificity in the detection, it can also make fluorescence detection unfeasible for some LOC applications, as the required sample preparation is difficult to achieve on-chip, outside the laboratory. Ideally, sensors not requiring chemical labeling are preferred. As a result, fluorescence detection is attractive for applications involving naturally fluorescing species [29].

Due to its high signal-to-noise ratio, the most common form of fluorescence detection is

---

[2]There are some important exceptions including a hand-held blood glucose detector, CoaguChek, from Roche Diagnostics [18].

laser-induced fluorescence, where a laser is used as the excitation source for the fluorophore. However, LED-based fluorescence detectors are an attractive alternative as they require low operating powers, can be naturally compact in size, making them easy to integrate into LOC devices, and they are inexpensive. Photomultiplier tubes (PMTs) are commonly used in the field of fluorescence detection, allowing for good sensitivity to low light levels. However, PMTs do not readily permit spatially resolved measurements, nor do they scale well for on-chip detection. On-chip fluorescence detection has also been demonstrated using highly sensitive charged-coupled device (CCD) arrays [30,31]. Due to its high selectivity and ability to perform sensitive measurements, fluorescence is the most widely used detection system in microfluidics, and is one of the most studied for LOC applications [20].

1.2.2 Surface plasmon resonance

Surface plasmons (SPs) are electronic oscillations that can occur at the interface of a metal and a dielectric (Fig. 1.2a). When excited with light, SPs are referred to as surface plasmon waves (SPWs) or surface plasmon polaritons (SPPs). SPWs are transverse-magnetic (TM) waves that propagate along the interface with the propagation constant, β, expressed as

$$\beta = \frac{\omega}{c}\sqrt{\frac{\varepsilon_M \varepsilon_D}{\varepsilon_M + \varepsilon_D}} \tag{1.1}$$

where ω is the angular frequency, c is the speed of light (in vacuum), and ε_M and ε_D are the dielectric functions of the metal and dielectric, respectively. In order to sustain a SP it is required that ε_M is negative, and larger in magnitude than ε_D; this condition is satisfied at optical wavelengths for a variety of metals, most commonly gold [32–34]. Due to their localization at the metal–dielectric interface, SPWs are highly sensitive to perturbations at the boundary surface, *e.g.,* a binding event or change in the refractive index of the dielectric. Surface plasmon resonance (SPR) relies on monitoring frequency-shifts in the reflectivity spectrum which occur as a result of these perturbations. SPR is not an inherently selective detection method; any perturbation to the boundary will result in an SPR shift. This is a result of the fact that SPR is sensitive to the effective refractive index of the two layers and not to any specific interaction with the molecule being analyzed. Experimentally, precautions must be taken to ensure that no secondary perturbations, *i.e.* unexpected binding or change in solvent, affect the SPR signal [35].

In terms of biomolecular sensing SPR is the "gold standard" for laboratory applications,
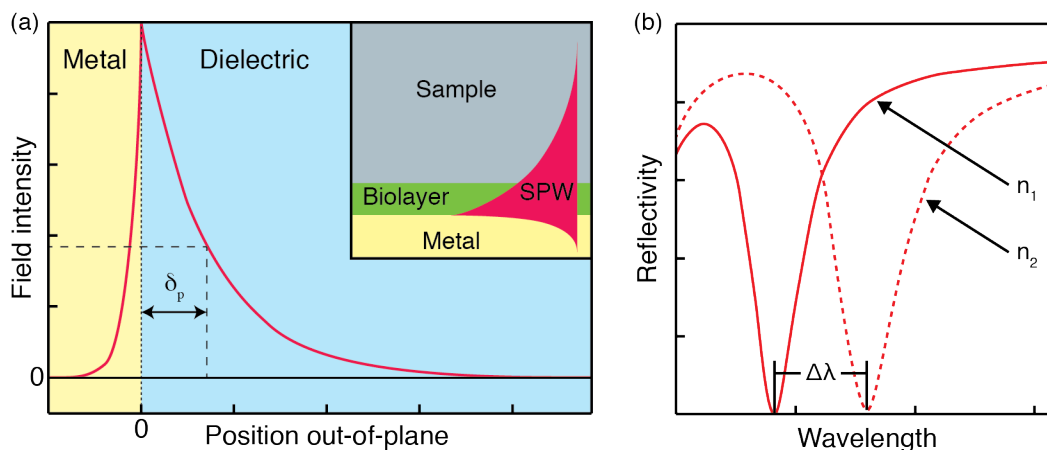
Figure 1.2: Surface plasmon waves can form at the boundary between a metal and dielectric. (a) The electromagnetic field decays exponentially into the materials, characterized by the penetration depth δ_p (typically $100-500$ nm). *Inset* Sensing occurs near the metal-dielectric interface. (b) SPR measurements are obtained by measuring the sample reflectance as a function of wavelength (depicted) or incident angle. Changes to the sample cause a shift the in the reflectance spectrum. Reproduced from Ref. [34].

owing mostly to its versatility with respect to analyte species and speed of analysis [34]. SPR possesses the ability to measure kinetic rate/equilibrium constants, and provides direct, fast (near real-time) detection; however, these advantages have not yet been exploited in LOC/POC devices. In fact the incorporation of SPR into LOC and POC devices has been, in general, slow, as current commercial SPR instruments are too large and expensive for LOC integration [35]. Some SPR-based LOC biomolecular detection devices have been demonstrated [35, 36], and the future of SPR in the field of LOC and POC devices is promising.

1.2.3   Surface enhanced Raman spectroscopy

Raman scattering is the elastic and inelastic scattering of light through virtual states (having short lifetimes) of a molecule. When monochromatic light (usually laser light) is shone on a molecule most of the absorbed light is elastically scattered, *i.e.* at the same wavelength as the source. However, a small amount of light is inelastically scattered at wavelengths governed by the vibrational energy states of the molecule. This inelastic Raman scattering can result in both a red shift (Stokes) and blue shift (anti-Stokes) of the incident light [37]. The resulting Raman spectrum is somewhat like a "fingerprint" of the molecule's vibrational energy space, meaning that the technique is selective towards to targeted molecules. However, the inelastic Raman scattering cross-section is too small to provide highly sensitive

detection in LOC devices, as the generated Raman signal is simply too weak [38, 39]. This issue was somewhat reconciled in the 1970's upon the discovery that the Raman signal is significantly enhanced when the target molecule is in contact with a rough metallic surface. This process is known as surface enhanced Raman scattering; the corresponding spectroscopic technique is known as surface enhanced Raman spectroscopy (SERS). The choice of surface material (referred to as the SERS-active material, or SERS enhancer) depends on a large number of parameters including the plasmon resonance frequency. Silver and gold, which are SERS active at visible and near-IR frequencies, are popular choices, silver colloids or nanoclusters, in particular. SERS can generate signals up to 10^{14} [39] times stronger than its traditional Raman counterpart and has been used to demonstrate single-molecule detection [40].

A number of SERS-based microfluidic biomolecular detectors have been recently demonstrated [25, 38, 39, 41, 42], however several notable challenges with SERS-based detection on the microscale have become evident. First and foremost is the low reproducibility of SERS measurements, stemming primarily from the inability to effectively mix (*i.e.,* bind) the analyte with the SERS enhancer—mixing is a common issue in microfluidic systems. This also leads to slow detection times, which are on the order of a few minutes. For these reasons, much research in the field of microfluidic SERS-based detection is focused on achieving rapid, reproducible mixing of the analyte with the SERS active surface.

1.3 Sensing with Optical Cavities

1.3.1 Optical cavities and whispering gallery modes

A fundamental challenge with optical sensing on the microscale is the limited sensitivity and detection limit, due to the low signals (from small sample volumes) and small interaction paths lengths (from small dimensions). One method to overcome this uses an optical resonant cavity to provide a multi-pass detection system. Photons in the cavity are confined, circulating typically $10^3 - 10^9$ times prior to detection, allowing for increased interaction with the analyte and, ultimately, higher sensitivity. Optical microcavities are widely investigated in the field of quantum optics and are available in a wide range of structures via a number of different fabrication techniques.

One metric of an optical microcavity is the quality (Q) factor, defined in terms of the

energy stored vs. the energy dissipated per cycle:

$$Q = 2\pi \frac{energy\,stored}{energy\,dissipated} \tag{1.2}$$

which, assuming a Lorentzian peak shape, is equivalently defined as

$$Q = \frac{\nu_0}{\Delta\nu} \tag{1.3}$$

where ν_0 is the resonant frequency of the cavity, and $\Delta\nu$ is the full-width at half-maximum (FWHM) of the resonance. Q can also be defined in terms of the complex frequency of the resonant mode:

$$Q \equiv \frac{Re(\omega)}{2|Im(\omega)|} = \frac{Re(k)}{2|Im(k)|} = \frac{Re(\nu)}{2|Im(\nu)|} \tag{1.4}$$

The Q-factor is an approximate of measure of the number of times an on-resonance photon circulates the cavity prior to emission. In general, the observed Q-factor is a result of several loss mechanisms, such as radiative losses, material losses, and scattering:

$$\frac{1}{Q} = \frac{1}{Q_{rad}} + \frac{1}{Q_{mat}} + \frac{1}{Q_{scat}} + \sum_i \frac{1}{Q_i} \tag{1.5}$$

where Q_{rad} is the radiative Q-factor and defined in Eq. (1.4). Q_{mat} is the material-limited Q-factor, given by the complex refractive index of the propagation material:

$$Q_{mat} = \frac{n}{2|\kappa|} \tag{1.6}$$

where $\tilde{n} = n + i\kappa$ is the complex refractive index of the material. The summation term in Eq. (1.5) represents contributions from all other loss mechanisms.

A particularly promising group of microcavity resonators are those that use whispering gallery mode (WGM) recirculation to confine light in the cavity. WGMs are named after their acoustic analogue, famously observed in St. Paul's cathedral in London and first explained by Lord Rayleigh [43]. They are low-loss optical resonances that circulate around circular or spherical cavities via total internal reflection (TIR). WGMs in optical microcavities can have Q-factors as high as 10^9 [44], meaning light circulates the cavity hundreds of millions of times, increasing the interaction path length from microns (single pass) to kilometers! Due to the nature of TIR, WGMs propagate along a boundary between

two dielectric materials, mostly confined in the high-refractive index material, but with an evanescent tail that decays exponentially into the low-index material. For example, consider a glass sphere ($n_s \simeq 1.45$) submerged in water ($n \simeq 1.33$): WGMs may propagate along the equator of a glass sphere, with an evanescent tail extending into the water. These WGMs are sensitive to changes in refractive index near the propagation boundary.

1.3.1.1   Total internal reflection[3]

When treated as a wave, light is the coupled oscillations of orthogonal electric and magnetic fields (Fig. 1.3a), known as an electromagnetic (EM) wave. When propagating through a material, light interacts with electric dipoles in the material and is, in general, slowed. The refractive index, n, is a bulk property which relates the speed of light in a material relative to the speed of light in vacuum:

$$ n = \frac{c}{v} \tag{1.7} $$

where v is the speed of light in the material[4] and $c = 2.997925 \times 10^8$ m/s is the speed of light in vacuum. By definition, the refractive index of a vacuum is unity, and most everyday materials have $n > 1$.[5] The refractive index is related to the relative permittivity ε_r and permeability μ_r of the material:

$$ n = \sqrt{\varepsilon_r \mu_r} \tag{1.8} $$

And the relative permittivity relates the electric displacement field **D** to the electric field **E** and material polarization **P**:

---

[3]Some of the material in this section can be found in undergraduate level Electrodynamics or Optics textbooks, such as [45–49], but is helpful for a full description of WGMs.

[4]Here, v is actually the phase velocity (v_p) of light in the medium.

[5]In fact, depending on the material and wavelength, n can be less than one. In this case the phase velocity of the light is greater than c. However, information in the wavepacket of light travels at the signal velocity, which is always less than c, thus maintaining the law of relativity. For cases of low dispersion (*i.e.* n changes slowly with wavelength) the signal velocity is equivalent to the group velocity of the wavepacket ($v_g \equiv \frac{\partial \omega}{\partial k} |_{\omega=\omega_0}$), which can be approximated as

$$ v_g = v_p - \lambda \frac{dv_p}{d\lambda} $$

or

$$ v_g = \frac{c}{n_g} $$

where n_g is the group refractive index, and is given by

$$ n_g = \frac{n}{1 + \frac{\lambda}{n} \frac{dn}{d\lambda}} $$

where n is the "classical" refractive index of the material (see Eq. 1.7).

$$\mathbf{D} = \varepsilon_0\mathbf{E} + \mathbf{P} = \varepsilon_r\varepsilon_0\mathbf{E} \qquad (1.9)$$

where ε_0 is the vacuum permittivity. And the relative permeability relates the magnetic $\mathbf{B}$ and $\mathbf{H}$ fields:

$$\mathbf{B} = \mu_r\mu_0\mathbf{H} \qquad (1.10)$$

where μ_0 is the vacuum permeability. For most materials $\mu_r \cong 1$, and $n \cong \sqrt{\varepsilon_r}$.
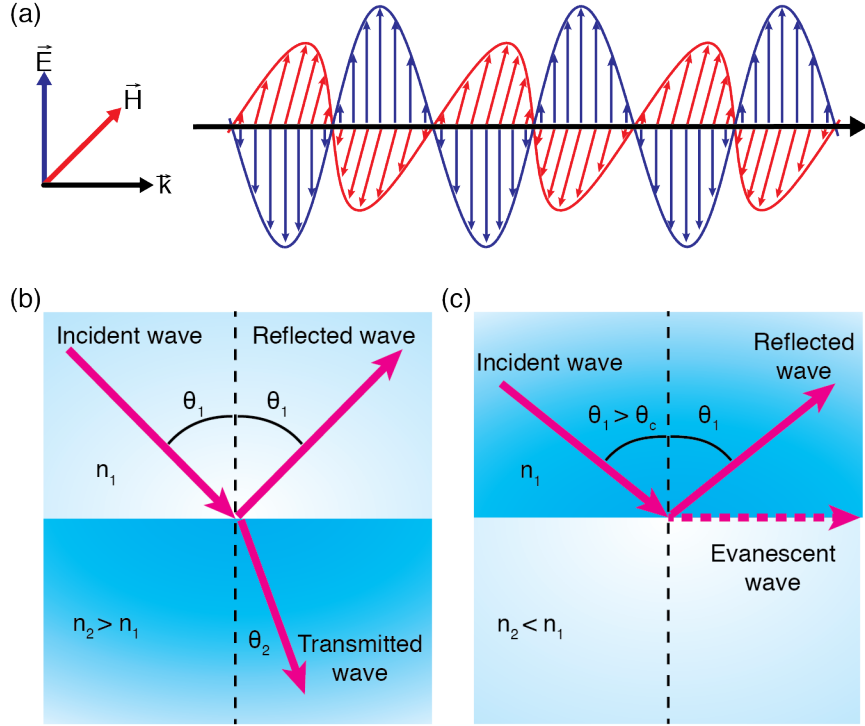
Figure 1.3: (a) Electromagnetic plane-wave. (b) Incidence at a dielectric boundary results in partially reflected and transmitted waves. The relative intensities of the waves is dependent on the refractive indices of the materials. (c) Total internal reflection. Under special circumstances the wave is entirely reflected, with no transmission. An evanescent wave travels along the boundary.

Consider an x-polarized plane wave propagating through a material, refractive index n_1, with electric and magnetic field components

$$\mathbf{E}(\mathbf{r}, t) = Re[\mathbf{E_0}(\mathbf{r})\exp\{i(\omega t - \mathbf{kr} + \phi)\}] \qquad (1.11)$$

$$\mathbf{H}(\mathbf{r}, t) = Re[\mathbf{H_0}(\mathbf{r})\exp\{i(\omega t - \mathbf{kr} + \phi)\}] \qquad (1.12)$$

$$
\begin{aligned}
\mathbf{E_0, H_0} &= complex\ field\ amplitude\ vectors \\
\omega &= angular\ frequency \\
\mathbf{k} &= wavevector\ (|\mathbf{k}| = k = wavenumber) \\
\phi &= phase
\end{aligned}
$$

and the wavelength of the light in the material is given by

$$
\lambda = \frac{\lambda_0}{n_1} = \frac{2\pi}{k} = \frac{2\pi}{\omega}\frac{c}{n_1} = \frac{1}{n_1}\frac{c}{\nu} \tag{1.13}
$$

where ν is the frequency of the EM wave. Now consider this wave arriving at incidence to a dielectric boundary—a boundary between two materials of different refractive index, such as glass and air. Part of the wave's energy will be transmitted into the second material, while some energy will be reflected back into the first material (Fig. 1.3b). The relative amplitudes of the reflected and transmitted waves depend on both the polarization of the EM wave (*i.e.* the direction in which the E-field oscillates, either parallel or perpendicular to the incident plane) and the angle at which the wave strikes the boundary; they are described by a set of equations, known as the **Fresnel Equations**:

$$
\begin{aligned}
r_\perp &= \frac{E_{r\perp}}{E_{0\perp}} = \frac{n_1\cos\theta_1 - n_2\cos\theta_2}{n_1\cos\theta_1 + n_2\cos\theta_2}, & t_\perp &= \frac{E_{t\perp}}{E_{0\perp}} = 1 + r_\perp & (1.14) \\
r_\parallel &= \frac{E_{r\parallel}}{E_{0\parallel}} = \frac{n_1\sec\theta_1 - n_2\sec\theta_2}{n_1\sec\theta_1 + n_2\sec\theta_2}, & t_\parallel &= \frac{E_{t\parallel}}{E_{0\parallel}} = (1 + r_\parallel)\frac{\cos\theta_1}{\cos\theta_2} & (1.15) \\
R_i &= |r|_i^2 & & & (1.16) \\
T_i &= 1 - R_i & & & (1.17)
\end{aligned}
$$

where R and T are the relative reflection and transmission powers[6], respectively, n_1 and n_2 are the refractive indices of first and second material, respectively, θ_1 is the incident/reflection angle, and θ_2 is the transmission angle, given by **Snell's Law**:

$$
\cos\theta_2 = \sqrt{1 - (n_1/n_2)^2 \sin^2\theta_1} \tag{1.18}
$$

---

[6]Note that in the particle formulation of light, R and T represent probabilities that an incident photon will be reflected or transmitted, respectively.

Equation (1.18) yields a peculiar effect in the case that $n_1 > n_2$: beyond some critical angle θ_c, the term $(n_1/n_2)^2 \sin^2 \theta_1$ becomes greater than one, yielding a purely complex result for $\cos \theta_2$. At this critical angle, when $\sin \theta_c = \frac{n_2}{n_1}$, substitution into Eqs. (1.14–1.17) reveals that the entire wave is reflected: $R = 1$, $T = 0$ (Fig. 1.4). This effect is called total internal reflection (TIR) and results in the confinement of light in the high-index material (Fig. 1.3c). When this occurs the entire EM wave is reflected back into the first, high-index material, however, since the EM field is not necessarily zero at the boundary and cannot discontinuously jump to zero, the EM field decays exponentially into the second, low-index material. This exponential decay is known as the evanescent wave. Evanescent waves are used for a number of applications including the coupling to optical microcavities.
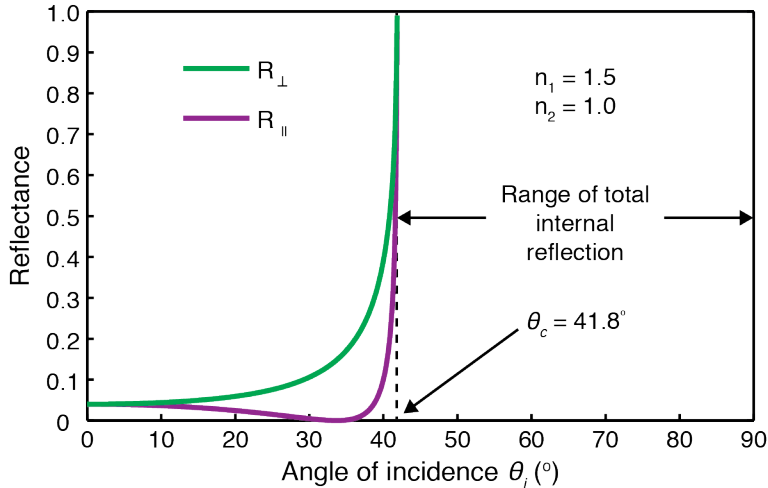
Figure 1.4: Reflection coefficients $R_\perp$ and $R_\parallel$ for a plane wave incident (incidence and θ_i) on a dielectric boundary ($n_1 = 1.5$, $n_2 = 1.0$). Total internal reflection occurs for incidence angles greater than the critical angle $\theta_c = 41.8°$.

1.3.1.2 Analytical evaluation of whispering gallery modes in cylindrical structures

In this section, we will give a basic overview of the origin and structure of WGMs, which will be helpful when we describe the experimental results. For further information on solving the optical modes of resonant cavities and waveguides refer to one of many electrical engineering/fiber optics or electromagnetic theory textbooks, such as [49–51].

As noted before, WGMs are optical resonance modes that propagate around cavities with circular or spherical symmetry via TIR. In 2D, simply enforcing a periodic resonance condition, ensuring constructive interference upon a round trip of the structure, yields an

intuitive expression for the WGMs in a circular resonator:

$$l\frac{\lambda_l}{n} = 2\pi r \tag{1.19}$$

where $\frac{\lambda_l}{n}$ is the wavelength of the resonant mode in the material (λ_l is the free space wavelength), r is the radius of the resonator, and l is an integer (*i.e.*, the resonance order). While useful for identifying simple trends, Eq. (1.19) fails to consider the nature of the light propagation and the influence of the structure and boundaries on the WGM resonances. These resonances are more accurately obtained by solving Maxwell's equations in the appropriate coordinate system and applying dielectric boundary conditions in accordance with the desired structure. This method has been applied to both spherical [52] and cylindrical structures [50, 51]. In this section an infinite cylinder will be considered as it is applicable to both optical fibres and capillaries to be described in the experimental section.

Whispering gallery modes in cylindrical structures   Consider a long cylinder with its axis along the $\hat{\mathbf{z}}$ direction. In cylindrical coordinates (r, ϕ, z), the z-components of the EM field can be written as

$$F_z(r, \phi, z) = A(r)e^{im\phi}e^{i(\omega t - \beta z)} \tag{1.20}$$

where F_z is either E_z or H_z, m is an integer, and β is a propagation constant along the cylinder axis. $A(r)$ is an arbitrary function, depending only on the variable r. The four other field components (E_r, E_ϕ, H_r, H_ϕ) can be determined explicitly from derivatives of E_z and H_z and need not be considered here (*i.e.* once expressions for E_z and H_z are obtained, so are expressions for the rest of the field components). Equation (1.20) can be reasoned intuitively, since the EM field is free to propagate down the cylinder, but must be periodic around the cylinder ($2\pi\phi$). Since we want only to consider bound modes of the cylinder, we let $\beta = 0$, leaving only circularly propagating modes, *i.e.* WGMs. Solving Maxwell's equations under these conditions yields the partial differential equation:

$$\frac{\partial^2 \mathbf{F}}{\partial r^2} + \frac{1}{r}\frac{\partial \mathbf{F}}{\partial r} + \frac{1}{r^2}\frac{\partial^2 \mathbf{F}}{\partial \phi^2} + k^2 \mathbf{F} = 0 \tag{1.21}$$

which is the Helmholtz equation. Here $\mathbf{F} = F_z(r, \phi, z)$, and $k^2 = \omega^2 \varepsilon \mu = \omega^2 \frac{n^2}{c^2}$, where n is the refractive index of the material. Taking the appropriate derivatives of $\mathbf{F}$ (refer to Eq.

13

(1.20)) yields the differential equation

$$\frac{d^2 A(r)}{dr^2} + \frac{1}{r}\frac{dA(r)}{dr} + \left(k^2 - \frac{m^2}{r^2}\right) A(r) = 0 \qquad (1.22)$$

which is the well known Bessel equation, with solutions

$$A(r) = \gamma Z_m(kr) \qquad (1.23)$$

where γ is a constant and $Z_m(kr)$ can be any of a number of Bessel functions. The z-dependent exponential factor in Eq. (1.20) was eliminated by setting $\beta = 0$, and the time- and ϕ- dependent factors $e^{i(\omega t + m\phi)}$ that multiply all the field components have been omitted in Eq. (1.22) as they do not influence the solutions of $A(r)$.

At this time we must consider the refractive index profile of the structure in question. The simplest case would be that analogous to an optical fiber, where

$$n = \begin{cases} n_1, & r < a \\ n_2, & r > a \end{cases}$$

and a is the radius of the fibre. However, for experimental reasons to be discussed in Sec. 1.3.2.2, we are going to imagine a slightly more complicated, three-layer structure, more closely analogous to a capillary, or a fibre with a film:

$$n = \begin{cases} n_1, & r < b \\ n_2, & b < r < a \\ n_3, & r > a \end{cases} \qquad (1.24)$$

where a and b are the outer and inner radii of the structure.[7]

Now, with our structure selected, we may choose which Bessel functions $(Z_m(kr))$ are appropriate. First, however, let us switch indices to a more conventional notation: $Z_m(kr) \to Z_l(kr)$. There are three linearly independent solutions to the Bessel equation: Bessel functions of the first $J_l(kr)$, second $Y_l(kr)$, and third $H_l^{(1,2)}(kr)$ kind. The Bessel

---

[7]Even more complicated is the case of a capillary with an internal film, which contained four layers. However, such detail is often unnecessary. In the case of a thick-walled capillary with a thin film [53], the walls of the capillary can be taken to extend to infinity, reducing the problem back to Eq. (1.24).

functions of the third kind, $H_l^{(1)}(kr)$ and $H_l^{(2)}(kr)$, also known as Hankel functions, are linear combinations of the first two types of Bessel functions that represent traveling waves away from, and towards the origin, respectively. In general, $A(r)$ is given by a linear combination of Bessel functions of the first and second kind, since they represent two linearly independent solutions to the Bessel equation .[8] However, some physical considerations can simplify the expression of $A(r)$.

For integer values of l (as is our case), only the Bessel functions of the first kind, $J_l(k_1 r)$, are finite at the origin $r = 0$ and so must be selected for this first region, $r < b$. Also, there is no EM source at $r = \infty$, thus solutions in the third region ($r > a$) should best be described by the outwards traveling wave $H_l^{(1)}(k_3 r)$. In the middle region, $b < r < a$, solutions will remain a linear combination of Bessel functions of the first and second kind; for consistency we will choose $J_l(k_2 r)$ and $H_l^{(1)}(k_2 r)$. The resulting expression for $A(r)$ is

$$A(r) = \begin{cases} C_1 J_l(n_1 kr) & r < b \\ C_2 J_l(n_2 kr) + C_3 H_l^{(1)}(n_2 kr) & b < r < a \\ C_4 H_l^{(1)}(n_3 kr) & r > a \end{cases} \tag{1.25}$$

where the C_i are constants. Note that we have switched variables for k; in Eq. (1.25) $k = k_0 = \frac{\omega}{c}$.

Maxwell's equations also govern how light behaves at a dielectric boundary, resulting in a set of equations defining boundary conditions that the field components must satisfy. Field components parallel to the plane of incidence are continuous across the boundary, whereas field components perpendicular to the plane of incidence are discontinuous by a factor of $\varepsilon_2/\varepsilon_1 \cong n_2^2/n_1^2$ for the E-field and $\mu_2/\mu_1 \cong 1$ for the H-field.

The solutions to Eq. (1.22) can be separated into two classes corresponding to the polarization of the EM wave; these classes are labelled TE_z and TM_z. Transverse-electric (TE_z) modes have the electric field polarized in the z-direction, *i.e.* transverse to the plane of the WGM. This requires that the field components $H_z = E_r = E_\phi = 0$. Conversely, transverse-magnetic (TM_z) modes have the magnetic field polarized in the z-direction, and so $E_z = H_r = H_\phi = 0$. When the boundary conditions described above are applied, TE_z and TM_z yield slightly different results. For consistency with the experimental data (Sec. 3.5), only TE_z modes will be considered. Applying the boundary conditions dictates that

---

[8]Since Hankel functions are linear combinations of the first and second type Bessel function, a linear combination of $J_l(kr)$ and $H_l^{(1)}(kr)$ is also a linear combination of $J_l(kr)$ and $Y_l(kr)$.

E_z and H_ϕ are continuous across the interfaces at both $r = a$ and $r = b$. This results in a system of four equations, linear in the coefficients C_1, C_2, C_3, and C_4, which can be solved in order to obtain the resonance wavenumber, k:

$$
\det
\begin{bmatrix}
J_l(n_1 kb) & J_l(n_2 kb) & H_l^{(1)}(n_2 kb) & 0 \\
J_l'(n_1 kb) & J_l'(n_2 kb) & H_l^{(1)\prime}(n_2 kb) & 0 \\
0 & J_l(n_2 ka) & H_l^{(1)}(n_2 ka) & H_l^{(1)}(n_3 ka) \\
0 & J_l'(n_2 ka) & H_l^{(1)\prime}(n_2 ka) & H_l^{(1)\prime}(n_3 ka)
\end{bmatrix}
= 0
\qquad (1.26)
$$

where the prime (') indicates a derivative with respect to the entire Bessel function argument. Due to the nature of the Bessel functions an exact analytical expression cannot be obtained. However, the WGM resonance can be estimated numerically by calculating Eq. (1.26) over the complex solution space of k and finding the zeros of the resulting function. The value of Eq. (1.26) for complex values of k is plotted in Fig. 1.5a. The location of each minimum (highlighted) represents the complex frequency of a WGM. For a given set of initial parameters l, a, b, n_1, n_2, and n_3 there exists an infinite number of solutions to Eq. (1.26), each with a different number of field intensity maxima in the radial direction ($\hat{r}$) (see Fig. 1.5b). Furthermore, we can see from Eq. (1.20) that l represents the number of field amplitude maxima in the azimuthal ($\hat{\phi}$) direction. Thus, in addition to the polarization, WGMs in cylindrical structures can be fully characterized using two quantum numbers: ρ, defined to be the number of field intensity maxima in the radial direction, and l, the number of field amplitude maxima in the azimuthal direction.
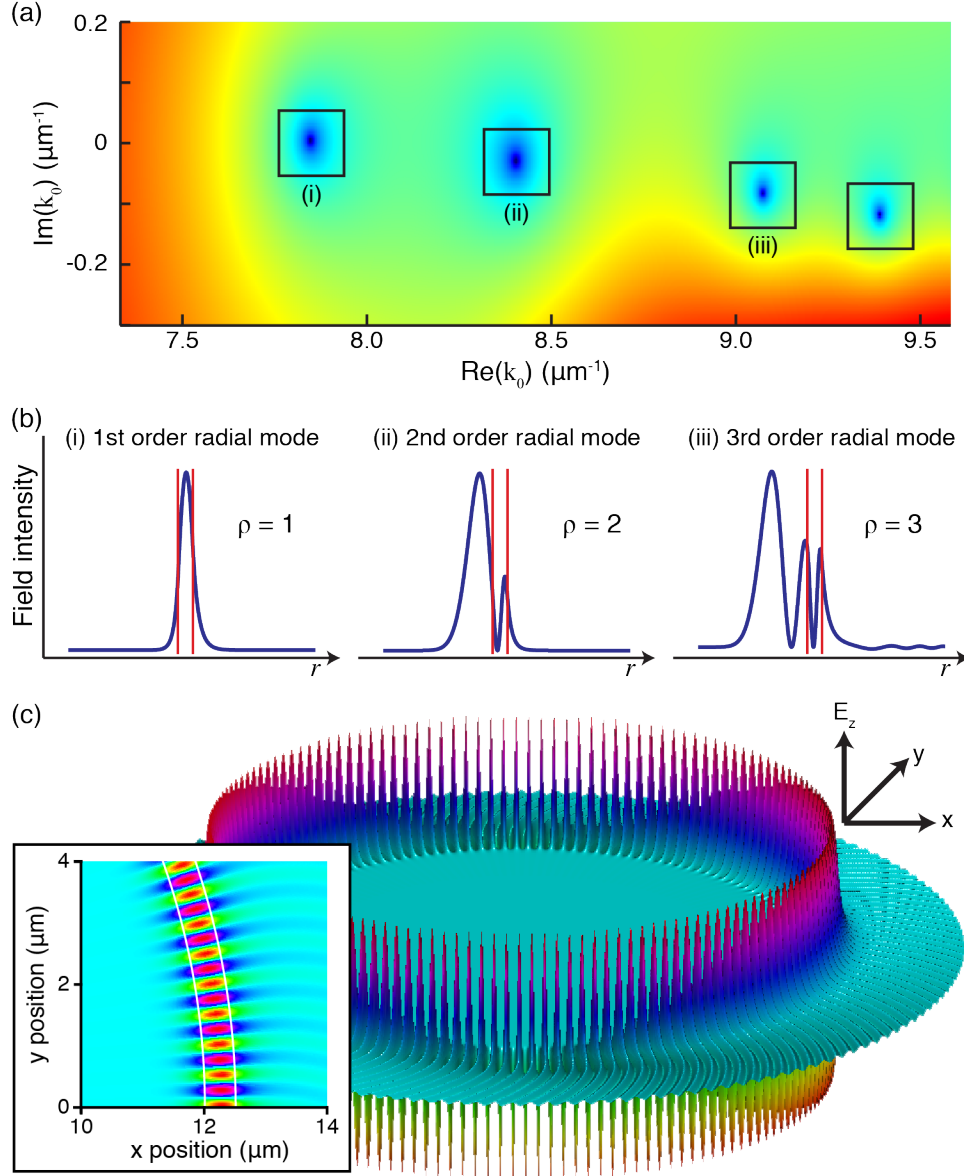
Figure 1.5: (a) Magnitude of Eq. 1.26 over complex k-space. Solutions to the characteristic equation exist at the zeros of the function (dark blue regions). For a given l an infinite number of solutions exist corresponding to different radial mode orders ($\rho = 1, 2, 3...$), marked by squares in the figure. (b) Radial intensity profiles of the first three radial modes. The region of the QD film is marked by red vertical lines. (c) Electric field (E_z) of a first order ($\rho = 1$) WGM ($a = 12.5\,\mu\text{m}$, $b = 12\,\mu\text{m}$). *Inset* Close up of film region. Boundaries of the film are highlighted by white lines.

1.3.2 Whispering gallery mode resonators

Biomolecular detection has been demonstrated in many WGM micro-resonator structures, including microfabricated waveguide/rings [54], toroids [55, 56], fibers [57], spheres [58],

and capillaries [53, 59–61] (Fig. 1.6). Of these structures, perhaps the most promising for microfluidic/LOC integration are microcapillaries, due to their inherent microfluidic channel. Capillaries also hold the unique property that the sensing surface is on the interior of the structure. In all of these structures one must have a method to couple light in and out of the resonator and probe the WGMs. The most popular method is the combination of a tapered fiber or waveguide to couple to the resonator, and a tunable laser to scan the optical frequencies. However, recent work, which is the primary focus of this thesis, has used an alternate fluorescence-based method.

Sphere   Cylinder

Ring or disk   Toroid
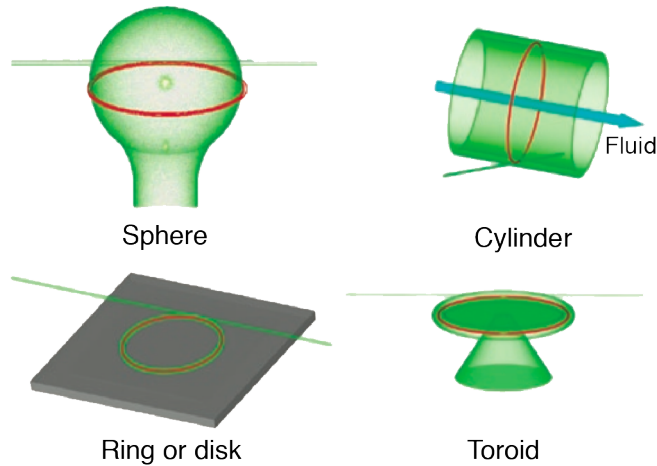
Figure 1.6: Whispering gallery mode resonators can take on a variety of shapes, including spheres, cylinders, rings, disks, and toroids. Modified from Ref. [62].

A common metric used to evaluate WGM sensors is the refractometric sensitivity. This is a measure of the sensitivity of the device in regards to changes in the refractive index of the analyte. The refractometric sensitivity (RS) is defined as

$$RS = \frac{\partial \lambda_{WGM}}{\partial n_{analyte}} \approx \frac{\Delta \lambda}{\Delta n} \tag{1.27}$$

For most devices the response is approximately linear for small index changes.

1.3.2.1   Liquid core optical ring resonators

Liquid core optical ring resonator (LCORR) structures, developed primarily by Xudong Fan and Ian White, at the University of Missouri-Columbia, combine WGM-based sensing with the microfluidic environment of silica microcapillaries [63]. LCORRs consist of a thin-walled glass microcapillary through which analyte fluids may be pumped; WGMs propagating in

the cylindrical cavity interact with the analyte (Fig. 1.7). Like other WGM-based sensors, LCORRs are sensitive to refractive index changes in the analyte, including those induced by surface-binding events.
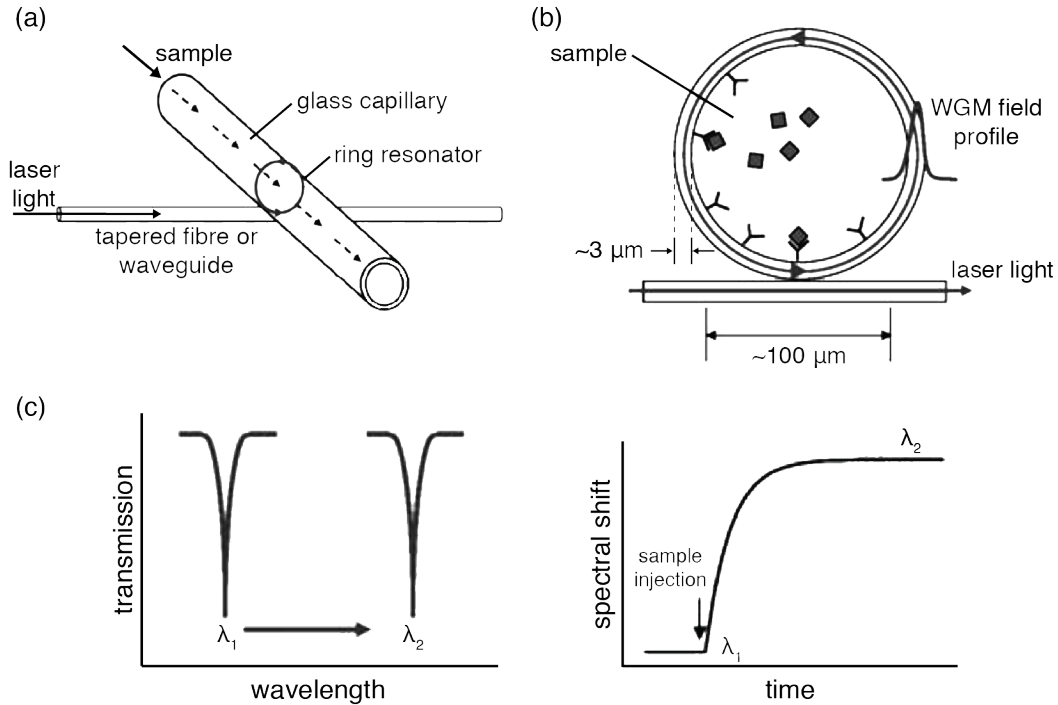
Figure 1.7: (a) Schematic of a typical LCORR device. (b) Biosensing in LCORRs is achieved through evanescent coupling. (c) WGMs appear as dips in the transmission spectrum. Changes in the sample cause a shift in the resonance wavelength. (d) Time-resolved measurements of the spectral shift allow the monitoring of sample injection and binding events. Modified from Ref. [59].

In order to serve as sensitive refractometric sensors the evanescent tail of WGMs in LCORRs must extend into the interior capillary channel. This requires the walls of the LCORR to be only a few micrometers thick. Thinning of the silica walls can be achieved through chemical etching using hydrofluoric (HF) acid. The final thickness of the capillary is determined by the concentration of the HF solution and the etching duration. This procedure has allowed the fabrication of LCORRs with outer capillary diameters $> 100\,\mu$m and walls $\lesssim 3\,\mu$m [64]. An alternative thinning method has been demonstrated by Zamora *et al.* which involves pressurizing the capillary with gas, then thinning the walls by simultaneously heating and pulling the capillary [60]. This method has enabled the fabrication of LCORRs with sub-μm wall thicknesses. While the thinning process does result in highly sensitive devices, it also leaves the structures very fragile.

Excitation of WGMs in LCORRs is done evanescently using a tunable laser and a tapered

optical fiber, which is held $< 1\,\mu$m from the LCORR. The excitation wavelengths are scanned with sub-pm resolution using a tunable laser and the WGMs are identified by sharp drops in the transmission spectrum. Evanescent coupling permits fast collection times and high resolution measurements. Using first order radial modes, LCORR-based sensors can exhibit refractometric sensitivities of typically $\sim 20\,$nm/RIU [11] but as high as $390\,$nm/RIU [60], detection limits as low as $10^{-6}\,$RIU, and sampling rates as fast as a few seconds [63, 64]. LCORRs using higher-order radial modes have demonstrated sensitivities of $570\,$nm/RIU and detection limits of 10^{-7}RIU [65]. Furthermore, their internal silica sensing surface is amenable to functionalization, allowing for analyte-specific detection [66, 67]. However, development of a true LOC/POC devices using LCORRs is hindered by the experimental and instrumental requirements of evanescent coupling. As noted above, the preparation of micron-thick capillary walls yields a mechanically fragile sensor. Also, the tapered fibre required for coupling must be held $< 1\,\mu$m from the structure and adjusted with nm-scale precision in order to ensure proper coupling between the fibre and the resonator. Finally, a stable, narrow-bandwidth tunable laser is required, adding both instrumental and economic complications towards LOC-device integration, as suitable tunable lasers can cost $> \$20,000$. Thus, while LCORRs have shown to be promising in a controlled laboratory setting, there are significant barriers to overcome before a reliable LCORR-based LOC/POC commercial device may be developed.

1.3.2.2 Fluorescent-core microcapillaries

Fluorescent-core microcapillaries (FCMs), consisting of a glass microcapillary coated with a luminescent QD film, offer a new method for microfluidic sensing. Like LCORRs, they combine the microfluidic capabilities of a microcapillary with the benefits of WGM-based optical transduction (Fig. 1.8), while offering potential advantages over LCORRs such as simple fabrication and use. As described, demonstration of FCMs for sensing is previously unreported.

FCM-based WGM biosensors are similar in principle to other WGM-based sensors: WGMs propagating in the resonator interact with the analyte fluid via an evanescent tail, and changes to the analyte cause shifts in the WGM resonance wavelength. However, the fabrication and operation of fluorescence based devices are fundamentally different from the "traditional" WGM sensors previously discussed. In short, a relatively high index, luminescent film is deposited on the sensor surface and is used both as the propagating medium and

excitation source for WGMs. This film may be composed of any luminescent material, however silicon-based structures are appealing for their biocompatibility and rich catalogue of fabrication methods, *e.g.,* luminescent Si-rich thin films or SiO_2-embedded Si nanocrystals (Si-NC). This concept is compatible with a number of WGM resonator structures, such as optical fibres [57] and microspheres [68], but it is particularly appealing for microcapillary resonators.
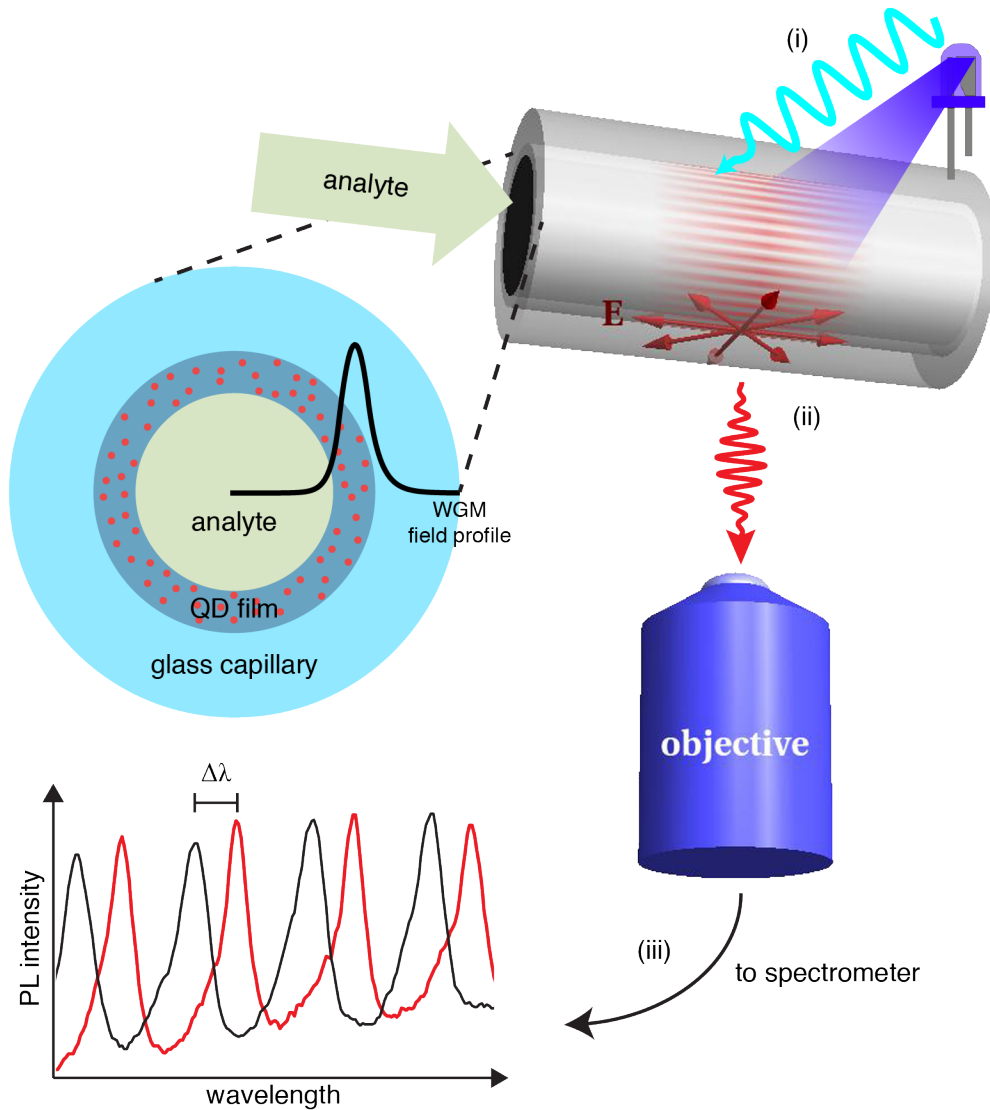
Figure 1.8: Schematic of a fluorescent-core microcapillary consisting of a glass capillary with a QD film coating its inner surface (Cross-section shown on left). Blue or UV light is used to excite the QDs in the film (i). Fluorescence from the QDs excites WGMs in the resonator. This fluorescence is collected by a microscope objective (ii) and directed to a spectrometer for analysis (iii). Changes in the refractive index of the analyte cause a shift ($\Delta\lambda$) in the WGM resonance wavelength.

Coating the inner surface of a microcapillary with a high index material permits the propagation of WGMs near the capillary core, in contrast to an uncoated structure where WGMs can only propagate at the external boundary. This negates the need for thin capillary walls as is required in LCORR structures. A such, FCMs can have arbitrarily thick capillary walls, so they are significantly more robust and easily handled than LCORRs. FCMs also eliminate the need for a tunable laser and nm-scale positioning systems required for the evanescent coupling to LCORRs. Instead, WGMs are excited using the luminescence of the film, which can be pumped using an appropriate external source, such as a laser or LED. Luminescence from the film can be collected and analyzed using standard spectroscopic techniques. In addition to avoiding the economic and spatial limitations of evanescent coupling, FCMs could enable the use of on-chip optical detection techniques such as the tapered Bragg waveguide spectrometer [69, 70].

Unlabeled fluorescence-based sensing has been demonstrated in "rolled-up" multilayers by Huang *et al.* [61]. Here, thin films of SiO and SiO_2 were deposited on a silicon substrate using chemical vapour deposition, then released and rolled in a process outlined in Ref. [71]. Preliminary measurements and simulations have suggested sensitivities could be as high as $\sim 425\,\mathrm{nm/RIU}$ and detection limits could be as low as $\sim 10^{-4}\,\mathrm{RIU}$. However, these structures are fabricated lithographically and are fixed to the substrate, making them marginally compatibile with microfluidic systems.

1.4 Optical properties of silicon nanocrystals

1.4.1 Quantum confinement in silicon nanocrystals

Bulk silicon is in general a poor light-emitter (see Appendix B). However, the electronic and optical properties of a bulk solid can be radically transformed when it is physically reduced in one or more dimensions to the nanometer scale. As a result of this quantum confinement, nano-sized structures can behave differently than their bulk counterparts, often exhibiting size-dependent emission wavelengths (Fig. 1.10a,b) and increased PL yields. Luminescence from Si has been observed in structures confined in 1D (thin films) [72], 2D (nanowires) [73, 74], and 3D (nanocrystals) [75].

Size-dependent luminescence in nanocrystals is due to a modification of the density of states (DOS) of the valence and conduction bands of the material. In nanostructures, the

DOS is "thinned" at band edges, resulting in the formation of quasi-discrete energy levels and increasing the bandgap of the material (Fig. 1.9) [76]. There are two distinct confinement regimes, the distinction being whether the nanocrystal radius a is greater (weak confinement) or smaller (strong confinement) than the Bohr exciton radius a_B. In the strong confinement regime (as is the case for visibly-luminescent Si-NCs) the ground-state exciton energy can be approximated as

$$E_{1,1,0} = E_g - 1.786 \frac{e^2}{\varepsilon a_B} + \frac{\pi^2 \hbar^2}{2\mu a^2} \tag{1.28}$$

where e is the elementary charge and $\mu^{-1} = m_e^{*-1} + m_h^{*-1}$. Equation (1.28) describes the discrete energy sub-bands as a combination of hydrogen-atom-like states of the bound exciton (second term in Eq. (1.28)), and particle-in-a-box-like states resulting from the physical confinement of electrons and holes (second term in Eq. (1.28)). The Coulombic interaction between the electron and hole is perturbed by the external potential at the nanocrystal boundary, resulting in the numerical multiplicative factor in the second term. Equation (1.28) diverges from the true exciton energy in both the upper ($a > a_B$) and lower ($a \lll a_B$) nanocrystal size limits (Fig. 1.10). For larger nanocrystals the exciton energy can approximated by a corresponding weak confinement expression; for smaller nanocrystals quantum chemical calculations must be performed.

Si-NCs also exhibit significantly greater PL efficiency than bulk silicon (10^{-6} in bulk silicon [78] compared to reports greater than 0.1 in nanocrystals [79,80]). The higher quantum efficiency can arise from several effects. First, the electronic transition can become more direct (*i.e.*, the selection rules governing the indirect transition are relaxed) as the nanocrystal shrinks in size, allowing the transition be become weakly allowed [76,77,81–83]. Second, the size reduction results in a slight increase of the exciton binding energy, providing thermal stability. Finally, the physical confinement of the $e - h$ pair reduces access to non-radiative pathways. In bulk Si, long radiative lifetimes and weak exciton binding energies allow $e - h$ pairs to migrate considerable distances in the crystal, often resulting in non-radiative recombination through defect states or Auger recombination. When the crystal dimensions are constrained, this long-range migration is not possible, limiting the probability of an exciton encountering a defect or second $e - h$ pair (such is required for Auger recombination) [82]. In this sense, confinement doesn't enhance radiative recombination in Si-NCs so much as it suppresses non-radiative processes.
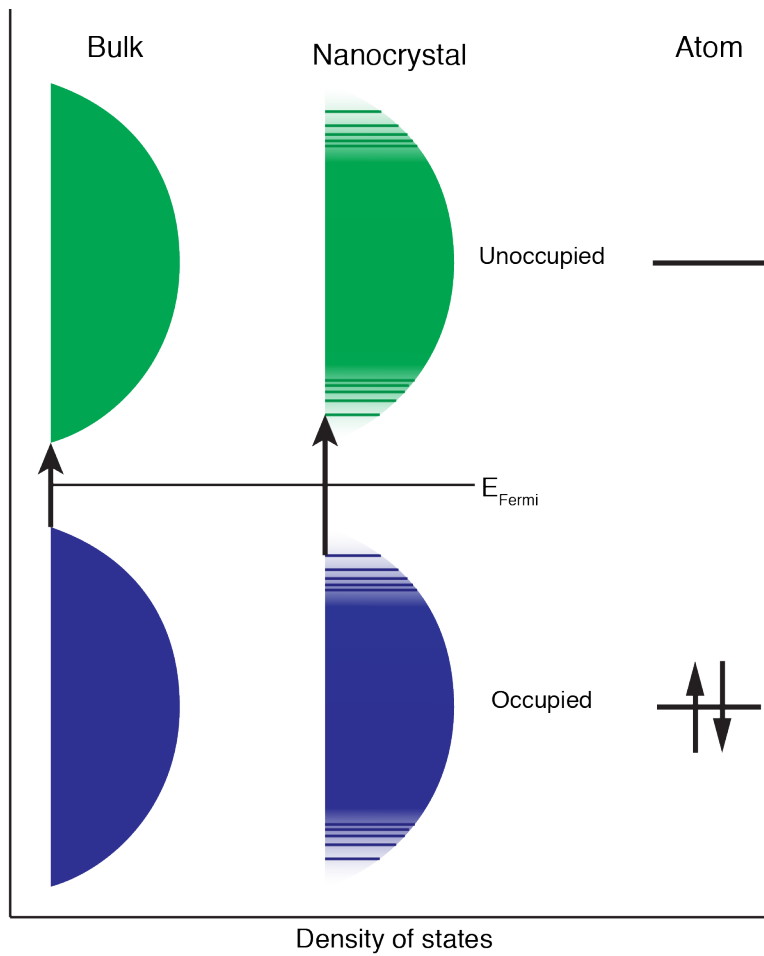
Figure 1.9: Density of states in a semiconductor nanocrystal. In a bulk material the DOS is continuous across the bands whereas in the atomic limit the DOS is represented by discrete energy levels. In nanocrystals the DOS is thinned, resulting in discrete energy levels at the band edges. Reproduced from Ref. [76].
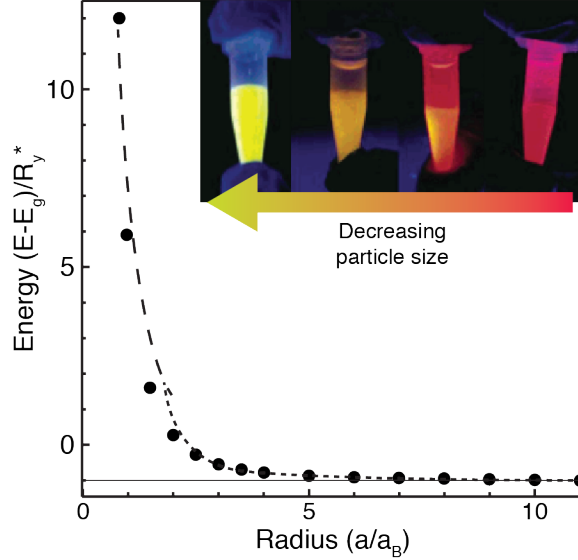
Figure 1.10: Exciton energy based on quantum confinement in an ideal nanocrystal: quantum chemical calculation (dot); Eq. 1.28 for strong confinement (long dash); corresponding weak confinement expression, short dash. Reproduced from Ref. [77]. *Inset* Result of quantum confinement in the PL of Si-NCs. The PL blue-shifts upon decreasing particle size, as predicted in theory. Modified from Ref. [75].

1.4.2   Fabrication oxide-embedded silicon nanocrystals

The fabrication of oxide-embedded Si-NCs is relatively simple, well known, and commonly practiced. Oxide-embedded Si-NCs are formed by the thermal treatment of Si-rich oxide (SiO_x, $0 < x < 2$), which can be prepared through one of several processes, such as laser ablation, ion implantation, sputtering and other physical deposition techniques, and chemical vapour deposition [84]. More recently however, our group developed a new method for fabricating oxide-embedded Si-NCs using the solid chemical precursor hydrogen silsesquioxane (HSQ) [75]. A significant advantage of this method is that it permits the uniform coating of non-planar structures (such as capillary channels) that could not be accessed by any of the previous methods.

HSQ is a cage molecule (Fig. 1.11) with the chemical formula $H_8Si_8O_{12}$. It is commonly used in the electronics industry as a spin-on dielectric. When thermally processed at *c.a.* $400\,^{\circ}C$ in an oxidizing environment HSQ collapses to form SiO_2 (silica) and SiH_4 (silane, the more explosive cousin of methane gas) [85]. However, processing at $900 - 1400\,^{\circ}C$ in a slightly reducing environment results in the formation of oxide-embedded Si-NCs. The annealing conditions for NC formation have been studied and reported on extensively [75, 86–88]. In summary, processing at $1100 - 1400\,^{\circ}C$ for 1 hr produces luminescent Si-NCs $\sim 4 - 14\,nm$ in

size with a central emission wavelength shifting from $\sim 800\,\mathrm{nm}$ to $\sim 925\,\mathrm{nm}$ as the annealing temperature increases [86]. HSQ precursor solutions have been used to fabricate high-quality luminescent films on a variety of planar and non-planar surfaces (Fig. 1.11) [57, 89, 90].
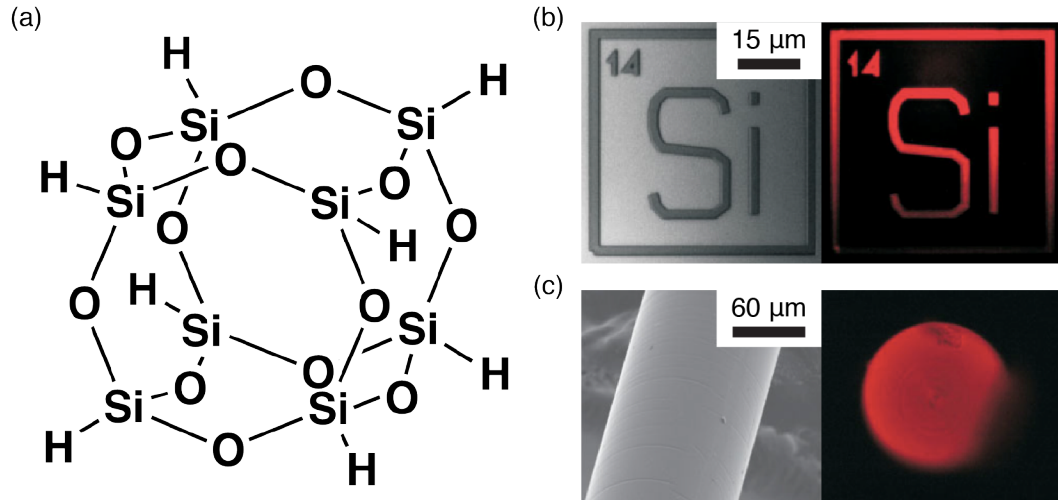
Figure 1.11: HSQ (a) can be used for solution-based processing of Si-NC films. Luminescent films may be fabricated on (b) lithographically (e-beam) defined surfaces, flat substrates, and (c) non-planar surfaces such as optical fibers (shown) and capillaries. Modified from Ref. [89].

Chapter 2

Experimental

2.1 Sample preparation

2.1.1 Introduction

The preparation of FCMs requires the fabrication of a thin, luminescent film on the interior surface of a microcapillary. This can be achieved using the precursor HSQ, which is available in solution, dissolved in methyl isobutyl ketone (MIBK). Fabrication of thin, QD-embedded films using HSQ precursor solutions was first outlined in Ref. [89], where films were fabricated on flat substrates and optical fibres. This process was then extended to allow film fabrication in glass microcapillaries in Ref. [91]. For all the above-noted structures HSQ solutions can be applied in a relatively facile way: the solution can be spin coated onto flat substrates, and fibres and capillaries can be dipped into the solution. For optical fibres, dipping coats the external fibre surface with the HSQ solution. For capillaries, dipping draws the solution up the channel via capillary forces, completely filling the capillary.

Thermal processing of HSQ in a reducing environment can result in the formation of Si-NCs embedded in a SiO_2-like matrix. There are three distinct phases in this process, as described in [86] and [87]:

1. $T \leq 400\,^{\circ}\mathrm{C}$: HSQ cross-linking and cage rearrangement. No indications of low-valent Si (*i.e.* Si^{n+}, $n < 4$).

2. $500\,^{\circ}\mathrm{C} < T < 900\,^{\circ}\mathrm{C}$: Disproportionation of HSQ yielding elemental Si and SiO_2. Si atoms migrate through the oxide forming non-crystalline nanodomains.

3. $T > 900\,°C$: Crystallization and growth of Si nanodomains

The annealing conditions dictate the size and luminescent properties of the resulting NCs. For films on flat substrates and optical fibres, high quality, red-luminescent films can be produced by annealing samples at $1100\,°C$ for $\sim 1\,hr$ in a slight reducing atmosphere (*e.g.,* 5% H_2:95% Ar). To ensure consistent film formation and stability, the annealing process for capillaries is more complicated. Samples must first be processed at $\sim 300\,°C$ for $2 - 3\,hrs$ in order to evaporate the solvent and deposit HSQ molecules on the inner surface of the capillary, and then annealed at $1100\,°C$ as in the case of fibres and flat substrates. Furthermore, a long cooling time ($\sim 12\,hrs$) is required for capillaries to ensure a uniform, crack free film.

For the purpose of this thesis, focus was aimed at fabricating QD films in capillaries, using the method outlined above, in order to synthesize the desired FCM structure. However, for some characterization techniques including ellipsometry and TEM, it was necessary to use a flat sample. Thus, in addition to the capillary samples, QD films were fabricated on flat substrates by spin coating and annealing.

2.1.2   Capillary preparation

The capillary tubing used in this work was manufactured by Polymicro Technologies and purchased in spools of 10 m [92]. The tubing was made of fused silica, coated with a flexible polyimide jacket (see Fig. 2.1). Several capillary sizes, with various inner diameters (IDs) were used: $10\,\mu m$, $25\,\mu m$, $50\,\mu m$, $75\,\mu m$, and $100\,\mu m$. Full specifications of the capillaries are presented in Table 2.1. Prior to solution processing, the capillaries were sectioned, cleaned, and had their polyimide coating removed.
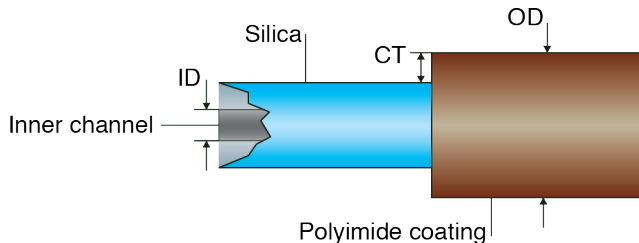

Figure 2.1: Diagram of capillary specifications. Inner diameter (ID), outer diameter (OD), and polyimide coating thickness (CT) quoted from manufacturer [92].

The capillary tubing was cleaved into several (approx. 10-20 per session) $\sim 2\,inch$ sections by first scoring the glass with a ceramic tile, then snapping. This method was used to avoid

Table 2.1: Manufacturer-quoted specifications of capillary sizes [92]

Inner diameter (μm)	Outer diameter (μm)	Coating thickness (μm)	Part No.
10 ± 2	363 ± 10	20	TSP010375
25 ± 2	363 ± 10	20	TSP025375
50 ± 3	363 ± 10	20	TSP050375
75 ± 3	193 ± 7	12	TSP075200
100 ± 4	164 ± 6	12	TSP100170

clogging the central channel of the capillaries with debris from an unclean cleave, or pinching the channel closed, as can occur when using optical fiber cleavers. The section length of the capillaries is limited only the the physical dimensions of the equipment used in fabrication; 2 inches was a convenient size to handle, transport, interface with the microscope apparatus, and is compatible with the instruments used in the rest of the preparation.

The polyimide coating may be removed through a number of thermal treatments. Several methods are specified by the manufacturer: open flame, gas torch, oven, electrical coil heater, electric arc, CO_2 laser, strong acid, or strong base. It is important that the technique used does not damage the capillary, compromise its structural integrity, or contaminate its inner surface (*i.e.* must be clean). Two methods were used which satisfy these criteria: burn-off in a furnace at $> 600\,°C$ and dissolution in hot sulfuric acid (H_2SO_4).

Furnace-heating Sectioned capillary samples were heated in a Barnstead Thermolyne 21100 tube furnace to $650\,°C$ for $45\,min$. Oxygen gas (O_2) was flowed through the furnace during heating to aid in the burn-off of the polyimide coating. Samples were allowed to cool over a period of $\sim 1\,hr$.

Acid treatment Sulfuric acid ($18\,M$) was heated to $\sim 300\,°C$ (*i.e.* until steaming) on a hot plate. Sectioned capillary samples were placed in the sulfuric acid for $15\,min$, allowing for the removal of the polyimide coating. The capillaries were then rinsed with distilled water, then further cleaned using a "piranha" solution (*i.e.* 3:1 mixture of H_2SO_4:H_2O_2). They were again rinsed in distilled water, then flamed dried with a torch.

2.1.3 Preparation of solution-based precursor

A commercially available HSQ solution (18% w/w HSQ in MIBK [93]) was used as a precursor for the formation of the Si-NC/SiO$_2$ film. As reported in Ref. [91], this "stock" solution was not optimal for use with all capillary sizes. To produce films with the desired thickness

and structure, the concentration of the precursor solution was adjusted. For brevity, the HSQ precursor solution will be referred to as HPS, or sHPS, where "s" indicates the stock solution.

The QD film is formed by depositing HSQ molecules onto the inner walls of the capillary, then annealing. The thickness of the resulting film can be related to the concentration of the starting HPS. For a capillary of length l and ID $2r$, and a solution concentration of C (in mol/L), the initial mass of HSQ in the solution-filled capillary is

$$m_{initial} = nM_{HSQ} = CV_i M_{HSQ} \tag{2.1}$$

where M_{HSQ} is the molar mass of HSQ (424.7 g/mol) and $V_i = \pi r^2 l$ is the inner volume of the capillary. Next, during the first annealing phase, the solvent is evaporated and the HSQ molecules are deposited on the inner wall of the capillary. Not all of the initially-present HSQ will be deposited, as some is likely to escape as the solvent evaporates. However, let it be assumed that the mass of HSQ deposited ($m_{deposited}$) is roughly proportional to initial mass present, *i.e.*, $m_{deposited} \propto m_{initial}$. In the second annealing phase the HSQ undergoes a disproportionation reaction yielding Si-NCs embedded in a SiO_2-like matrix. Again, some mass will be lost in this step, *e.g.*, to gaseous byproducts such as silane, however it may once again be assumed that this mass loss is proportional to the initial mass present. Thus, the final mass of the film will be roughly proportional to the initial mass of HSQ present in the capillary prior to annealing. Given a uniform film density, the initial mass is also proportional to the volume of the final film. This volume V_{film}, through simple geometrical considerations, is given by

$$\begin{aligned} V_{film} &= \left(\pi r^2 - \pi(r - d_f)^2\right) l \tag{2.2} \\ &= \pi l (2rd_f - d_f^2) \tag{2.3} \end{aligned}$$

where d_f is the thickness of the film. Combining Eqs. (2.1) and (2.2) under the conditions described above results in

$$
\begin{aligned}
m_{initial} &\propto V_{film} \\
M_{HSQ}C(\pi r^2 l) &\propto \pi l(2rd_f - d_f^2) \\
C &\propto 2\left(\frac{d_f}{r}\right) - \left(\frac{d_f}{r}\right)^2
\end{aligned}
\tag{2.4}
$$

For thin films (relative to the capillary diameter) the quadratic term may be neglected, yielding a simple expression indicating that the film thickness is proportion to both the capillary radius and HPS concentration:

$$
d_f \propto rC \tag{2.5}
$$

Thus, when making large-diameter samples, the HPS had to be diluted in order to keep the film thin enough for the WGM tail to extend into the capillary (Fig. 1.8). Conversely, the solution had to be concentrated for smaller-diameter capillaries. For dilutions, an appropriate solvent (m-xylene, Sigma-Aldrich, anhydrous > 99%) was added to the sHPS; for concentrations, dry, dried HSQ was prepared and dissolved in the solvent. Various concentrations were tested for each capillary size. Concentrations yielding successful samples are discussed in Sec. 3.1 and presented in Table 3.1. Due to the oxygen/water-sensitivity of HSQ, all the manipulations described in Sections 2.1.3.1 and 2.1.3.2 were performed in an inert environment, specifically, in an Ar glove-box (with the exception of the drying of the HSQ solution which was performed on a Schlenk line). Furthermore, any solvent used was dry (*i.e.,* anhydrous, and never exposed to atmosphere) and stored under inert conditions.

Experimentally it was more straightforward to measure the mass of the components (*i.e.,* HPS, sHPS, solid HSQ, solvent), so the concentrations referred to for the remainder of this thesis are quoted either as a mass fraction, denoted by W, or a weight percent (%w/w). The molar concentration C can be related to W through the molar mass of HSQ and the densities of HSQ and the solvent:

$$
C = \frac{W}{M_{HSQ}} \left(\frac{1}{\frac{1-W}{\rho_{solvent}} + \frac{W}{\rho_{HSQ}}} \right) \tag{2.6}
$$

where $\rho_{solvent}$ and ρ_{HSQ} are the densities of the solvent and solid HSQ, respectively. While $\rho_{solvent}$ is typically known, ρ_{HSQ} is not, making Eq. (2.6) not directly usable. However,

over small regions, Eq. (2.6) is approximately linear in W. Furthermore, the non-linearity of C and W is not crucial, since Eq. (2.5) was simply used to illustrate the general trend of the film thickness, and to provide an educated estimate to the required HPS concentrations when fabricating the samples.

2.1.3.1 Dilution of HSQ solution

For larger capillary samples, *i.e.*, IDs of $50\,\mu$m, $75\,\mu$m, and $100\,\mu$m, the sHPS was diluted. An aliquot of sHPS, typically $\lesssim 0.1\,$g, was weighed in a glass vial. The additional mass of solvent $m_{solvent}$ required to achieved the desired concentration, W_2, was calculated using the equation

$$m_{solvent} = m_{precursor}\left(\frac{W_1}{W_2} - 1\right) \tag{2.7}$$

where W_1 and W_2 are the initial and desired final mass fractions, respectively (*e.g.*, the mass fraction of 18%w/w sHPS was $W_1 = {}^{m_{HSQ,1}}/m_{total,1} = 0.18$), and $m_{precursor}$ is the measured mass of the sHPS aliquot. The sample was diluted with the solvent m-xylene, added drop-wise, until the approximate required mass was achieved. The actual final concentration was then calculated using equation 2.7 from the measured values $m_{precursor}$ and $m_{solvent}$.

For example, when preparing the $100\,\mu$m ID capillaries, a HPS concentration of $\sim 1.8\,\%$w/w was desired (see Table 3.1). An aliquot of sHPS ($18\,\%$w/w) was measured to be $0.0926 \pm 0.0003\,$g. Using Eq. (2.7), the desired mass of m-xylene to be added was calculated:

$$
\begin{aligned}
m_{solvent} &= 0.0926\left(\frac{0.18}{0.018} - 1\right)\\
m_{solvent} &= 0.833\,\text{g}
\end{aligned}
$$

However, due to the limitations of the dropper, this mass could not be added exactly. The actual mass of solvent added was measured to be $0.8369 \pm 0.0003\,$g, yielding a final HPS concentration of

$$W_{final} = \frac{W_1 m_{precursor}}{m_{precursor} + m_{solvent}} = \frac{0.18(0.0926)}{0.0926 + 0.8369}$$

$$W_{final} = 0.0179 \approx 1.8\,\%\mathrm{w/w}$$

2.1.3.2   Concentration of HSQ solution

For the preparation of the $10\,\mu$m and $25\,\mu$m capillaries the sHPS was concentrated. This was accomplished by first drying the sHPS to obtain solid HSQ and then dissolving the HSQ in m-xylene.

Extraction of solid HSQ from precursor solution   A few mL of sHPS was placed in a round-bottom Schlenk flask which was subsequently sealed and removed from the inert environment glove box. The flask was attached to a vacuum-gas manifold (Schlenk line) and the solution was dried under vacuum for several hours. Once the solvent had evaporated, leaving only solid HSQ, the flask was removed from the manifold. The solid was scraped off the walls of the flask, then flame-dried using a hand torch. The flask was replaced on the manifold and was left under vacuum overnight. Finally, the flask was filled with Ar gas, sealed, and replaced in the inert environment.

Preparation of HSQ solution   A small amount, typically $0.05 - 0.10\,$g, of previously prepared solid HSQ was weighed in a glass vial (m_{HSQ}). The solvent m-xylene was added drop-wise until the desired concentration was obtained, in accordance with the equation

$$m_{solvent} = m_{HSQ} \left(\frac{1}{W} - 1 \right) \tag{2.8}$$

where W is the desired mass fraction of the HPS. The final concentration was then calculated using equation 2.8 from the measured values $m_{solvent}$ and m_{HSQ}.

For example, when preparing the $25\,\mu$m ID capillaries, a HPS concentration of $\sim 25\,\%\mathrm{w/w}$ was desired (see Table 3.1). A small amount of solid HSQ was measured to be $0.1065 \pm 0.0003\,$g. Using Eq. (2.8), the desired mass of solvent to be added was calculated:

$$m_{solvent} = 0.1065 \left(\frac{1}{0.25} - 1 \right)$$

$$m_{solvent} = 0.320\,\mathrm{g}$$

The actual mass of solvent added was measured to be 0.3213 ± 0.0003 g, yielding a final HPS concentration of

$$
\begin{aligned}
W_{final} &= \frac{m_{HSQ}}{m_{HSQ} + m_{solvent}} = \frac{0.1065}{0.1065 + 0.3213} \\
W_{final} &= 0.2489 \approx 24.9\,\%\text{w/w}
\end{aligned}
$$

2.1.4   Application of precursor solution and annealing

The HSQ solution-coated samples were annealed in a slightly reducing environment, resulting in the formation of the Si-NC/SiO$_2$ film. The annealing process depended on the sample being prepared.

Capillaries   Several HPS concentrations were tested for each capillary size; see Table 3.1 in the Sec. 3.1 for the concentration of the HPS that produced successful samples. A small aliquot (< 0.5 mL) of previously-prepared HPS was transferred to a glass vial and removed from the inert environment. One end of each capillary was dipped into the HSQ solution for $\sim 15 - 30$ s. During this time, the solution filled the capillary channel via capillary forces.

  The annealing process of capillary samples occurred in three steps:

1. $300\,^\circ$C for 3 hrs.

2. $1100\,^\circ$C for 1 hr.

3. Cooling: 1 hr or 12 hrs

Annealing was performed in either a Lindberg/Blue M tube furnace or Thermal Technologies Inc. upright furnace. A gaseous mixture of either 5% H$_2$:95% Ar or 5% H$_2$:95% N$_2$ was flowed over the samples during the entire annealing and cooling process.

Flat films   100 μL of HSQ precursor solution was spin-coated onto a clean Si-wafer for 25 s at 1000 rpm. Flat samples were annealed at $1100\,^\circ$C for 1 hr in a Thermal Technologies Inc upright furnace and cooled over a period of ~ 1 hr. A gaseous mixture of 5% H$_2$:95% N$_2$ was flowed over the samples during the entire annealing and cooling process. For samples prepared for ellipsometry and/or SEM, the spin-coating/annealing procedure was repeated three times in order to fabricate a film of sufficient thickness.

2.2 Materials characterization

A number of techniques were used to determine the physical and optical properties of the QD films. Electron microscopy was used to study composition and thickness of the films. Optical imaging and spectroscopic techniques were used to determine the optical properties of the films and cavities. Obtaining properties such as the film thickness and refractive index is important in understanding the physics of the optical cavities. As outlined in Sec. 1.3.1.2, WGMs are sensitive to these parameters so an intimate knowledge relating them to the performance of a device will aid in further improvement and development.

2.2.1 QD Film microstructure

Transmission electron microscopy (TEM) was performed by X.Y. Wang on a flat, spin coated film using a JEOL 2010 transmission electron microscope. TEM samples were prepared by standard cross-sectional thinning methods. Standard bright field and high-resolution images and electron diffraction patterns were collected in order to confirm the presence of Si-NCs.

Scanning electron microscopy (SEM) was performed using a JEOL 6301F field-emission scanning electron microscope. SEM images were collect for both capillaries and flat films. Flat films were cleaved vertically and imaged from the side to allow the measurement of the film thickness. This thickness was required for fitting ellipsometry data previously collected on the films. Capillaries were snapped or cleaved perpendicularly to their axis using optical fibre cleavers, exposing a cross-sectional surface. All samples were coated in a thin layer of chrome or gold prior to SEM imaging to improve conductivity and reduce charging effects.

2.2.2 Optical constants of QD film

Variable angle spectroscopic ellipsometry (VASE) was performed, with the assistance of N. Ponnampalan, on a flat, spin-coated QD film in order to measure the optical constants of the film. Reflection data was obtained at incident angles of $65°$ and $75°$ over a wavelength range of $300 - 1700\,\text{nm}$. A Si wafer was used as the sample substrate in order to provide contrast with the oxide film. The sample was sequentially spin coated and annealed three times to generate a film thick enough to produce clear oscillations in the reflection spectrum. The thickness of the film (measured using SEM) was used as a starting point for the Cauchy-model fitting used to extract the optical constants.

2.2.3 Flat film spectroscopy

Flat film samples were fixed in place on an optics bench. The 325 nm line of a Omnichrome Series 56 helium-cadmium (HeCd) laser was used for NC excitation. The PL from the film was collected using an optical fibre, held $\lesssim 1$ cm from the sample, and fed to an Ocean Optics USB-2000 spectrometer. The spectrometer was USB-interfaced to a computer via the Ocean Optics *Spectra Suite* software. Spectra were intensity-calibrated using an Ocean Optics HL-2000 FHSA Tungsten Halogen light source. The USB-2000 spectrometer is pre-calibrated for wavelength.

2.3 Fluorescence microscopy

2.3.1 Fluorescence imaging

Capillary samples were mounted on the stage of a Nikon Eclipse TE 2000-e inverted microscope which was interfaced to a QImaging colour CCD camera (See Fig. 2.2a). The Si-NCs were pumped with the 488 nm line of a Coherent Innova 70c Ar-ion laser operating in continuous wave mode at a power of ~ 40 mW. Fluorescence images were captured without the use of a background illumination source. PL from the Si-NCs was collected through the microscope objective by the colour camera. A filter was inserted between the microscope objective and CCD in order to avoid laser light from entering the camera. Typically, collection times of $\sim 5 - 30$ s were required fluorescence images.

2.3.2 Spectroscopy

The microscope is also interfaced to a spectrograph, which allows for spectroscopic analysis of the capillary samples. One of two light sources was used to excite the Si-NCs in the capillaries: an Argon-ion laser or an LED (Fig. 2.2). The 488 nm line of the Ar-ion laser was used, operating in continuous wave mode at an incident power of ~ 40 mW with a beam diameter of ~ 2 mm focussed at the sample. The beam struck the sample in free space, perpendicular to the microscope objective. A 550 nm long-pass filter was used in-line, after collection through the microscope objective, to prevent scattered laser light from entering the microscope optics. For LED excitation a Prizmatix 405 nm LED was operated at an incident power of ~ 2 mW. In this case, light from the LED was focused through the microscope objective and onto the sample. PL from the NCs was collected through a 10x

or 20x microscope objective and was subsequently directed to the spectrograph. A linear polarizer was inserted between the microscope objective and the spectrograph to control the polarization of the collected light.
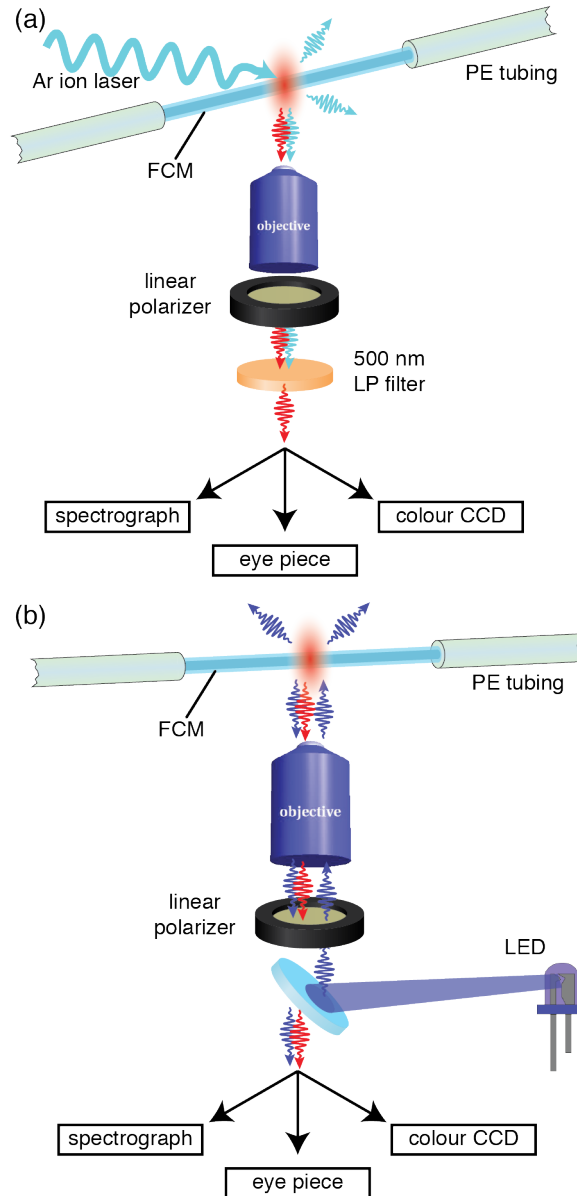
Figure 2.2: Schematic of microscope and beam paths used in studying the FCMs. (a) Laser excitation. The laser excites the FCM in free space above the microscope. Fluorescence is collected by the microscope objective then filtered, using a polarizer and a long-pass filter, before being directed to the spectrograph (for spectral analysis), eye piece (for viewing), or colour CCD (for imaging). (b) LED excitation. Light from the LED is focused through the objective lens onto the FCM.

PL spectra were collected using a Santa Barbara Instrument Group (SBIG) self-guided spectrograph (SGS) coupled to a ST-7XME camera. The spectrograph was equipped with

a 18 μm-wide slit and a 600 lines/mm grating, resulting in a pitch of 0.104 nm/pixel at the imaging CCD. The CCD camera was thermoelectrically cooled to $-15\,°C$ to minimize detector noise. Typically, collection times between 2 min and 5 min were used when collecting PL spectra. The camera was computer-interfaced via the manufacturer-supplied CCDOps software. Raw spectral intensity data was exported as a 16-bit TIFF files for analysis.

2.3.3 Calibration

All PL spectra required calibration for both wavelength and intensity. The Ocean Optics USB-2000 spectrometer, used to collect PL spectra from the flat films, was manufacturer-calibrated for wavelength; spectra were corrected for intensity automatically in Spectra Suite using a standard blackbody light source. The calibration of spectra collected using the SBIG SGS required more attention, for several reasons: 1) the SGS/ST-7 spectrograph and camera are not pre-calibrated by the manufacturer for wavelength or for intensity, 2) alignment of the entrance slit, grating, and CCD array caused a "rotation" of the spectra on the CCD, and 3) the CCDOps software allowed for little manipulation/correction of the spectra, so external software was required. An Ocean Optics HL-2000 FHSA Tungsten Halogen light source with a colour temperature 3100 K was used to correct for detector response and the spectral lines of a Hg/Ar lamp were used to calibrate the wavelength of the spectra.

The ST-7 camera possesses a 765 x 510 pixel CCD yielding 2D spectral data: the horizontal direction representing wavelength and the vertical direction representing position along the entrance slit. The PL, Hg/Ar calibration, and blackbody calibration spectra were exported from CCDOps as 16-bit TIFF images and imported into the image editing software *ImageJ* for manipulation (Fig. 2.3, left). The PL spectrum was rotated such that the spectrum was aligned horizontally; the blackbody and Hg/Ar spectral images were then rotated by the same angle. A horizontal cross section was extracted from the images from the region corresponding to the edge of the capillary core, where WGMs were most predominant in the PL spectrum (Fig. 2.3, right). The PL spectrum was then corrected for intensity using the collected blackbody spectrum and Plank's radiation law:

$$S(\lambda) = s(\lambda)\frac{I_{\lambda,T}(\lambda)}{B_{\lambda,T}(\lambda)} \tag{2.9}$$

where $S(\lambda)$ is the intensity-calibrated PL spectrum, $s(\lambda)$ is the raw PL spectrum, $B_{\lambda,T}(\lambda)$ is the collected blackbody spectrum, and $I_{\lambda,T}(\lambda)$ is the theoretical blackbody intensity curve

(a)
PL spectrum

(b)
Blackbody
spectrum

(c)
Hg/Ar calibration
spectrum

(d)
Calibrated WGM
spectrum
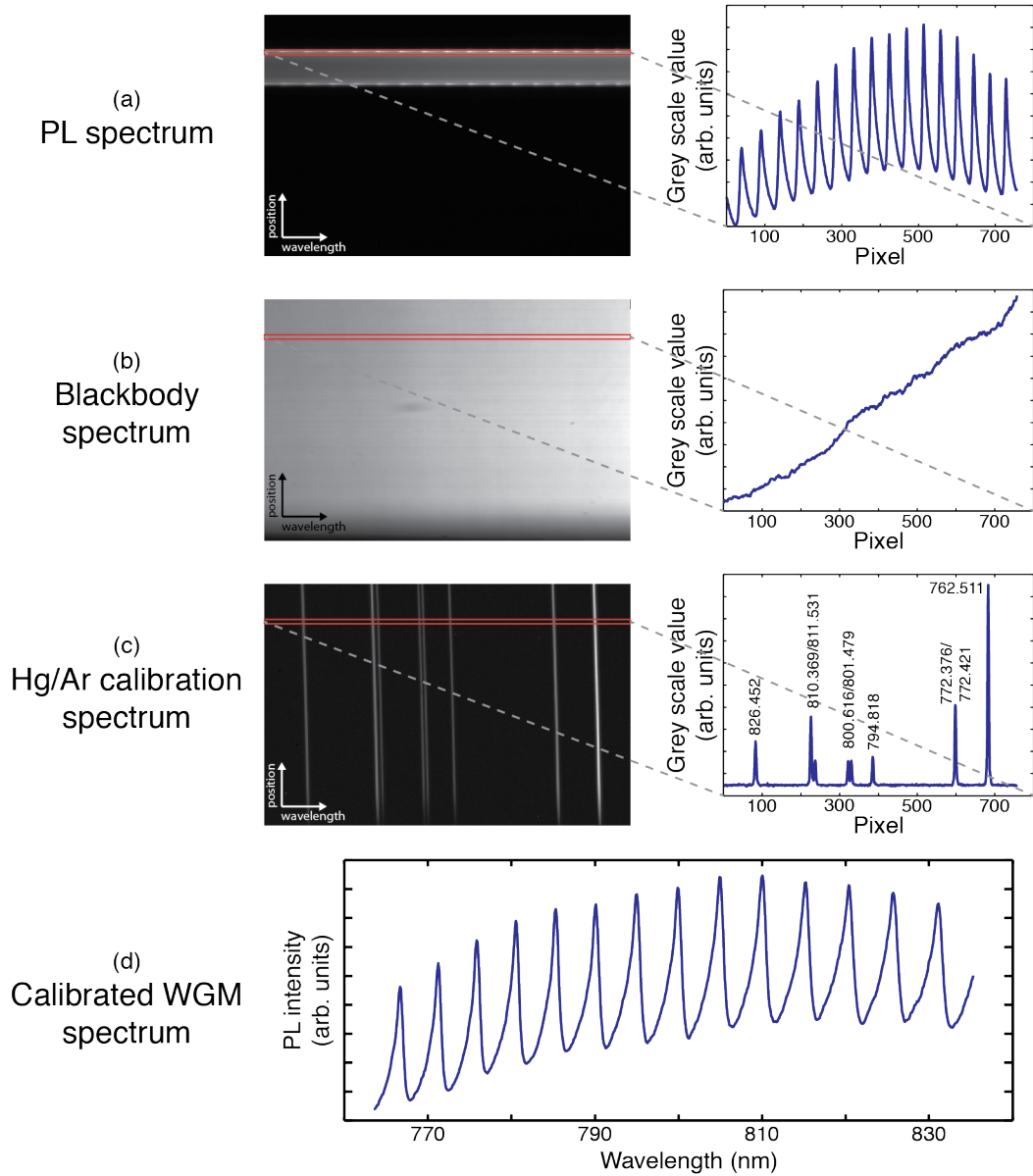
Figure 2.3: Calibration of WGM spectra. Collected PL, blackbody, and Hg/Ar spectra: *Left* rotated 2D spectra, *Right* averaged cross section of selected area. *Calibration* The PL cross section (a) was calibrated for intensity and wavelength using the corresponding cross sections from the blackbody (b) and Hg/Ar (c) spectra. The intensity was corrected using Eqs. (2.9) and (2.10), and the pixel value was correlated to the appropriate wavelength using the observed spectral lines in the Hg/Ar spectrum. (d) The final calibrated WGM spectrum.

for a given temperature, T, given by Plank's law:

$$I_{\lambda,T}(\lambda) = \frac{2hc}{\lambda^5} \frac{1}{e^{\frac{hc}{\lambda kT}} - 1} \tag{2.10}$$

Known spectral lines of the Hg/Ar source were used to map the CCD pixel value to wavelength; this map was used to calibrate the PL and blackbody spectra. This process was repeated for every PL spectrum to ensure accurate calibration. In some cases it was beneficial to extract a spectrum from a range of horizontal cross sections, in which case the pixels were averaged vertically to produce the final spectrum.

2.4 Sensor characterization

2.4.1 Refractometric Sensitivity

In order to determine the refractometric sensitivity (RS) of the FCM, the capillaries were interfaced to a syringe pump. Solutions of different concentrations of sucrose in water were then pumped through the capillaries. Sucrose is inexpensive, non-toxic, soluble, and has well documented optical properties [94–97]. The refractive index of aqueous sucrose solutions is shown in Table 2.2 [98,99]. Sucrose has a solubility of 2000 g/L [100]; however, experimentally, solutions with a concentration of more than 900 g/L were found to be too viscous to be pumped through the capillary channel.[1] This limitation provided a working refractive index range of $1.333 - 1.458$ RIU. Eleven solutions were prepared for use in this investigation (Table 2.2). First, an 850.9 g/L sucrose in distilled water "stock" solution was prepared (solution #11). The other solutions (solutions #2-10) were prepared by diluting the stock solution with distilled water. Solution #1 was pure distilled water.

FCMs were interfaced to the syringe pump via polyethylene (PE) tubing [101]. Polyethylene tubing was selected due to its chemical inertness, stiffness, and availability in small diameters. Each capillary sample was glued, at both ends, to PE tubing using one of a variety of glues, *e.g.,* super glue or contact cement. One end of the sample was attached to the syringe pump; the other was attached to a reservoir to collect waste fluid (Fig. 2.5b). The sample was fixed to a "home-made" sample holder which was subsequently mounted to a breadboard on the microscope stage (Fig. 2.5c). Plastic syringes (1 mL) were loaded with the various sucrose solutions and a Chemyx Nanojet syringe pump was used to pump

---

[1]The actual upper limit depends of the sample, particularly the capillary ID, and flow rate. 900 g/L is an empirically-obtained limit found to be suitable for most samples.
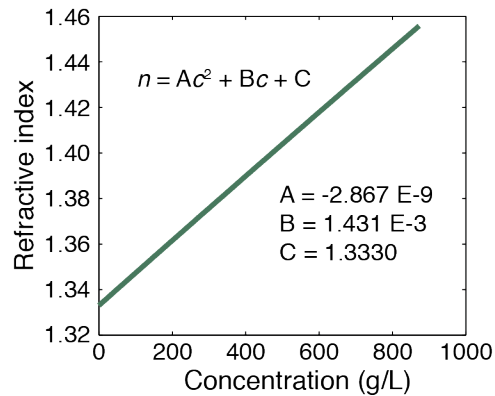
Figure 2.4: Refractive index of aqueous sucrose solutions [98, 99]

Table 2.2: Concentration and refractive index of prepared sucrose solutions

Solution #	Notes	Sucrose concentration (g/L)	Refractive index [98, 99]
0	air (no solution)	N/A	1.0
1	distilled water	0.0	1.333
2		85.1	1.345
3		170.2	1.357
4		255.3	1.369
5		340.3	1.381
6	diluted from	425.4	1.393
7	solution #11	510.5	1.405
8		595.6	1.417
9		680.7	1.429
10		765.8	1.441
11	"stock" solution	850.9	1.453

the sucrose solutions, one at a time, through the capillaries. This apparatus, depicted in Fig. 2.5a, allows the experimenter to change the refractive index of the capillary core (by pumping various sucrose solutions) and collect corresponding fluorescence spectra without physically touching or moving the sample. This ensured the same region of the capillary and film was sampled each time. The refractometric sensitivity of two FCMs was tested: 1) a $25\,\mu$m ID capillary and 2) a $100\,\mu$m ID capillary (for brevity, these are henceforth referred to as Type-I and Type-II FCMs, respectively).
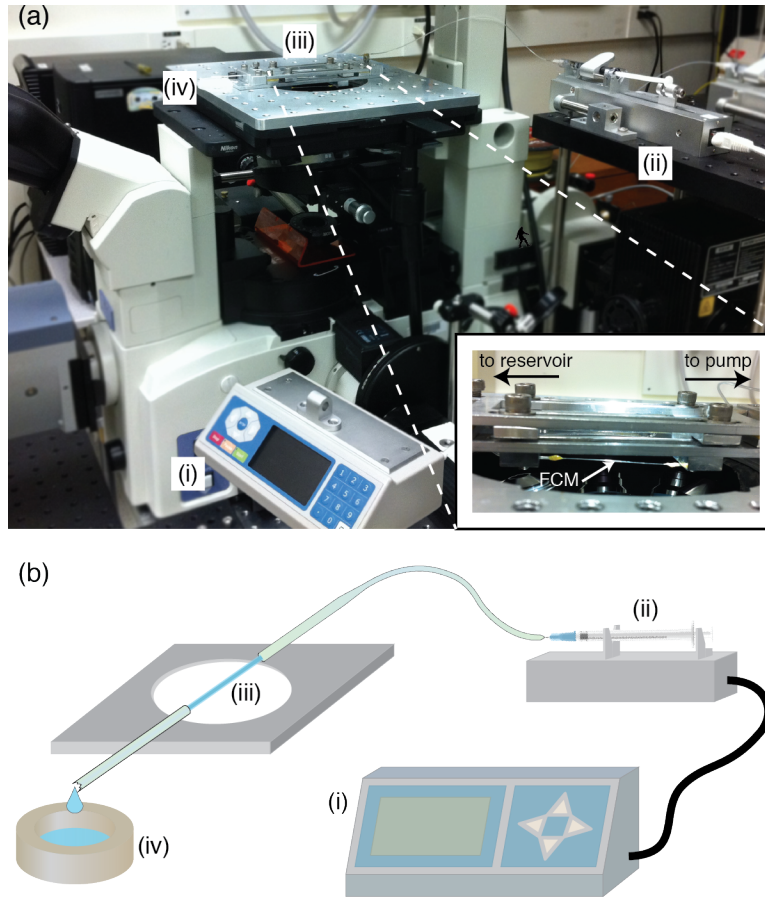
Figure 2.5: Microfluidic pumping apparatus. (a) Photograph and (b) schematic depicting the components of the microfluidic apparatus: (i) Nanojet pump controller, (ii) syringe pump and syringe, (iii) FCM mounted on the microscope stage, and (iv) fluid collection reservoir.

2.4.2   Effect of temperature fluctuations

Irradiation with laser light can induce heating of the target. In this investigation, laser light was used as an excitation source for the NC film, possibly raising the temperature of the sample in the process. Changes in temperature can induce changes in the optical cavities,

resulting in unexpected and/or unaccounted for errors in the fluorescence WGM spectra. Most notable are the thermo-optic and thermo-mechanical effects, both of which have been shown to be measurable in optical ring cavities [102, 103]. In an attempt to quantify the extent of any thermally-driven changes in the fluorescence spectra of the sample, two tests were performed. First, a Type-I FCM was exposed to $100\,\text{mW}$ laser radiation from the $488\,\text{nm}$ line of a Ar laser for $3.5\,\text{hrs}$, while continuously monitoring the fluorescence spectrum of the sample. The laser power used in this investigation was roughly 2.5 times the power used when measuring the refractometric sensitivity. Second, Type-I and Type-II FCMs were exposed to gradually increasing laser power, again continuously monitoring the PL spectrum. The power was increased step-wise from $9\,\text{mW}$ to $116\,\text{mW}$. At each step a PL spectrum was collected with an exposure time of $60\,\text{s}$.

Chapter 3

Results

3.1   Sample evaluation

The relative success of the sample preparation was determined by analyzing the PL from the sample both visually and spectroscopically. "Successful" samples were those that showed highly-visible WGMs in their PL spectra. Though this could have been investigated using brute-force, taking a spectrum of every sample, a significant amount of time was saved by exploiting some visual trademarks of unsuccessful samples. Most obviously, some samples ($1/8 - 1/4$ of the total of any given batch) did not exhibit any visible PL. This was likely due to a clog in the capillary that prevented the precursor solution from filling the channel. Roughly half of the samples in each batch exhibited bright orange PL emanating from the capillary core (Fig. 3.1a). Although bright and uniform, this PL did not appear to originate from the edges of the central channel, as would be expected for well-developed WGMs. Rather, the PL was concentrated in the middle of the core. An SEM micrograph of one such sample revealed a cylinder-like solid protruding from the capillary (Fig. 3.1b), suggesting the HSQ was not deposited onto the walls of the capillary during annealing. Instead it agglomerated in the capillary core producing long structures running the length of the capillary. These samples did not exhibit any WGMs in their PL spectra. The QD films in successful capillary samples were generally featureless and appeared smooth, with the exception of some defects and impurities (Fig 3.2). Fluorescence images of the samples revealed an orange-red PL emission from the capillary core. The central channel was well defined, with very little light coming from the capillary walls. The PL was concentrated

at the edges of the capillary core, and an end-on view of the cleaved capillary revealed a ring-like band of PL defining the QD film, confirming that the emitted PL was confined to the high-index QD film.
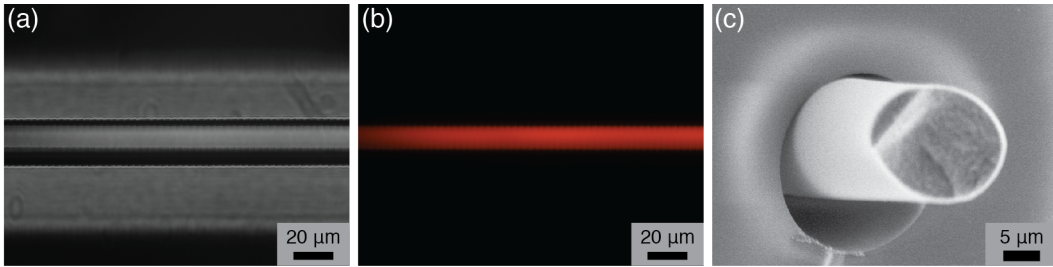
Figure 3.1: Unsuccessful sample. (a) Transmitted light image showing a solid structure in the capillary core that emits orange fluorescence (b). (c) SEM micrograph of such a sample showing a solid structure protruding from the central channel.
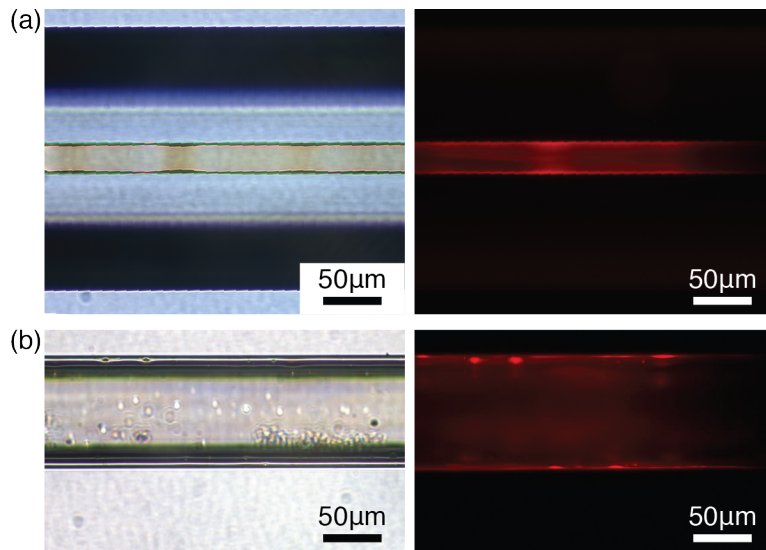
Figure 3.2: Transmission (left) and fluorescence (right) images of a (a) $25\,\mu$m ID and (b) $100\,\mu$m ID capillary coated with a QD film. The film appears beige in transmission. Fluorescence is concentrated at the edges of the capillary's central channel.

In rapidly cooled samples (*i.e.,* cooled over $\sim 1\,$hr) fluorescence images revealed an oscillatory change in PL intensity along the length of the capillary (Fig. 3.3). This was not observed in samples that were cooled over a longer period of time ($\sim 12\,$hrs). These oscillations may be attributed to changes in film thickness, though no direct measurements of the film thickness could be made inside the capillary channel.

The most important parameter controlling the success of the sample preparation was the concentration of the HPS. In Ref. [91], QD films were fabricated in capillaries with $25\,\mu$m, $50\,\mu$m, and $100\,\mu$m IDs using the same stock precursor solution used in this thesis [93].

Figure 3.3: Oscillations in the PL from QD films were observed in rapidly cooled samples. (a) $25\,\mu$m ID FCM that was cooled over a 12 hr period after annealing. (b) Similar sample cooled in 1 hr.

However, WGMs were not observed in the case of the $100\,\mu$m capillaries, attributed to the fabrication of a relatively thick film in these large structures, which was prone to cracking and delamination. This was overcome in the current work by diluting the stock solution for larger capillary sizes, as described in Sec. 2.1.3.1. However, WGMs were also absent from the PL spectra if the precursor solution was too dilut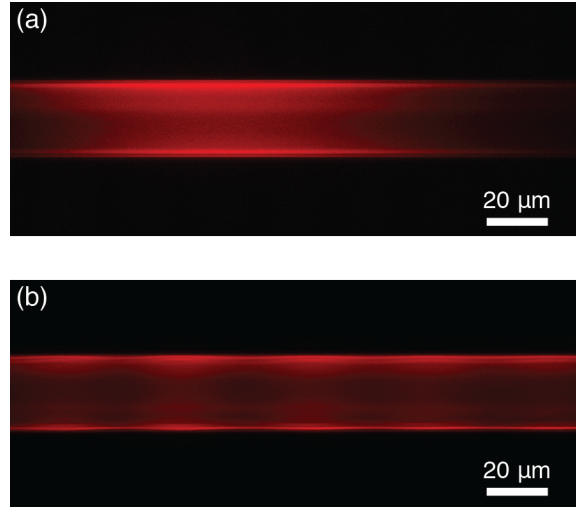e. This can be attributed to the fabrication a very thin QD film; *i.e.*, too thin to support WGMs. Thus, for smaller capillary sizes the precursor solution was concentrated, as described in Sec. 2.1.3.2.

Initially the sHPS was sufficient for fabricating films in $25\,\mu$m ID capillaries. However, over time this method began to fail to produce samples exhibiting WGMs. The PL from these samples appeared similar to other samples that did exhibit WGMs with the exception that the overall intensity was substantially lower, indicating the precursor solution was too dilute. Indeed, concentrating the stock solution resulted in successful samples once again. This somewhat anomalous behaviour in the sample preparation may be attributed to on going degradation of the stock solution, which may have resulted in a lower effective solution concentration. Ultimately, the sHPS had to be concentrated for the $25\,\mu$m ID samples, and diluted for $50\,\mu$m, $75\,\mu$m and $100\,\mu$m ID samples. The sHPS would also likely require concentration for the preparation of $10\,\mu$m samples and, indeed, this was attempted, however, the $10\,\mu$m samples were too easily clogged and no successful samples were fabricated. The concentration of the HPSs that were used to successfully fabricate samples exhibiting WGMs are shown in Table 3.1. Note that the concentrations quoted in

Table 3.1 are in reference to the original stock precursor solution concentration, neglecting any possible oxidation, *i.e.,* the sHPS would be quoted as 18% w/w.

Table 3.1: Concentration of the HSQ precursor solutions used in the fabrication of the FCMs

Capillary ID (μm)	Precursor concentration* (% w/w HSQ)	Success rate $\pm 5\%$
10	N/A	no successful samples
25	25	20%
50	12.5	30%
75	8	80%
100	2	20%
* - assuming a stock solution concentration of 18% w/w HSQ in MIBK		

3.2 Materials characterization

The presence of Si-NCs in the prepared films was confirmed by performing TEM on a spin-coated HSQ-annealed film. The bright-field micrograph of this film, shown in Fig. 3.4, clearly indicated regions of crystallinity in the film. Specifically, the lattice planes of nanocrystalline regions $\sim 2-4$ nm in size were observed. The visible lattice fringes, as well as the selected-area electron-diffraction patterns, confirmed the presence of nanocrystalline silicon.
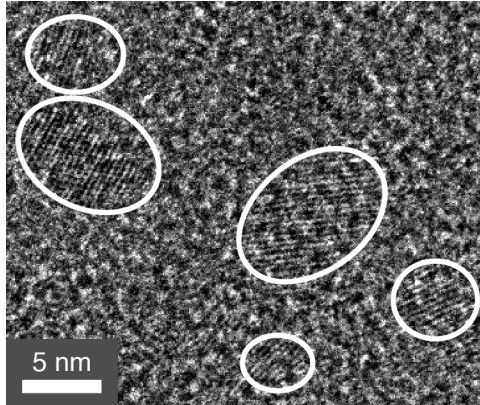
Figure 3.4: TEM micrograph of an annealed HSQ film obtained by X.Y. Wang. Regions of crystallinity are highlighted for clarity. Electron diffraction (not shown) confirmed the presence of randomly-oriented Si-QDs.

SEM was performed on both flat and capillary samples. Films on flat samples were readily identifiable due to the significant contrast between the Si substrate and the Si-NC/SiO$_2$ film. The triply spin coated/annealed films used in ellipsometry had an average thickness of $\sim 1.6 \pm 0.3 \mu$m (Fig. 3.5a). This value was used as a starting parameter for the Cauchy fitting used to obtain the optical constants (Sec. 3.3). In general, SEM images

of the films in capillaries were difficult to obtain because there is little contrast in both backscattered and secondary electron imaging when comparing the SiO_2 capillary to the Si-NC/SiO_2 film. Furthermore, the film was generally well-adhered to the capillary and did not fracture or separate from the capillary upon mechanical cleaving. In an attempt to induce fracturing and separation of the film some samples were cleaved by hand, by "snapping" the capillary in two, and others were gently ground using a mortal and pestle. However, neither method produced samples in which the film could be clearly imaged. Essentially, it was necessary to rely on a few fortuitous cases when a poorly adhered film separated from the capillary wall and could be seen protruding from the end of the capillary. One such case is shown in Fig. 3.5b in which a film was extending out of a $50\,\mu$m ID capillary. The film, roughly $0.5 - 1\,\mu$m thick, appeared smooth and uniform, though only a small length was imaged.
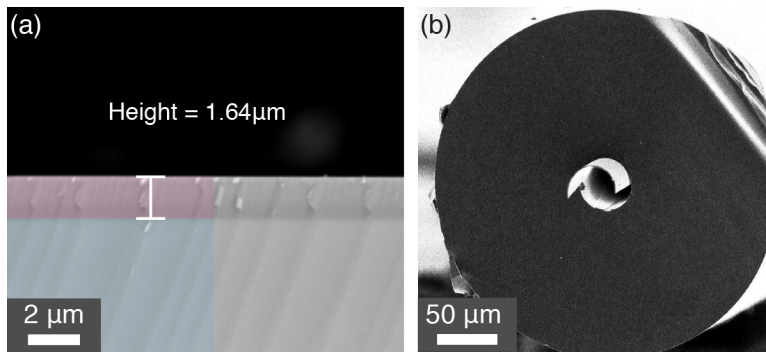
Figure 3.5: SEM micrographs of annealed HSQ films. (a) Cross section of a triply spin coated film on a flat Si substrate, with a measured thickness of $1.64\,\mu$m. False colour on left for clarity. (b) Film extending from core of glass capillary.

3.3 Determination of Optical Constants

The complex refractive index of the HSQ films was obtained by performing variable angle spectroscopic ellipsometry (VASE) on a flat, spin-coated film (see Sec. 2.2). The reflection signal was monitored while scanning the incident wavelength from 300 to 1700 nm. The signal was collected at reflection angles of $65°$ and $75°$. At both angles the reflection spectra showed oscillations in signal with increasing wavelength (Fig. 3.6a). These oscillations generally both broadened and increased in amplitude at longer wavelengths. The signal diminished rapidly at short wavelengths.

Reflection data was analyzed using a Cauchy model for the refractive index. In this

model, the complex refractive index, given by

$$\tilde{n} = n(\lambda) + i\kappa(\lambda) \tag{3.1}$$

is fit to several parameters. The real component of the refractive index, $n(\lambda)$, is approximated as

$$n(\lambda) = A + \frac{B}{\lambda^2} + \frac{C}{\lambda^4} \tag{3.2}$$

and the extinction coefficient, $\kappa(\lambda)$, is approximated as

$$\kappa(\lambda) = \alpha e^{\beta\left(12400\left(\frac{1}{\lambda} - \frac{1}{\gamma}\right)\right)} \tag{3.3}$$

where the constants A, B, C, α, and, β are fitting parameters and γ is the band edge of the material. The film thickness is also a free parameter in the model. This was initially estimated using SEM (see Section 3.2). $n(\lambda)$ and $\kappa(\lambda)$ were obtained by iteratively adjusting the fit parameters, calculating the theoretical reflection spectrum of the thin-film structure, and minimizing the residuals of the fit to the experimental reflection data.

The model fit converged reasonably well (Figure 3.6a). Peak positions were accurately reproduced, however the observed oscillation amplitude was smaller than predicted. The resulting spectra of $n(\lambda)$ and $\kappa(\lambda)$ are shown in Fig. 3.6b. In the region of Si-NC luminescence ($\sim 700 - 900\,\text{nm}$, see Section 3.1) n ranged from 1.666 to 1.677 and κ ranged from 0.0003 to 0.001, with average values around $800\,\text{nm}$ of 1.672 and 0.0006, respectively. This result confirmed that the refractive index of the film was larger than that of the glass capillary (*i.e.* $1.67 > 1.45$). Thus, this structure can support WGMs at the film-glass interface. The measured refractive index value of 1.672 is consistent with values measured in thin SiO_x films for $x \sim 1.5$ [104], and porous nanocrystalline Si films [105]. It is also consistent with the empirically-predicted value in Ref. [91] for a Si-NC film fabricated in a similar fashion, using an HSQ precursor solution.
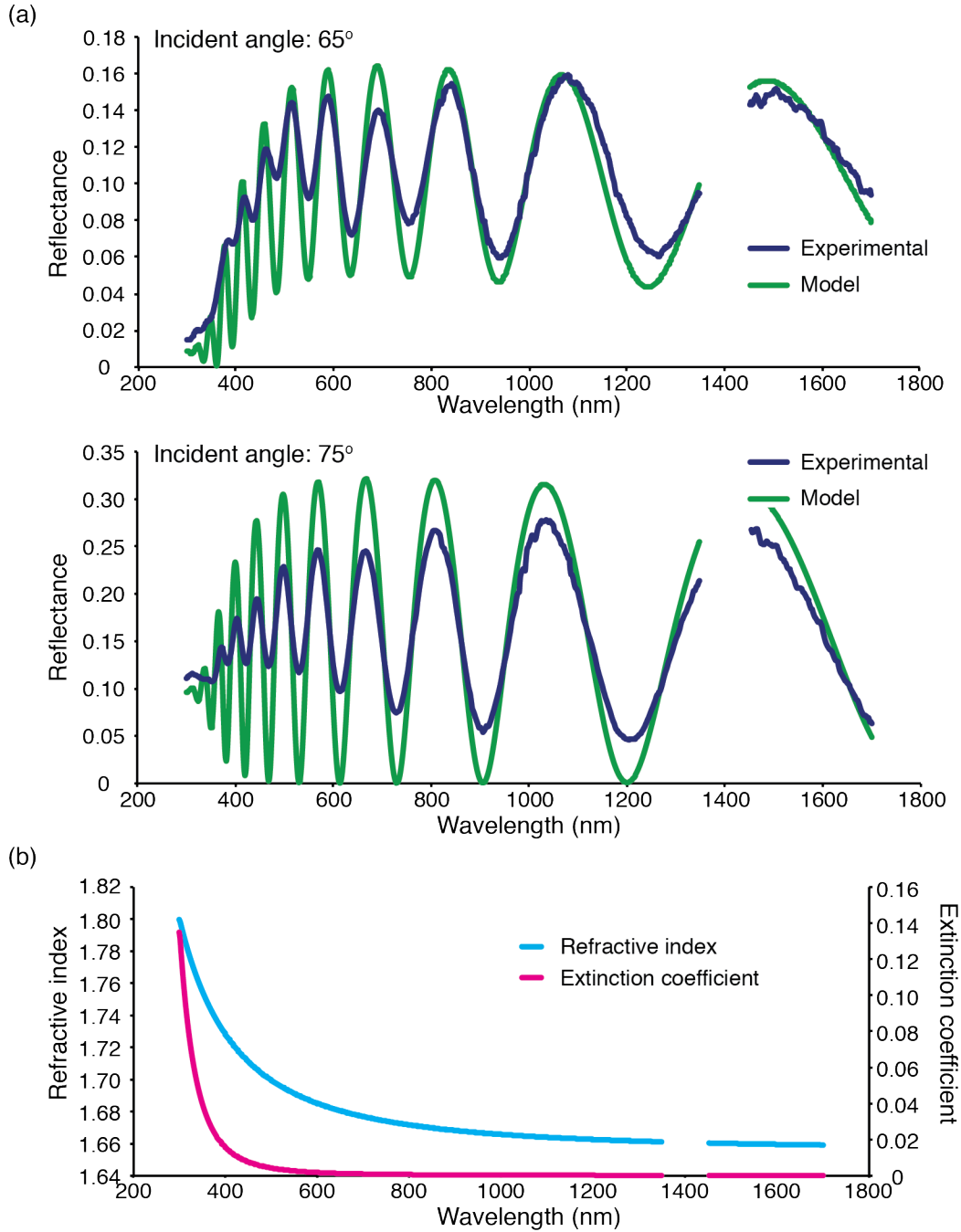
Figure 3.6: (a) Experimental and fitted model VASE reflectance data for a flat annealed HSQ film for incidence angles of 65° and 75°. (b) Calculated refractive index n and extinction coefficient κ from model fit. Data was not collected for wavelengths between 1340 nm and 1450 nm due to high absorption in the detector fibre.

3.4 Optical Spectroscopy

3.4.1 Photoluminescence and whispering gallery mode spectra

The PL spectra from capillary samples showed a broadband background with superimposed intensity modulations consistent with the formation of WGMs in the QD film (Fig. 3.7).[1] The background was similar to the PL observed from flat films (Fig. 3.7, inset). Two sets of modes could be clearly identified in the PL spectrum, corresponding to the two different WGM polarizations: TE_z (electric field is polarized along the capillary axis) and TM_z (magnetic field polarized along the capillary axis). The z-direction here is defined parallel to the capillary axis, and the polarization is defined with respect to the plane of propagation. The two polarizations were isolated by inserting a linear polarizer after the microscope objective When the polarizer was aligned parallel to the capillary axis only TE_z polarized WGMs were collected, conversely for TM_z modes. The Q factors of the TE_z and TM_z modes are similar, around 800, however the TE_z modes have a significantly greater intensity than TM_z modes.
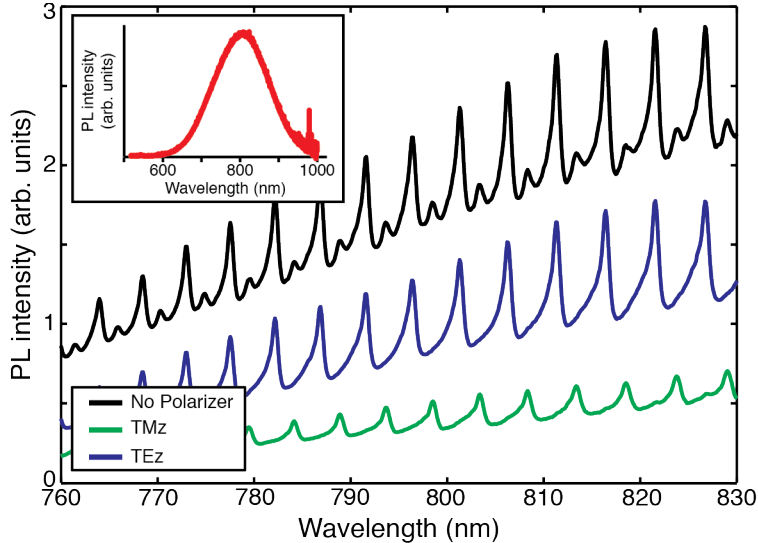
Figure 3.7: Polarization of WGMs in FCMs. With no polarizer (black) two sets of peaks can be observed, corresponding to the polarizations of WGMs. TE_z modes (blue) showed a significantly higher visibility than TM_z modes (green). *Inset* PL spectrum of a flat film.

The TE_z WGM spectra obtained for FCMs with IDs of $25\,\mu$m, $50\,\mu$m, $75\,\mu$m, and $100\,\mu$m are shown in Fig. 3.8. The free spectral range (FSR *i.e.*, spacing between successive peaks) and Q factors of the WGMs shown in Fig 3.8 are summarized in Table 3.2. The FSR in the

---

[1]The presence of WGMs in photoluminescence spectra is a result of the quantum mechanical phenomena known as the Purcell effect. See Appendix C.
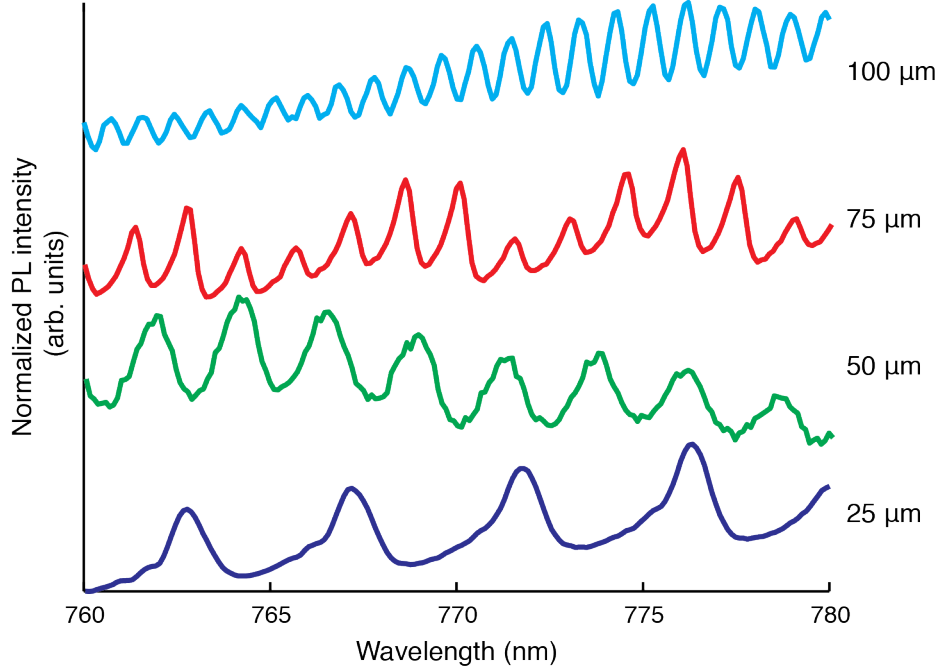
Figure 3.8: WGM spectra FCMs with IDs of $25\,\mu$m, $50\,\mu$m, $75\,\mu$m, and $100\,\mu$m, showing only TE_Z modes. The observed FSRs are consistent with those predicted by Eq. (3.4), See Table 3.2. Data sets normalized and offset for clarity.

spectral region shown decreases with increasing capillary diameter. This is expected from Eq. (1.19), which can be written as

$$\frac{\lambda_l}{n} = \frac{2\pi r}{l} \tag{3.4}$$

For the $25\,\mu$m ID samples the FSR observed in the spectral region shown in Fig. 3.8 was $\sim 4.5\,$nm; this decreased to $0.9\,$nm in $100\,\mu$m ID samples. The observed FSRs generally agreed with those predicted by Eq. (3.4). The observed Q-factors from the $25\,\mu$m and $50\,\mu$m capillaries were approximately 800. This increased to $1600 - 1800$ in the larger capillaries. The WGMs in some of the narrower capillaries exhibited asymmetry in their peak shape with a clearly defined skewing to short wavelengths. As discussed in Sec. 4.1, this asymmetry was most likely caused by a continuum of "spiraling" WGMs, that is WGMs that have a non-zero axial propagation constant.

Table 3.2: Observed and predicted free spectral range and measured Q of WGMs in Fig. 3.8.

Capillary ID (μm)	Observed FSR (nm $\pm$ 0.1 nm)	Predicted FSR at $\lambda_0 = 770$ nm (nm)	Q (approx.)
25	4.5	4.5	800
50	2.3	2.3	800
75	1.5	1.5	1800
100	0.9	1.1	1600

3.5   Refractometric sensing

3.5.1   Laser excitation

Several aqueous solutions of sucrose were pumped through the capillary samples, incrementally increasing the refractive index of the core in steps of 0.012 RIU from 1.333 RIU (distilled water) to 1.453 RIU (concentrated sucrose solution). A PL spectrum was collected at each refractive index step, after the solution was pumped through the capillary. WGMs can be observed in these samples with exposure times $\lesssim 10$ s, however, for this experiment spectra were collected with an exposure time of 240 s in order to minimize noise in the spectra and aid in eventual peak fitting. To avoid overlapping modes of different polarization in the PL spectra a linear polarizer was used to select only TE_z WGMs, because of their high visibility.

As the refractive index of the fluid was increased, a red-shift in the WGM spectrum was observed in both the Type-I (25 μm ID, Fig. 3.9) and Type-II (100 μm ID, Fig. 3.10) FCMs. This is the first reported instance of refractometric sensing using FCMs. For the Type-I FCM a total spectral shift was approximately 1.1 nm over a refractive index range of $n = 1.333 - 1.453$. In the case of the Type-II FCM the index range was $n = 1.333 - 1.423$, as spectra corresponding to higher indices were too noisy to accurately assign peak values. Over this range the total observed shift was approximately 0.65 nm. The average sensitivity of the Type-I FCM, estimated using a linear least-squares fit to a straight line, was 9.8 nm/RIU over the noted refractive index range. For the Type-II FCM the average sensitivity was 6.8 nm/RIU.
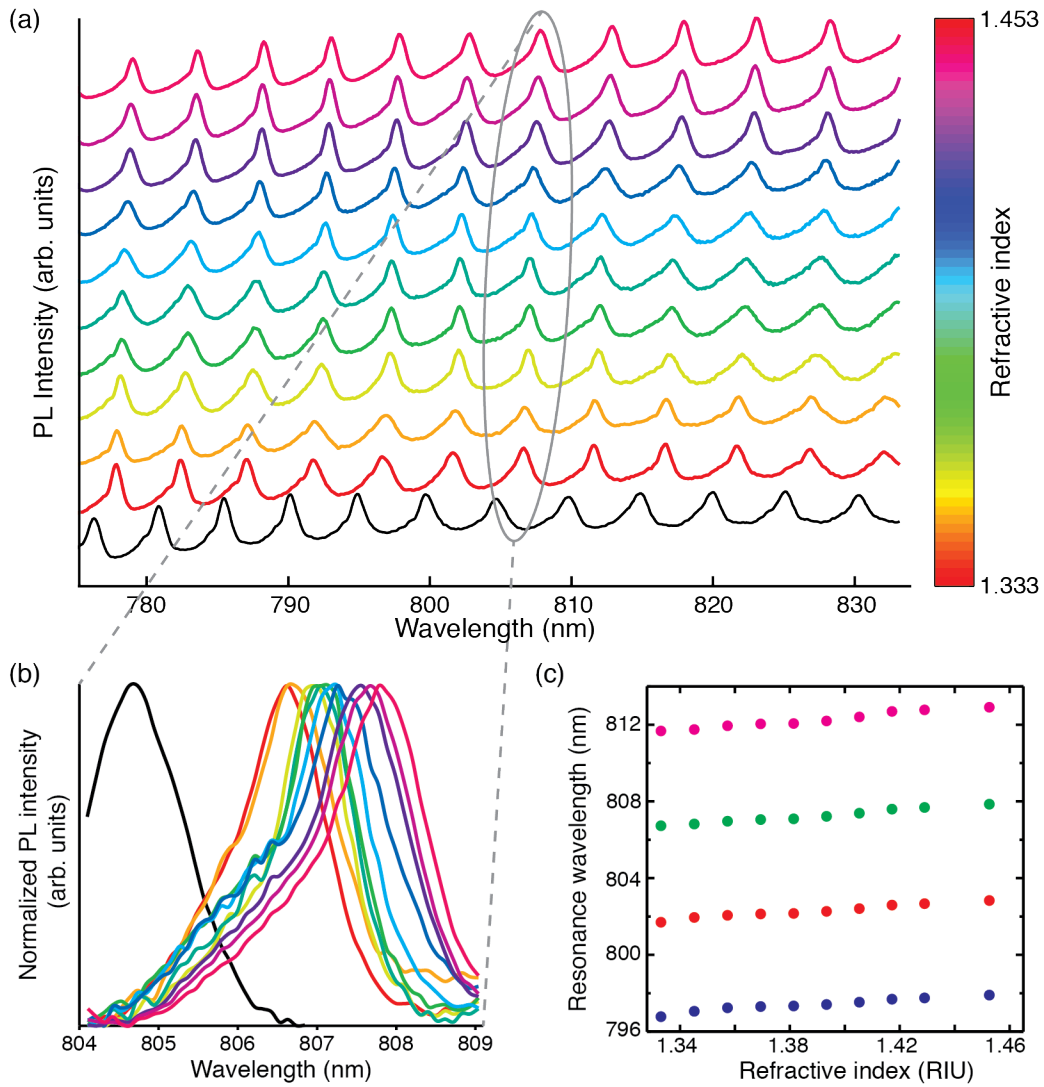
Figure 3.9: (a) Shift in the WGM spectrum of a Type-I FCM upon injection of sucrose solutions. Spectra offset for clarity. Coloured spectra correspond to the refractive index scale on the right. The spectrum in black was collected prior to solution injection, with only air ($n = 1.0$) in the FCM core. The spectra were collected using an Ar-ion laser as an excitation source. (b) Shift of a single WGM. (c) Resonance wavelength of four neighboring WGMs.

Figure 3.10: Shift in the WGM spectrum of a Type-II FCM upon injection of sucrose solutions (refractive index scale at right). Spectra offset for clarity. The spectra were collected using an Ar ion laser as an excitation source. *Inset* Resonance shift of single mode (indicated by vertical line on spectrum). The observed sensitivity was 6.8 nm/RIU.

3.5.2 LED excitation

An LED was used as an excitation source in order to demonstrate that a laser is not required in the operation of the FCMs. A laser is an expensive component for a viable microfluidic apparatus and the ability to replace it with an LED would increase the cost efficiency of any FCM-based device. Spectra were collected for a Type-I FCM with an exposure time of 240 s; WGMs were again observed in the PL spectra (Fig. 3.11). Six sucrose solutions ranging in refractive index from $1.333 - 1.453$ (solutions 1, 3, 5, 7, 9, and 11 from Table 2.2) were pumped through the sample. Again a red shift in the WGM spectrum was observed upon increasing refractive index of the core. The total shift observed in this sample was approximately 0.6 nm. The difference in the magnitude of the observed shifts between the laser-excited and LED-excited samples is due to differences in the samples, most likely a difference thickness of the QD film in the two different analysis regions.
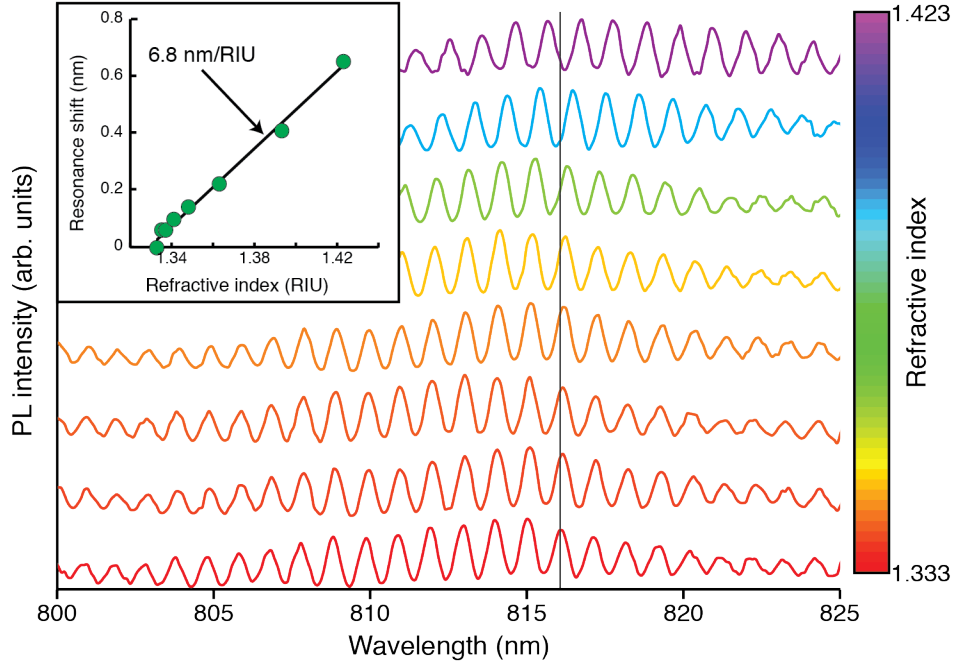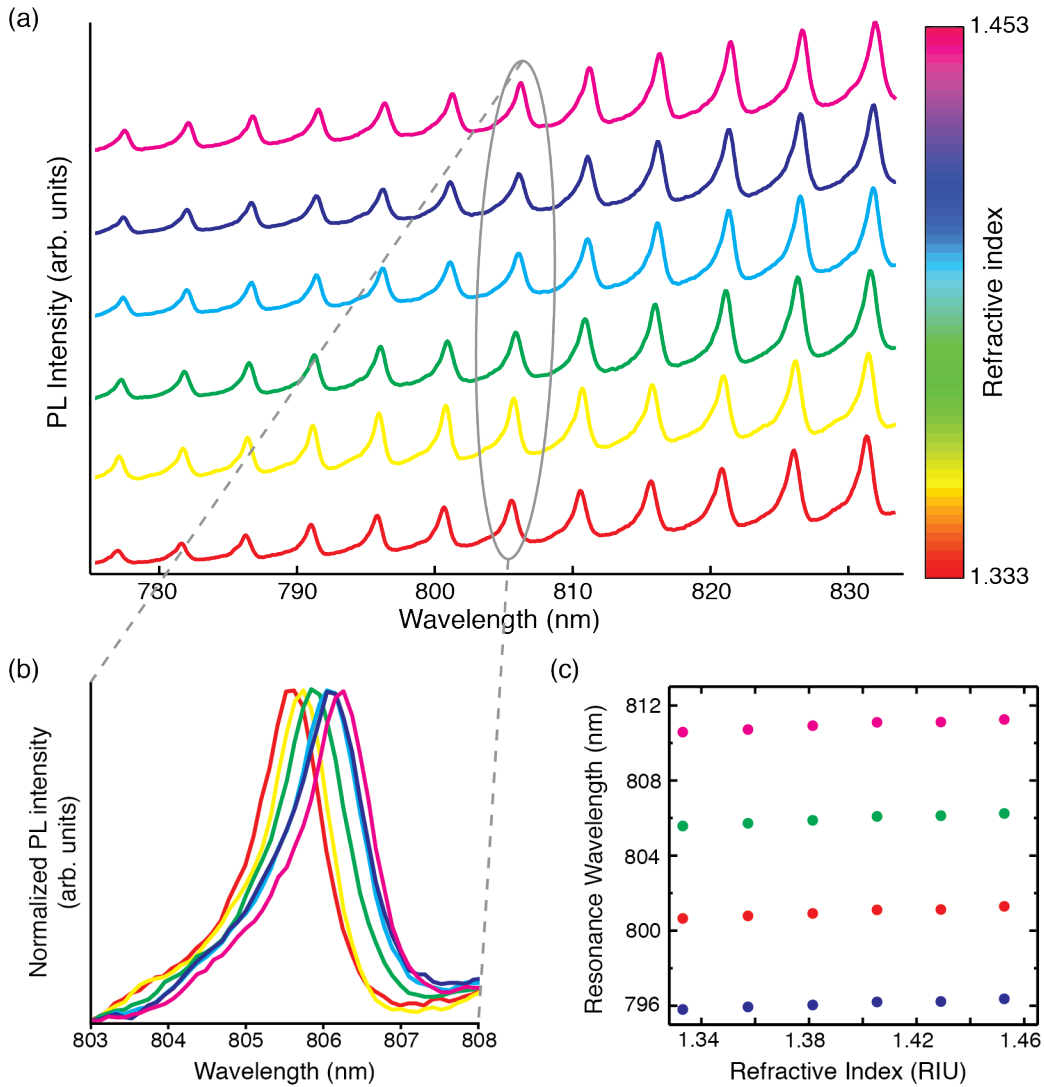
Figure 3.11: (a) Shift in the WGM spectrum of a Type-I FCM upon injection of sucrose solutions (refractive index scale at right). Spectra offset for clarity. The spectra were collected using an LED as an excitation source. (b) Shift of a single WGM. (c) Resonance wavelength of four neighboring WGMs.

3.5.3 Thermally induced resonance shifts

Two experiments were performed to determine if there were any thermal effects, such as laser-induced heating, that might influence the WGM shifts. In the first study the peak wavelength of the WGM resonances in Type-I and Type-II FCMs were monitored as a function of laser power. At each power a spectrum was collected for 60 s. The spectra collected for the Type-I FCM are shown in Fig. 3.12a. A small red shift was observed upon increasing the laser excitation power, giving a slope of approximately $0.4\,\mathrm{pm/mW}$ over

a power range of 9 to 116 mW incident on the sample, for a total shift of ~ 65 pm (Fig. 3.12b). The effect was slightly more pronounced in the Type-II FCM where the average shift was approximately $1.4\,\text{pm}/\text{mW}$ (Fig. 3.12c). These shifts were well outside the uncertainty in the peak position (Appendix A).
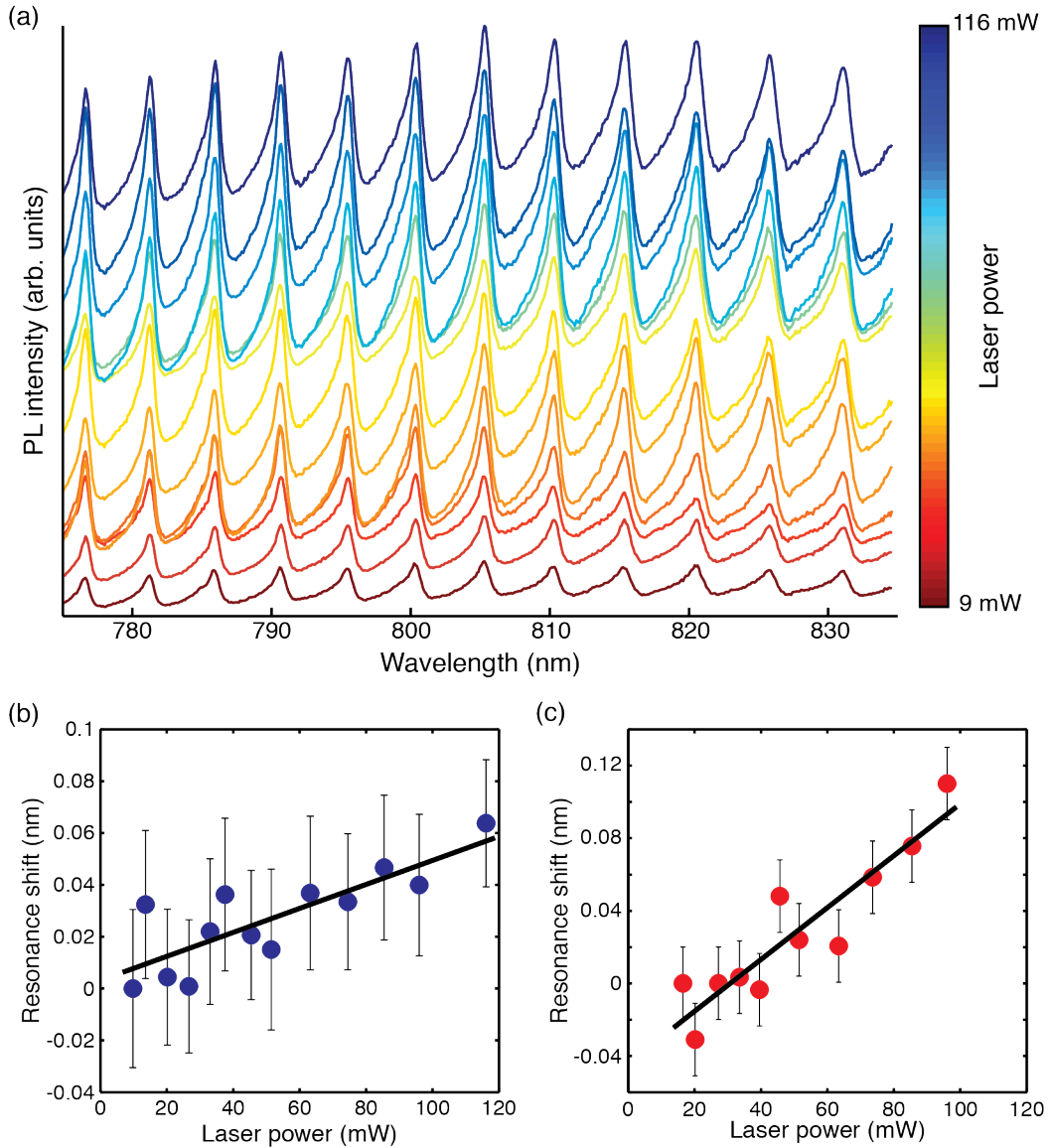
Figure 3.12: Spectral shift of a Type-I FCM as a result of increased laser power. Spectra are naturally scaled, but offset for clarity. The total measured resonance shift was (b) 65 pm for the Type-I FCM and (c) 110 pm for the Type-II FCM. Errors bars in (b) and (c) were calculated from the residuals of the peak fitting method used to identify the peak locations (see Appendix A).

In the second experiment the WGM spectrum of a Type-I capillary was monitored as it was continuously exposed to 100 mW (incident on the sample) laser irradiation. Spectra

were collected at regular intervals with an exposure time of 90 s. In total the sample was irradiated continuously for 3.5 hrs. The collected spectra are shown in Fig. 3.13, with the measured resonance shifts shown in the inset. The maximum observed shift was 49 pm.
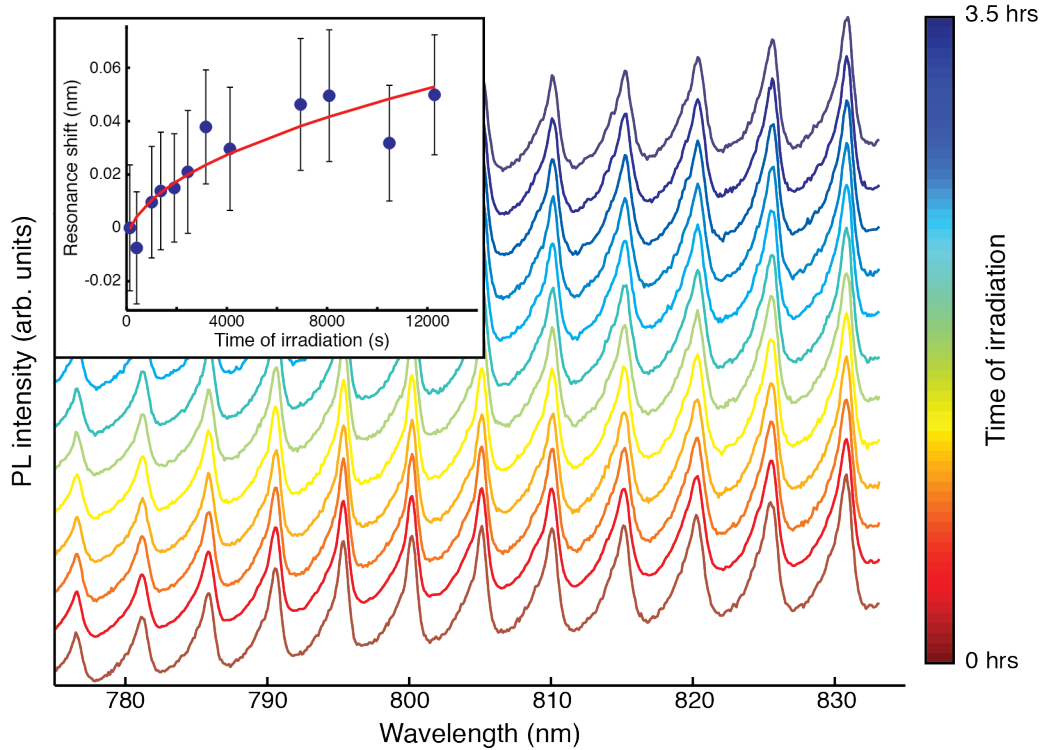
Figure 3.13: Spectral shift of a Type-I FCM as a result of prolonged exposure to 100 mW laser irradiation. Spectra are naturally scaled, but offset for clarity. *Inset* Time-dependent spectral shift, including $\sqrt{t}$ fit (see Sec. 4.2). The total observed shift was 49 pm. Errors bars were calculated from the residuals of the peak fitting method (Appendix A).

Chapter 4

Discussion

4.1 Peak shapes and fitting

The resonant wavelengths of the WGMs were determined by fitting a curve to each WGM peak (Appendix A). Modes from the Type-II capillary (Fig. 3.10 in Sec. 3.5) appeared symmetric and were well approximated with a Lorentzian lineshape:

$$I(\nu) = \frac{\gamma}{\pi} \left[\frac{A}{1 + (\frac{\nu - \nu_0}{\gamma})^2} \right]$$
(4.1)

where A is an amplitude scaling parameter, ν_0 specifies the central peak frequency, and γ is the peak-width parameter, equal to the half-width at half-maximum of the peak. The Q factor of a Lorentzian is defined in in terms of the parameters ν_0 and γ:

$$Q = \frac{\nu_0}{\Delta \nu} = \frac{\nu_0}{2\gamma}$$
(4.2)

where $\Delta \nu$ represents the FWHM of the peak. When $A = 1$ Eq. (4.1) becomes the Cauchy probability distribution, with unit area.

WGM peaks from the Type-I capillary were clearly asymmetrical and skewed towards shorter wavelengths (Figures 3.9 and 3.11 in Sec. 3.5). This effect was visible in both TE_z and TM_z modes and was observed regardless of the use of the polarizer. It is unlikely that these apparent sidebands are a result of the overlap of higher order radial modes ($\rho > 1$). Such modes would have a greater refractometric sensitivity than the main peaks, causing a relative shift between the two as the refractive index was changed. This is inconsistent

with the observation that the main peaks and the sidebands maintained a constant spectral relationship over the entire refractive index range. In contrast, so called "spiral modes" (modes with a non-zero k_z component) can appear as a family of overlapping peaks on the high-frequency side of a resonant mode [106]. Such spiraling modes have been observed in evanescently-coupled silica capillaries [60]. In FCMs, spiraling modes represent a continuum of higher-frequency peaks with intensities that decay away from the main WGM maximum, consistent with the data.

Since it is not practical to attempt to derive a lineshape that corresponds to a continuum of decaying Lorentzians of uncertain amplitudes, two empirical lineshapes were used to analyze the data. The first was a sum of two standard Lorentzians, and the second was a "skewed" Lorentzian. The "two mode" lineshape is given by

$$I(\nu) = \frac{A_1}{1 + (\frac{\nu - \nu_1}{\gamma_1})^2} + \frac{A_2}{1 + (\frac{\nu - \nu_2}{\gamma_2})^2} \tag{4.3}$$

where the subscripts 1 and 2 denote parameters of the two peaks. A_i are intensity scaling parameters, ν_i are the resonance frequencies of the peaks, and γ_i are the linewidths. The skewed Lorentzian lineshape, first derived in Ref. [107], is given by

$$I(\nu) = \frac{A}{1 + (\frac{\nu - \nu_0}{\gamma(\nu)})^2} \tag{4.4}$$

where the Lorentzian linewidth parameter γ has been replaced by a "skewing function" $\gamma(\nu)$, which varies with frequency. This skewing function allows the peak width γ to vary over the range of the peak. Best results were obtained when $\gamma(\nu)$ was chosen as a sigmoid function:[1]

$$\gamma(\nu) = \frac{(1 + b_2)\gamma_0}{1 + b_2 e^{-b_1(\nu - \nu_0)}} \tag{4.5}$$

where b_1 and b_2 are fitting parameters controlling the asymmetry of the peak and γ_0 is the "natural" Lorentzian linewidth. Negative values of b_1 skew the to peak to lower frequencies, while positive values of b_1 skew the peak to higher frequencies (as is the case for the observed FCM spectra). The parameter b_2 introduces an asymmetry to the variation of the peak width about the central frequency. Equation (4.5) is scaled such that the peak width is equal to the natural peak width at the resonance frequency:

---

[1]A sigmoidally modified Lorentzian function, similar to Eqs. (4.4) and (4.5), has previously been used to estimate the lineshapes of asymmetric infrared absorption peaks [107].

$$\gamma(\nu_0) = \gamma_0 \qquad (4.6)$$

When b_1 or b_2 (not necessarily both) is equal to zero, $\gamma = \gamma_0$ for all values of ν, and $I(\nu)$ is a pure Lorentzian with $FWHM = 2\gamma_0$.

Both lineshapes described the shape of the observed peaks, particularly near the central peak frequency. The two-mode and skewed Lorentzian functions consistently returned fits with $R^2 > 0.98$ and 0.95, respectively, indicating that Eq. (4.3) yielded a slightly higher correlation to the data. However, in many circumstances both functions resulted in fits with $R^2 > 0.99$. The two functions often returned slightly different results for the absolute peak values (ν_0), however the relative peak shifts were found to be essentially identical.
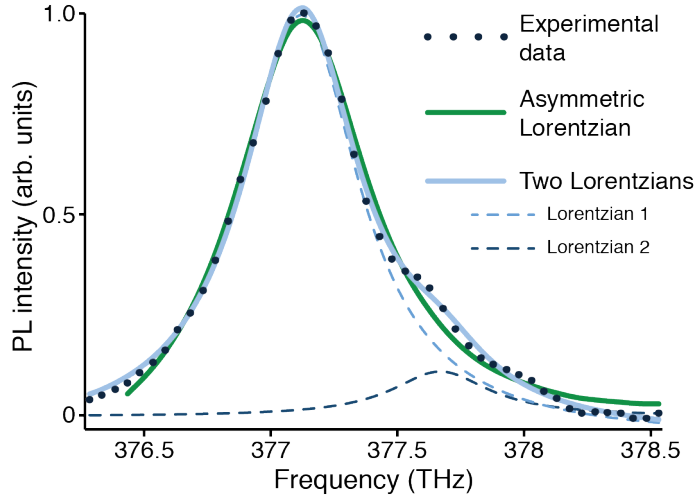
Figure 4.1: Comparison of the two functions used to fit the resonance peaks in the Type-I FCM. Two curves were fit to the experimental data (dots): an asymmetric Lorentzian (solid green, $R^2 = 0.992$), and the sum of two standard Lorentzians (single Lorentzians, dashed; sum, solid blue; $R^2 = 0.998$).

4.2 Thermal fluctuations

In FCMs there are two primary effects resulting from temperature fluctuations that may inadvertently influence the WGM spectra: thermal expansion of the structure and thermal modification of the optical constants of the materials. These effects can result in unaccounted-for changes in the WGM spectra. In experiments such as these, thermal fluctuations may be caused by exposure to laser light, required to pump the QD fluorescence [108, 109]. For simplicity, the laser-induced heating in a layered structure (a planar

analogue to an FCM, Fig. 4.2a) was modeled following the procedure outlined in Ref. [109].

Heat flow in a material is governed by the heat equation:

$$\frac{\partial^2 T(x,t)}{\partial x^2} = \frac{1}{\alpha_s}\frac{\partial T(x,t)}{\partial t} \tag{4.7}$$

where α_s is the thermal diffusivity, defined in terms of the thermal conductivity k_s, heat capacity c_p, and density ρ_s of the material:

$$\alpha_s \equiv \frac{k_s}{c_p \rho_s} \tag{4.8}$$

Heating from the laser excitation spot yields the condition

$$-k_s\frac{\partial T(x,t)}{\partial x} = A_s P \tag{4.9}$$

where P is the power density of the laser light and A_s is the absorptivity of the material. The resulting temperature profile can be written as

$$T(x,t) = T_s(t)e^{-x/\delta(t)} \tag{4.10}$$

In Eq. (4.10), $T_s(t)$ is the time-dependent temperature of the irradiated surface and $\delta(t)$ is the time-dependent temperature penetration depth. These quantities are given by

$$T_s(t) = T_0 + \frac{A_s P}{\sqrt{c_p \rho_s k_s}}(2t)^{1/2} \tag{4.11}$$

$$\delta(t) = \sqrt{2\alpha_s t} \tag{4.12}$$

Equations (4.10), (4.11), and (4.12) indicate that the temperature of the material increases as $t^{1/2}$ and decays exponentially into the bulk.

The heating predicted in Eq. (4.10) can induce thermal expansion and thermo-optic effects in the FCM. Thermal expansion changes the physical size or shape of the resonator. The QD film, capillary walls, and capillary channel can all be affected to a different degree, causing changes to the capillary diameter and QD film thickness. The thermo-optic effect is the thermally-induced modification of the refractive index of a material. Generally, thermal expansion causes changes to the parameters r, b, and $d = r - b$, while the thermo-optic effect modifies n_1, n_2, and n_3; all of these parameters control the WGM resonance wavelengths

(Fig. 4.2b).
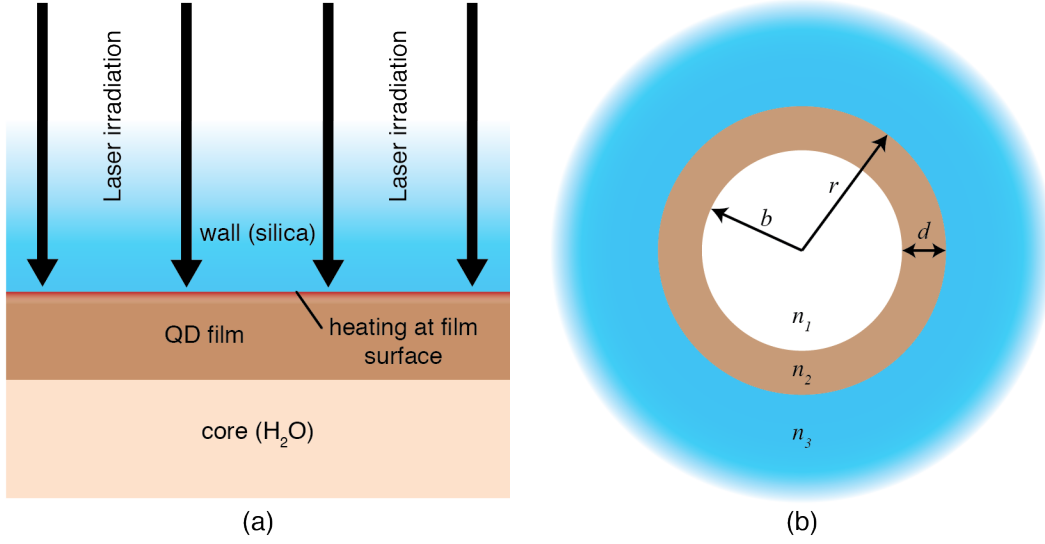
Figure 4.2: Schematic of structures used in thermal analysis: (a) laser-induced heating, and (b) thermo-mechanical and thermo-optic effects

WGMs in FCMs can be treated in terms of the simple resonance condition presented in Eq. (1.19) [103]:

$$l\lambda_l = 2\pi r n_{eff} \qquad (4.13)$$

where r is the outer radius (Fig. 4.2), λ_l is the WGM resonance wavelength of azimuthal order l, and n_{eff} is the effective index of the mode. The effective index depends on the geometry of the device and the mode profile of the WGM. For a given radius, n_{eff} will depend on the refractive indices of the layers, and the film thickness:

$$n_{eff} = f(n_1, n_2, n_3, d) \qquad (4.14)$$

where n_1, n_2, and n_3 are the refractive indices of the core, film , and walls, respectively. The shift in WGM wavelength as a result of thermal expansion and thermo-optic effects can be extracted from Eq. (4.13):

$$\frac{\delta\lambda}{\lambda} = \frac{\partial r}{\partial T}\frac{1}{r}\delta T + \frac{\partial n_{eff}}{\partial T}\frac{1}{n_{eff}}\delta T \qquad (4.15)$$

The first term in Eq. (4.15) represents the contribution due to thermal expansion. This is a combined effect resulting from the net expansion of the core, film, and walls, and is

governed by the linear thermal expansion coefficient α (units K^{-1}):

$$\alpha \equiv \frac{\partial r}{\partial T} \frac{1}{r} \qquad (4.16)$$

The second term in Eq. (4.15) represents the thermo-optic contribution to the resonance shift. Here the derivative term can be expanded using Eq. (4.14):

$$\frac{\partial n_{eff}}{\partial T} = \kappa_1 \frac{\partial n_{eff}}{\partial n_1} + \kappa_2 \frac{\partial n_{eff}}{\partial n_2} + \kappa_3 \frac{\partial n_{eff}}{\partial n_3} + \alpha_2 \frac{\partial n_{eff}}{\partial d} \qquad (4.17)$$

where κ is the thermo-optic coefficient of the specified material, defined as:

$$\kappa \equiv \frac{\partial n}{\partial T} \qquad (4.18)$$

Assuming the QD layer and the capillary walls have the same thermal expansion and thermo-optic coefficients, the expected spectral red-shift would be on the order of $10\,\text{pm/K}$ [103]. Upon exposure to increasing laser power, the observed shifts were $\sim 0.4\,\text{pm/mW}$ for the Type-I FCM and $\sim 1.4\,\text{pm/mW}$ for the Type-II FCM (see Fig. 3.12 in Sec. 3.5.3). Since the laser was stable within $1\,\text{mW}$, this contributes a maximum experimental error of $1.4\,\text{pm}$ to the peak location. Upon prolonged exposure to $100\,\text{mW}$ laser irradiation the WGM peak shifts followed a $\sqrt{t}$ curve, in accordance with Eq. (4.11) (Fig. 3.13 in Sec. 3.5.3), up to a maximum shift of $49\,\text{pm}$ after a $210\,\text{min}$ exposure. Each experimental spectrum (Sec. 3.5) was, however, collected over a maximum time of only $10\,\text{min}$. Thus, the heating-induced uncertainties contributed a maximum experimental error of $7\,\text{pm}$ to the spectral shift. Based on these observed shifts, the sample temperature therefore increased by $< 1\,\text{K}$ during the refractometric sensing experiments. These combined spectral uncertainties are significantly smaller than the observed shifts ($\sim 100\,\text{pm}$ per spectrum), and so we can confidently conclude that thermal fluctuations induced by the laser did not significantly contribute to the observed spectral shifts.

4.3 Numerical analysis

4.3.1 Finite-difference frequency-domain

The theoretical mode structure and refractometric sensitivity of the FCMs were calculated using a a finite-difference frequency-domain (FDFD) model, developed primarily by Josh

Silverstone. The basic operation of the code is described as follows. The z-component of the vector wave equation was isolated (*i.e.*, TE_z polarization, for consistency with the measurements) and forced into harmonic solutions, yielding the Helmholtz equation:

$$\frac{\partial^2}{\partial x^2} E + \frac{\partial^2}{\partial y^2} E + +n^2 k_0^2 E = 0 \qquad (4.19)$$

where $E = E_z$.[2] Finite difference approximations for the partial derivatives of the Helmholtz equation were used to discretize the solution over the computational domain:

$$\frac{\partial^2}{\partial x^2} E \approx \frac{E_{(i+1,j)} - 2E_{(i,j)} + E_{(i-1,j)}}{\Delta x^2} \; ; \quad \frac{\partial^2}{\partial y^2} E \approx \frac{E_{(i,j+1)} - 2E_{(i,j)} + E_{(i,j-1)}}{\Delta y^2} \qquad (4.20)$$

where indices i and j specify a particular computational cell, and $\Delta x / \Delta y$ are the spatial grid spacings. This discretization was formulated as a matrix eigenvalue problem, with the eigenvalue equal to the square of the resonant frequency and the eigenvector equal to the corresponding eigenmode of the cavity:

$$\Lambda_y^2 E_{(i,j-1)} + \Lambda_x^2 E_{(i-1,j)} - 2\left(\Lambda_x^2 + \Lambda_y^2\right) E_{(i,j)} + \Lambda_x^2 E_{(i+1,j)} + \Lambda_y^2 E_{(i,j+1)} = k_0^2 E_{(i,j)} \quad (4.21)$$

$$\Lambda_k^2 = -\left(\frac{1}{n_{(i,j)}\Delta k}\right)^2 , \; k = x, y \qquad (4.22)$$

$$A\bar{E} = \lambda \bar{E} \qquad (4.23)$$

Equation (4.23) represents the eigenproblem to be solved: $\bar{E}$, the eigenvector, is a vector containing every $E_{(i,j)}$ in the computational domain, $\lambda = k_0^2$ is the eigenvalue, and A is a sparse matrix composed of elements from Eq. (4.21). $\bar{E}$ and A have sizes of $N_x N_y$ and $N_x N_y \times N_x N_y$, respectively, where $N_{x/y}$ are the number of computational cells in the x and y directions. Radiating boundary conditions based on the "one-way" wave equations were used to remove optical energy from the computational domain. A small amount of reflection occurred at the boundaries for non-normal-incidence waves. This effect was found to be minor, as confirmed by varying the domain size and ensuring solution consistency. The

---

[2]For TE_z polarization all other electric field components are zero: $\mathbf{E}_{TE} = E_z \hat{z} \equiv E\hat{z}$; $E_r = E_\theta = 0$.

method permitted the resonance wavelength, Q-factor, and mode numbers ρ (the radial order) and l (the azimuthal order) to be extracted for any given TE_z mode, while also allowing considerable geometrical flexibility compared to analogous analytical methods.

The model was used to investigate the role of two key structural parameters in regards to RS: capillary ID and QD film thickness. A two-dimensional layered structure was simulated (inset Fig. 4.3): the inner layer corresponded to the analyte ($n_1 \approx n_{water} = 1.33$), the middle layer to the QD film ($n_2 = 1.67$), and the outer layer to the glass capillary ($n_3 = 1.45$). Because the capillaries were thick walled and the light was confined primarily within the QD layer, as shown in Fig. 4.3, the simulation domain did not include the outer air-boundary of the capillary. The numerical resonance shifts of WGMs in Type-I and Type-II capillaries were tracked over a refractive range roughly equivalent to that performed in experiment (*i.e.*, $n_1 \simeq 1.33 - 1.45$), for structures with film thicknesses ranging from 400 to 1000 nm (Fig. 4.4).
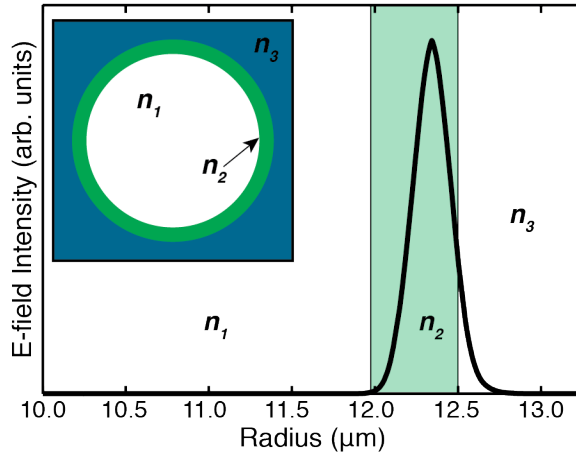
Figure 4.3: Radial field profile of a $\rho = 1$ WGM in a Type-I structure with a 525 nm QD film (highlight in green), calculated using the FDFD method. *Inset* Refractive index profile for FDFD simulations, showing the core (n_1), QD film (n_2), and capillary wall (n_3).

Results from the FDFD model revealed that the refractometric sensitivity (RS) depends primarily on three parameters: the capillary diameter, the QD film thickness, and the refractive index of the core. For a constant film thickness, the RS was generally higher in the larger-diameter (Type-II) structures (Fig. 4.4). This can be attributed to a larger fraction of the mode extending into the capillary core in the larger-diameter structures, consistent with results for LCORR structures [64]. The fact that this effect was not observed in experiment (Figures 3.9 and 3.10) is a result of the second key parameter: the QD film thickness.

The FDFD model revealed that the QD film thickness is the most dominant factor

governing the RS of the device. In both Type-I and -II structures the RS increases sharply upon reduction of the QD film thickness (Fig. 4.4, inset). However, the simulations also indicated that when the film becomes too thin the Q-factor of the mode degrades due to excessive loss into the capillary walls (*i.e.*, loss of confinement of the mode in the QD layer). Thus, obtaining the ideal film thickness involves a trade-off between sensitivity and the Q-factor required for peak fitting and measurement. The thickness of the QD film in the fabricated FCMs was estimated by comparing the observed shifts and RS to those calculated using the FDFD model. The calculated and observed shifts agreed well for a film thickness of approximately 525 nm for the Type-I FCM, and 650 nm for the Type-II FCM. Thus, though the larger capillary diameter of the Type-II FCM would indicate a higher sensitivity, a thicker film resulted in an overall reduction in the RS.
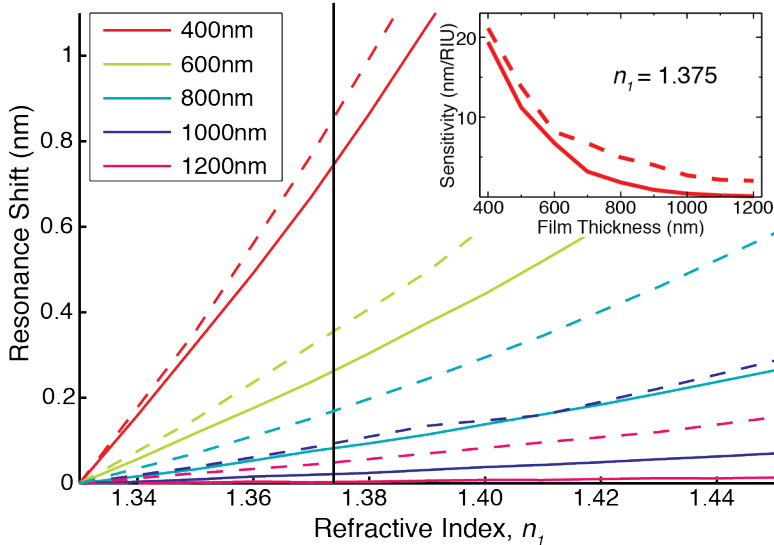
Figure 4.4: FDFD-calculated WGM resonance shifts for Type-I (solid) and Type-II (dashed) FCMs with various film thickness ranging from $400 - 1200$ nm. *Inset* Refractometric sensitivity of Type-I (solid) and Type-II (dashed) capillaries at $n_1 = 1.375$ (solid vertical line in main figure). Film thickness influences the refractometric sensitivity of the device, sharply increasing for "thin" films. For a given film thickness, the larger diameter capillary shows higher refractometric sensitivity.

The FDFD model also showed that the RS of the FCMs depends on the refractive index of the analyte n_1. In both structures the sensitivity increased with increasing n_1, evidenced by the nonlinearity of the curves in Fig. 4.4. For example, in a Type-I FCM with a 400 nm (1000 nm) film, the sensitivity increases from 16 nm/RIU (0.3 nm/RIU) to 27 nm/RIU (0.7 nm/RIU) over the specified refractive index range. This trend, also observed in experiment (discussed in Sec. 4.4), is partly associated with the increased field extension

into the fluid core when $n_1 \rightarrow n_2$.

4.3.2   Finite-difference time-domain simulations

Finite-difference time-domain (FDTD) simulations are a powerful numerical technique useful for monitoring the propagation of electromagnetic radiation in dielectric materials. The structure to be simulated is defined by a grid of cells (Fig. 4.5), each with a corresponding refractive index value. Light propagation is simulated by solving a discretized set of Maxwell's curl equations in each cell in discrete time steps, for example:

$$H_{x(i,j,k)}^{n+1/2} = H_{x(i,j,k)}^{n-1/2} + \frac{\Delta t}{\mu \Delta z}(E_{y(i,j,k)}^{n} - E_{y(i,j,k-1)}^{n}) \tag{4.24}$$

$$- \frac{\Delta t}{\mu \Delta y}(E_{z(i,j,k)}^{n} - E_{z(i,j-1,k)}^{n}) \tag{4.25}$$

$$E_{x(i,j,k)}^{n+1} = E_{x(i,j,k)}^{n} + \frac{\Delta t}{\varepsilon \Delta y}(H_{z(i,j+1,k)}^{n+1/2} - H_{z(i,j,k)}^{n+1/2}) \tag{4.26}$$

$$- \frac{\Delta t}{\varepsilon \Delta z}(H_{y(i,j,k+1)}^{n+1/2} - H_{y(i,j,k)}^{n+1/2}) \tag{4.27}$$

where the indices i, j, and k specify a particular cell at time step n, ε and μ are the material permittivity and permeability, respectively, and the $\Delta x, y, z, t$ terms represent the spacial and temporal grid spacings. Generally, field components are calculated in a "leapfrog" manner, alternating between **E** and **H** fields in half integer time steps (*i.e.* **E**-field components are calculated at $t = n\Delta t$, and **H**-field components are calculated at $t = (n+1/2)\Delta t$). At the computational boundaries a perfectly-matched-layer was used to act as a perfect absorber of all incident radiation. This allowed radiation to escape the computational domain without inducing reflections at the boundary. FDTD simulations performed for this study were done so using *Fullwave* from the RSoft Design Group [110].

Extracting useful information from the FDTD simulations was a multi-step process; the procedure was as follows (Fig. 4.6):

1. Launch a broadband field (*i.e.*, pulse) to excite a superposition of cavity resonance modes.[3]

2. Without further excitation, monitor the field decay for a certain amount of time; longer times result in higher frequency resolution.

---

[3]Both radial and plane wave excitation fields originating from the QD film were used as a radiation source for the simulations; results using the two fields were identical.
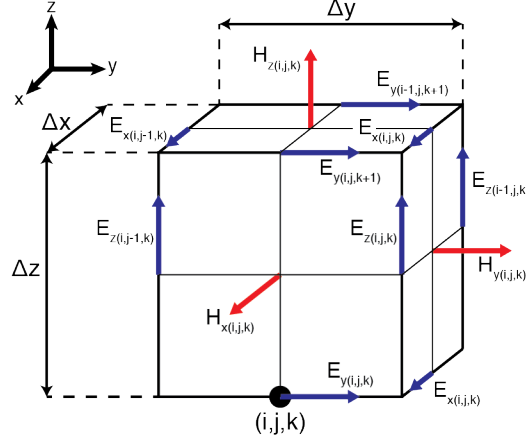
Figure 4.5: Yee cell at grid point (i,j,k) used for calculating the electromagnetic fields in FDTD simulations. Each electric (magnetic) field component is calculated from the four surrounding magnetic (electric) field components.

3. Perform a Fourier transform on the time-domain data to yield a frequency spectrum of the cavity.

4. Extract (a) mode profile or (b) sensitivity data:

   (a) Drive the system at single resonance frequency and use a spatial monitor to obtain the radial mode profile.

   (b) Repeat steps 1-3 for various values of n_1. Monitor the frequency of a single resonance to obtain the refractometric sensitivity. This may also require step 4a to ensure the same azimuthal order mode is monitored.

5. Repeat steps 1-4, applying desired structural changes (*i.e.,* changes to film thickness).

The FDTD simulations revealed a similar dependence of the RS on film thickness and core refractive index as the FDFD simulations: increasing for thinner films and higher core indices (Fig. 4.7a). The calculated resonance shifts were non-linear with respect to n_1. In this refractive index range, the curves were well approximated by a quadratic function. The RS was taken as the slope of the curve, $RS = \frac{\partial \lambda}{\partial n_1}$, yielding an approximately linear increase in sensitivity with the core refractive index. For example, with a film thickness of $500\,\text{nm}$ the RS increased from $8\,\text{nm/RIU}$ to $18\,\text{nm/RIU}$ over the range of n_1, from 1.33 to 1.49. These values are consistent with those calculated using the FDFD model.

The FDTD simulations also provided a clear picture of the trade-off between sensitivity and Q-factor, in regards to the QD film thickness. This allowed for an explanation and
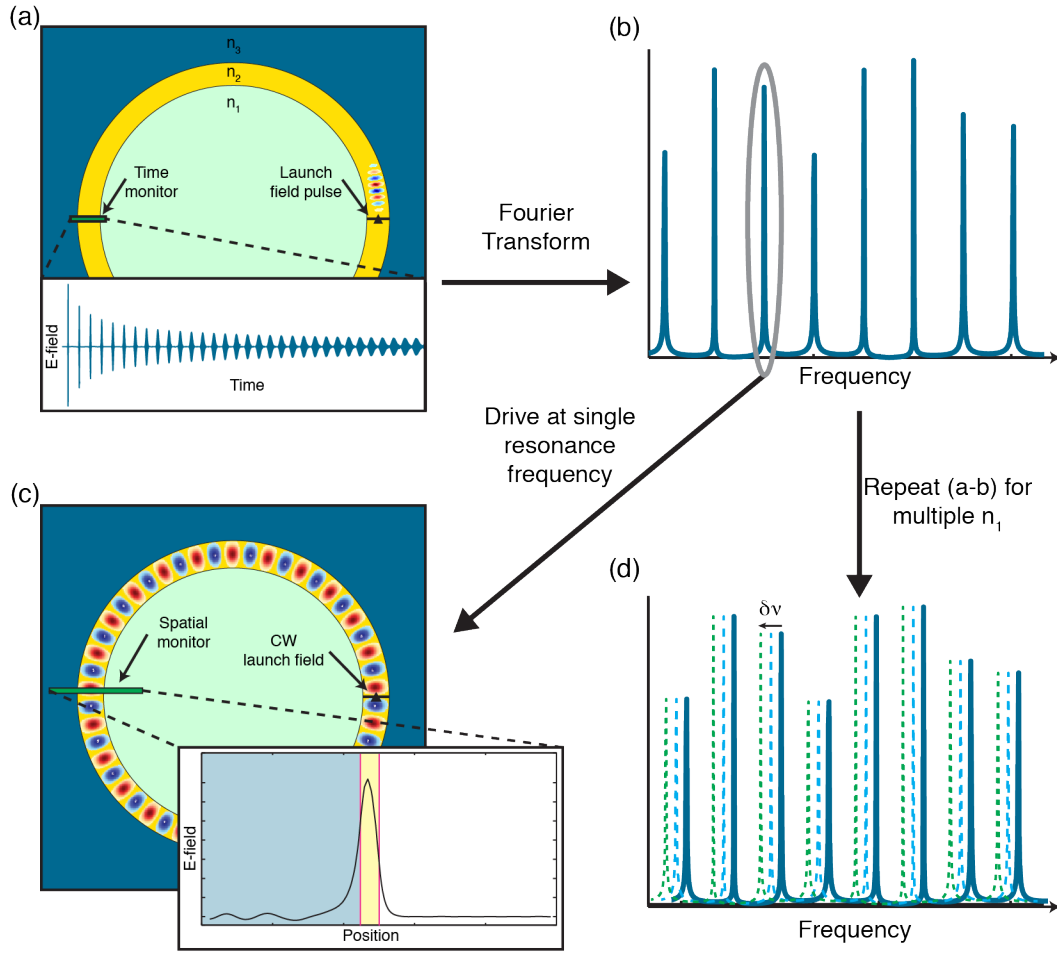
Figure 4.6: Extraction of spectra, refractometric sensitivity, and WGM field information from FDTD simulations (see pg. 68). (a) A pulse is used as an excitation field (*i.e.*, launch field) and the time-dependent electromagnetic field amplitude is monitored at a point in the structure. (b) A Fourier transform of the time response yields a mode spectrum in frequency space. From (b), one can proceed to extract (c) radial mode profiles, or (d) sensitivity information. (c) The system is driven at a single resonance frequency (from the spectrum in (b)) using a continuous wave excitation field. A spatial monitor is used to obtain radial mode profiles. (d) A refractometric sensitivity experiment is simulated by altering the refractive index of the core, repeating steps (a-b), and monitoring the resonance shift of a single mode ($\delta\nu$). In some cases it is necessary to perform step (c) at each refractive index to ensure the same azimuthal mode is being monitored (*i.e.* ensure the mode has the same azimuthal number l).

estimation of the optimal thickness. The maximum sensitivity increased from $0.7\,\mathrm{nm/RIU}$ to $50\,\mathrm{nm/RIU}$ for film thicknesses ranging from $1000\,\mathrm{nm}$ to $300\,\mathrm{nm}$. Over the same range, the Q-factor decreased from 4×10^6 to 2×10^3 (Fig. 4.7b). This degradation in Q imposes an experimental limit to the thickness of the QD film, since a low Q-factor indicates a loss in visibility of WGMs in the PL spectra. This limit was empirically estimated to be around $300\,\mathrm{nm}$, which corresponds to a maximum RS of $\sim 50\,\mathrm{nm/RIU}$. Radial mode profiles confirmed that thinner films result in an increased field presence in the core region of the capillary (Fig. 4.8), offering an explanation to the increased sensitivity of thinner-filmed structures. These results are consistent with those obtained using the FDFD model.
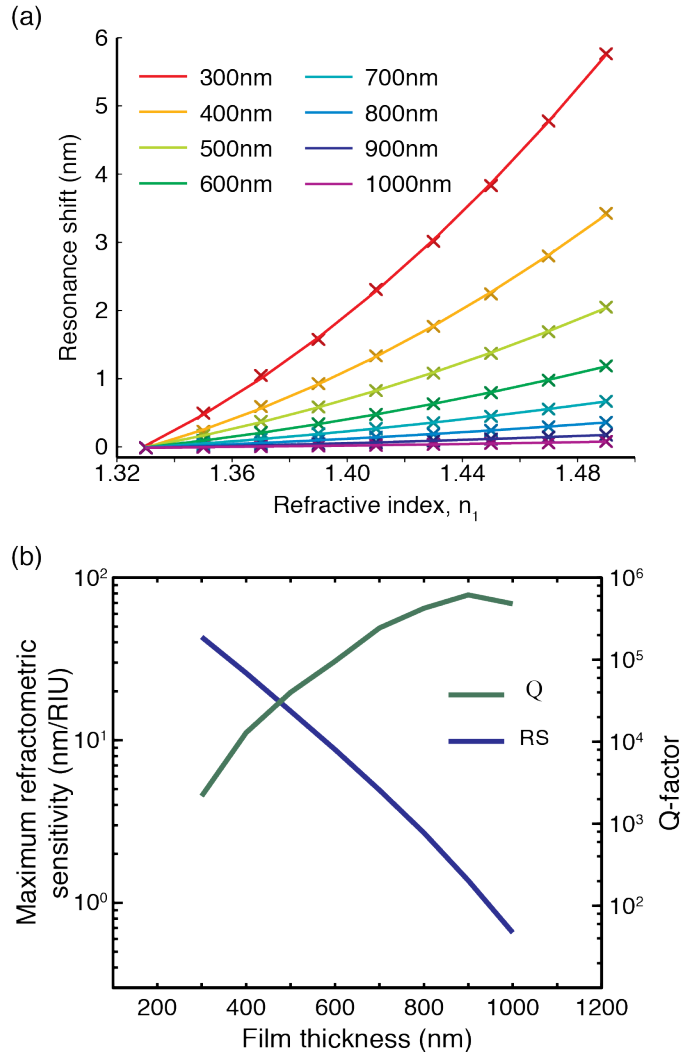
Figure 4.7: FDTD-calculated (a) resonance shift, (b) refractometric sensitivity, and Q-factor of a WGM (TE_z, $\rho = 1$, $l = 161$) in a Type-I FCM with a QD film thickness ranging from $300 - 1000\,\text{nm}$. Curves in (a) are quadratic fits to the calculated resonances (crosses). (b) The refractometric sensitivity (solid blue) was obtained by taking the maximum slope of the curves in (a). The Q-factor (solid green) was taken as the average calculated Q of a mode for a given film thickness.
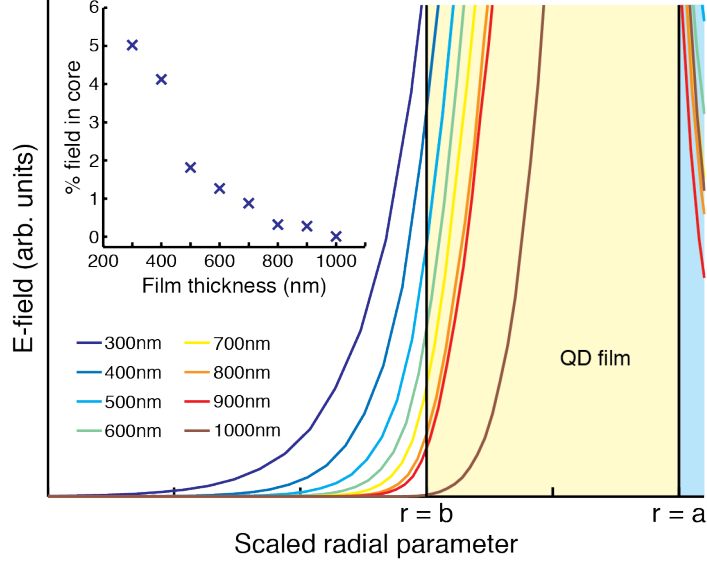
Figure 4.8: Radial field profiles of a WGM (TE_z, $\rho = 1$, $l = 161$) in a Type-I FCM with a QD film thicknesses ranging from $300 - 1000$ nm. The QD film region is highlighted in yellow. The radial parameter is scaled for each curve such that the QD film is represented at the same location. *Inset* Integrated percentage of the WGM field existing in the core region for each film thickness.

4.4 Device performance

4.4.1 Advantages of fluorescent-core microcapillaries

FCMs offer many attractive features over other refractometric sensors, such as LCORRs. The fabrication is simple and does not require thinning processes such as heating, or chemical etching using HF. Furthermore, the sample is structurally robust and easy to handle. Also, no lithographic techniques are required, as needed for the fabrication of "rolled-up" microcapillaries and waveguide-coupled resonators. FCMs do not require nano-positioning devices, evanescent fiber coupling, or costly tunable lasers for operation. Only an excitation source, method of light collection, and spectrometer are required. As demonstrated, the excitation source can be as simple and inexpensive as an LED. While in the present study a microscope was used to collect light from the FCMs, one strictly only needs a lens to focus the capillary image onto the spectroscopy system. Also, the development of on-chip spectrometers, such as tapered waveguide spectrometers, makes LOC integration feasible. These advantages make FCMs an appealing alternative to LCORRs for microfluidic sensing.

4.4.2   Experimental sensitivity and detection limit

An important metric used to measure the capabilities of a refractometric/bio-sensor is the refractometric sensitivity (RS), which dictates the observed shift in WGM wavelength for a given change in refractive index. While over a small range of index, the observed shifts in the WGMs of the Type-I FCM appeared linear, over a larger refractive index range ($n_1 = 1.00 - 1.45$, which includes a point collected with air in the capillary core) the shifts were clearly non-linear, increasing with n_1. The increase in sensitivity with refractive index can be attributed to an increase in the fraction of light energy in the core of the capillary. A simplistic model of this effect has been derived by Zhu *et al.* [111]:

$$RS = \frac{\partial \lambda}{\partial n_1} \approx \frac{\lambda}{n_2} \eta_1 \tag{4.28}$$

where n_2 is the refractive index of the QD film and η_1 is the fraction of light energy in the core. Assuming an exponential decay of the electric field into the core, η_1 can be approximated as

$$\eta_1 \approx A \frac{n_1^2}{\sqrt{n_2^2 - n_1^2}} \tag{4.29}$$

where A is a multiplicative term that depends on the capillary radius, electric field intensity, and mode volume. Equations (4.28) and (4.29) indicate that the RS increases with n_1. The actual functional form of the resonance shifts can be found by integrating Eqs. (4.28) and (4.29), which is non-trivial. For the purposes of this study, a quadratic function, fit to the observed spectral shifts, served as an adequate approximation. The maximum RS of the Type-I FCM, taken as the slope of the curve at $n_1 = 1.453$, was found to be $13.8\,\mathrm{nm/RIU}$ (Fig. 4.9).

A second important metric of refractometric sensors is the detection limit (DL), which is the minimum change in refractive index that can be detected, given by [112, 113]

$$DL = \frac{R_{sensor}}{RS} = \frac{p}{\left(\frac{\partial \lambda}{\partial n}\right)} \tag{4.30}$$

where R_{sensor} is the sensor resolution, taken to be equal to the wavelength pitch of the spectrometer p. The spectrometer pitch is the change in wavelength per pixel on the CCD; it is ultimately determined by the resolution of the grating in the spectrometer. For the spectrometer used in this investigation $p \approx 0.1\,\mathrm{nm/pixel}$. This results in an estimated
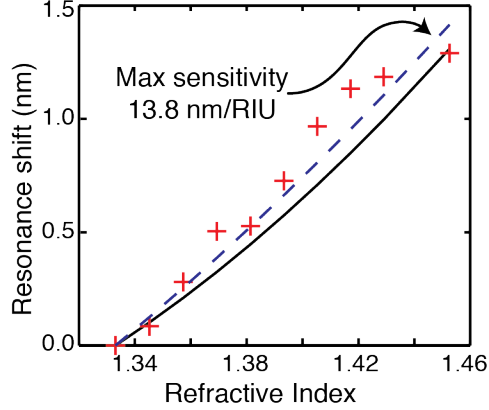
Figure 4.9: Measured (red crosses) and FDFD-calculated (solid line, black) refractometric sensitivity of Type-I FCM. Experimental data is from the $\rho = 1$, $l = 160$ mode in Fig. 3.9 ($\lambda_0 \approx 822$ nm). Also shown is the quadratic fit (long dashed line, blue) to the experimental data, calculated including the $n_1 = 1.0$ point (not shown) with only air in the capillary. The maximum RS was 13.8 nm/RIU. The FDFD-calculated curve was obtained by simulating the $\rho = 1$, $l = 160$ WGM in a Type-I FCM with a 525 nm film.

detection limit of 7×10^{-3} RIU, based on a $RS = 13.8$ nm/RIU. These values are comparable with those of QD-doped fluorescent microspheres [112, 114, 115], but are much lower than those obtained for LCORRs, which have demonstrated sensitivities as high as 390 nm/RIU [60] and detection limits on the order of 10^{-6} RIU [64, 113].[4] Equation (4.30) offers two natural pathways to improve the ultimate detection limit of FCMs: increase the RS and/or improve the sensor resolution.

Several other means to improve the sensitivity may be explored. The first, demonstrated by the FDFD and FDTD simulations discussed in Sec. 4.3, is to decrease the thickness of the QD film. For example, decreasing the film thickness to 300 nm would increase the RS three-fold (see Fig. 4.7). Thinning the QD film may be accomplished by adjusting the concentration of the HSQ precursor solution used in film preparation. Second, large-diameter capillaries increase the fraction of the E-field in the core, thereby increasing the RS. However, as observed in this study, the improvement in RS from the increase in capillary size can be offset by the film thickness. Thus, the film thickness must again be controlled with precision, perhaps by using a blow-through method during fabrication.

In the present study, the DL was ultimately limited by the sensor resolution, which was limited by the relatively poor spectrometer resolution (manufacturer-specified 0.24 nm) and large wavelength pitch (0.10 nm/pixel). In contrast, due to their high Q-factors ($\sim 10^6$)

---

[4]These values correspond to LCORRs using first-order radial modes. LCORRs exploiting higher-order WGMs have demonstrated improved sensitivities and detection limits [65].

and the sub-pm scanning resolution of tunable lasers, LCORRs have DLs on the order of $10^{-6} - 10^{-7}$ [64,65,113]. For FCMs, higher-resolution spectrometers can achieve an order-of-magnitude improvement in the spectral resolution. Further spectrographic improvements are possible: for example, tapered waveguide spectrometers can potentially provide resolutions in the range of a few picometers [69,116]. Additionally, better data analysis methods (as we have recently investigated [117]) could increase the system resolution considerably beyond the spectrometer pitch. These improvements, along with improvements to the RS, could improve the DL of FCMs to $\sim 10^{-5}$ RIU.

Chapter 5

Conclusion

FCMs offer an alternative, microcavity-based refractometric sensing platform that combines the microfluidic advantages of LCORR systems with lower costs and simpler fabrication methods. The refractometric sensing capabilities of FCMs were investigated for potential applications in LOC-based microfluidic sensing.

5.1 Summary of results

A solution-based precursor method was used to fabricate thin QD-embedded films on the inside of glass capillaries. The chemical precursor HSQ was used to coat the capillary channels, which, after an annealing treatment, generated a luminescent film consisting of silicon QDs embedded in an oxide film. Films were fabricated in capillaries with IDs ranging from $25 - 100\,\mu$m by modifying the concentration of the HSQ precursor solution.

In the FCM structures developed here, the QD films supported the formation of WGMs that sampled the capillary channel. The Si-QDs in the film were pumped using either an Ar-ion laser or an LED and their luminescence coupled into the WGMs. The mode structure was studied using standard spectroscopic methods. Refractometric sensing was demonstrated using two different capillary sizes: a $25\,\mu$m ID capillary (Type-I), and a $100\,\mu$m ID capillary (Type-II). Aqueous sucrose solutions of varying concentration were pumped though the capillaries. The sucrose concentration determined the refractive index of the solution in the channel. Varying the index caused a shift in the resonant wavelengths of WGMs propagating in the QD film. A total shift of $1.3\,$nm was observed for the Type-I capillary, and $0.65\,$nm for the Type-II capillary, over refractive index ranges of $1.333 - 1.453$ and $1.333 - 1.423$,

respectively. The refractometric sensitivity (RS) was determined by taking the slope of the data, yielding a maximum sensitivity of $13.8\,\mathrm{nm/RIU}$ and $6.8\,\mathrm{nm/RIU}$ in the Type-I and Type-II capillaries, respectively.

Electromagnetic field simulations were used to predict the performance of various FCM devices. Three parameters were found to control the overall refractometric sensitivity. The thickness of the QD layer had the strongest effect; for example, upon decreasing the film thickness from 1000 to $300\,\mathrm{nm}$, the RS of a Type-I FCM increased from 0.7 to $43\,\mathrm{nm/RIU}$ ($n_1 = 1.45$). Second, the capillary diameter can play an important role, with larger diameters giving a better sensitivity. Thirdly, the solution refractive index itself controls the sensitivity. As the fluid index n_1 approaches the film index, the RS was found to increase. All three effects are related to the fraction of the mode extending evanescently into the capillary channel. These simulations also permitted the experimental QD film thickness to be extracted, since the capillary diameter and sensitivity were known or measured. In this way, the thickness of the QD film in the Type-I and -II capillaries were estimated at $\sim 525\,\mathrm{nm}$ and $\sim 650\,\mathrm{nm}$, respectively.

The ultimate detection limit of the studied FCMs is given by the wavelength resolution of the experimental setup divided by the FCM sensitivity. Given a maximum sensitivity of $13.8\,\mathrm{nm/RIU}$ and a spectrometer pitch of $0.1\,\mathrm{nm/pixel}$, the detection limit is $7 \times 10^{-3}\,\mathrm{RIU}$. This detection limit is comparable to other "traditional" fluorescence systems, such as QD-embedded microspheres, but is much smaller than those characteristic of LCORR-based devices that utilize a tunable laser and an evanescent coupling apparatus. The detection limits of the FCM devices would be improved, firstly, by using a thinner QD film. This could be accomplished by adjusting the concentration of the HSQ precursor solution. Second, increasing the size of the capillary can also increase the sensitivity of the device. Thirdly, using a higher-resolution detection system would correspondingly increase the detection limits. Fourthly, more advanced data analysis methods can not only improve the ultimate experimental resolution, but can significantly decrease the required sampling time. These combined improvements could increase the detection limits by several orders of magnitude.

5.2 Future study

Due to their simplicity, both in fabrication and operation, FCMs offer an interesting method of refractometric sensing in microfluidic environments. With the foundation of their sensing

capabilities firmly established, several opportunities are possible to optimize FCMs for LOC integration. First, a reliable method for the fabrication of consistent and controllable film thicknesses should be established. This will involve systematic studies involving the precursor concentration and annealing conditions. Also, a "blow-through" technique, in which a pressurized gas is used to eject the precursor solution from the capillary prior to annealing, offers a potential route to fabricating more controllable films. Once this is established, the film thickness can be optimized for a given capillary size, delivering the highest possible RS whilst maintaining a sufficiently high Q-factor.

Recent work has demonstrated that FCMs may be sensitive enough to monitor binding events of certain biomolecular systems [117], suggesting the development of a microfluidic fluorescence-based biosensor. Demonstration of true biosensing would require a multi-step process to functionalize channel surface. The biotin-streptavidin system, with its characteristically high binding affinity, may present a good testbed for the first FCM biosensing experiments.

Bibliography

[1] W. B. J. Zimmerman, *Microfluidics: History, Theory and Applications*, vol. 1. Udine, Italy: SpringerWienNewYork, 2006.

[2] S. Haeberle and R. Zengerle, "Microfluidic platforms for lab-on-a-chip applications," *Lab on a Chip*, vol. 7, pp. 1094–1110, 2007.

[3] H. P. Le, "Progress and trends in ink-jet printing technology," *The Journal of Imaging Science and Technology*, vol. 42, no. 1, pp. 49–62, 1998.

[4] K. E. Herold and A. Rasooly, eds., *Lab on a Chip Technology, Volume 1: Fabrication and Microfluidics*. Norfolk, UK: Caister Academic Press, 1st ed., 2009.

[5] K. E. Herold and A. Rasooly, eds., *Lab on a Chip Technology, Volume 2: Biomolecular Separation and Analysis*. Norfolk, UK: Caister Academic Press, 1st ed., 2009.

[6] S. C. Terry, J. H. Jerman, and J. B. Angell, "A gas chromatographic air analyzer fabricated on a silicon wafer," *Electron Devices*, vol. 26, no. 12, pp. 1880–1886, 1979.

[7] F. Balagaddé, L. You, C. Hansen, F. H. Arnold, and S. R. Quake, "Long-term monitoring of bacteria undergoing programmed population control in a microchemostat," *Science*, vol. 309, pp. 137–140, 2005.

[8] A. H. Diercks, A. Ozinsky, C. L. Hansen, J. M. Spotts, D. J. Rodriquez, and A. Aderem, "A microfluidic device for multiplexed protein detection in nano-liter volumes," *Analytical Biochemistry*, vol. 386, pp. 30–35, 2009.

[9] G. M. Whitesides, "The origins and the future of microfluidics," *Nature*, vol. 442, pp. 368–373, 2006.

[10] P. S. Dittrich, "Lab-on-a-chip: microfluidics in drug discovery," *Nature Reviews Drug Discovery*, vol. 5, pp. 210–218, 2006.

[11] H. Zhu, I. M. White, J. D. Suter, M. Zourob, and X. Fan, "Integrated refractive index optical ring resonator detector for capillary electrophoresis," *Anal. Chem*, vol. 79, pp. 930–937, 2007.

[12] G. E. Moore, "Cramming more components onto integrated circuits," *Electronics*, vol. 38, no. 8, p. 144, 1965.

[13] E. Verpoorte and N. D. Rooij, "Microfluidics meets mems," *Proceedings of the IEEE*, vol. 91, no. 6, pp. 930–953, 2003.

[14] A. Manz, N. Graber, and H. M. Widmer, "Miniaturized total chemical analysis systems: a novel concept for chemical sensing," *Sensors and Actuators B: Chemical*, vol. B1, pp. 244–248, 1990.

[15] A. Rasooly, "Moving biosensors to point-of-care cancer diagnostics.," *Biosensors & bioelectronics*, vol. 21, no. 10, p. 1847, 2006.

[16] A. Rasooly and J. Jacobson, "Development of biosensors for cancer clinical testing," *Biosensors and Bioelectronics*, vol. 21, pp. 1851–1858, Jan 2006.

[17] Some examples include FluimedX (www.fluimedix.com), Biacore (www.biacore.com), and Farfield Sensors (www.farfield-group.com).

[18] B. Cosmi, G. Palareti, M. Moia, and M. Carpenedo, "Accuracy of a portable prothrombin time monitor (coagucheck) in patients on chronic oral anticoagulant therapy: A prospective multicenter study," *Thrombosis Research*, vol. 100, pp. 279–286, 2000.

[19] M. Brivio, N. R. Tas, M. Goedbloed, H. J. G. E. Gardeniers, W. Verboom, A. vandenBerg, and D. N. Reinhoudt, "A maldi-chip integrated system with a monitoring window," *Lab Chip*, vol. 5, no. 378-381, 2005.

[20] B. Kuswandi, Nuriman, J. Huskens, and W. Verboom, "Optical sensing systems for microfluidic devices: a review," *Analytica Chimica Acta*, vol. 601, pp. 141–155, 2007.

[21] E. Krioukov, J. Greve, and C. Otto, "Performance of integrated optical microcavities for refractive index and fluorescence sensing," *Sensors and Actuators B: Chemical*, vol. 90, pp. 58–67, 2003.

[22] P. S. Nunes, N. A. Mortensen, J. P. Kutter, and K. B. Mogensen, "Photonic crystal resonator integrated in a microfluidic system," *Optics letters*, vol. 33, no. 14, pp. 1623–1625, 2008.

[23] A. Ymeti, J. Greve, P. V. Lambeck, T. Wink, S. W. F. M. vanHovell, T. A. M. Beumer, R. R. Wijn, R. G. Heideman, V. Subramaniam, and J. S. Kanger, "Fast, ultrasensitive virus detection using a young interferometer sensor," *Nano Lett*, vol. 7, no. 2, pp. 394–397, 2007.

[24] D. Yin, E. J. Lunt, M. I. Rudenko, D. W. Deamer, A. R. Hawkins, and H. Schmidt, "Planar optofluidic chip for single particle detection, manipulation, and analysis," *Lab on a Chip*, vol. 7, pp. 1171–1175, 2007.

[25] N. A. Abu-Hatab, J. F. John, J. M. Oran, and M. J. Sepaniak, "Multiplexed microfluidic surface-enhanced raman spectroscopy," *Applied spectroscopy*, vol. 61, no. 10, pp. 1116–1122, 2007.

[26] H. Dirac and P. Gravesen, "Realisation and characterisation of all liquid optical waveguides," *IEEE Proceedings 14th International Conference on Micro Electro Mechanical System*, p. 4590462, 2001.

[27] B. H. Weigl and P. Yager, "Silicon-microfabricated diffusion-based optical chemical sensor," *Sensors and Actuators B: Chemical*, vol. 39, pp. 452–457, 1997.

[28] J. Gao, X. Yin, and Z. Fang, "Integration of single cell injection, cell lysis, separation and detection of intracellular constituents on a microfluidic chip," *Lab Chip*, vol. 4, no. 1, pp. 47–52, 2004.

[29] B. Liu, H. Hisamoto, and S. Terabe, "Subsecond separation of cellular flavin coenzymes by microchip capillary electrophoresis with laser-induced fluorescence detection," *Journal of Chromatography A*, vol. 1021, pp. 201–207, 2003.

[30] K. Sapsford, D. Farrell, S. Sun, A. Rasooly, H. Mattoussi, and I. L. Medintz, "Monitoring of enzymatic proteolysis on a electroluminescent-ccd microchip platform using quantum dot-peptide substrates," *Sensors and Actuators B*, vol. 139, pp. 13–21, 2009.

[31] F. Darain, P. Yager, K. L. Gan, and S. C. Tjin, "On-chip detection of myoglobin based on fluorescence," *Biosensors and Bioelectronics*, vol. 24, pp. 1744–1750, 2009.

[32] A. Boardman, K. Booth, and P. Egan, "Optical guided waves, linear and nonlinear surface plasmons," *Guided Wave Nonlinear Optics*, pp. 201–230, 1992.

[33] A. D. Boardman, *Electromagnetic surface modes*. Chichester: Wiley, 1982.

[34] J. Homola, "Present and future of surface plasmon resonance biosensors," *Analytical and bioanalytical chemistry*, vol. 377, pp. 528–539, 2003.

[35] R. B. M. Schasfoort and A. J. Tudos, eds., *Handbook of Surface Plasmon Resonance*. The Royal Society of Chemistry, 2008.

[36] D. Kohlheyer and R. B. M. Schasfoort *Eur. Pat. Appl.*, no. EP 05076569.2, 2005.

[37] N. B. Colthup, L. H. Daly, and S. E. Wiberley, *Introduction to infrared and Raman spectroscopy*. Academic Press, Inc., 3 ed., 1990.

[38] I. White, J. Gohring, and X. Fan, "Sers-based detection in an optofluidic ring resonator platform," *Optics Express*, vol. 15, no. 25, pp. 17433–17442, 2007.

[39] Y. S. Huh, A. J. Chung, and D. Erickson, "Surface enhanced raman spectroscopy and its application to molecular and cellular analysis," *Microfluidics and Nanofluidics*, vol. 6, pp. 285–297, 2009.

[40] S. Nie and S. Emory, "Probing single molecules and single nanoparticles by surface-enhanced raman scattering," *Science*, vol. 275, pp. 1102–1106, 1997.

[41] F. Docherty, P. Monaghan, R. Keir, D. Graham, W. E. Smith, and J. M. Cooper, "The first serrs multiplexing from labelled oligonucleotides in a microfluidics lab-on-a-chip," *Chem. Commun.*, vol. 1, pp. 118–119, 2004.

[42] L. Chen and J. Choo, "Recent advances in surface enhanced raman scattering detection technology for microfluidic chips," *Electrophoresis*, vol. 29, pp. 1815–1828, 2008.

[43] L. Rayleigh *Phil. Mag.*, vol. 20, p. 1001, 1910.

[44] M. L. Gorodetsky, "High-q optical whispering-gallery microresonators: precession approach for spherical mode analysis and emission patterns with prism couplers," *Optics Communications*, vol. 113, pp. 133–143, 1994.

[45] M. Born and E. Wolf, *Principles of Optics*. Cambridge, UK: Cambridge University Press, 7th ed., 2005.

[46] D. J. Griffiths, *Introduction to Electrodynamics*. Upper Saddle River, New Jersey: Prentice Hall, 3rd ed., September 1999.

[47] B. E. A. Saleh and M. C. Teich, *Fundamentals of Photonics*. Hoboken, New Jersey: Wiley-Interscience, 2nd ed., 2007.

[48] E. Hecht, *Optics*. US: Addison Wesley, 4th ed., 2002.

[49] J. A. Stratton, *Electromagnetic Theory*. Hoboken, New Jersey: John Wiley & Sons, Inc., 2007.

[50] D. Marcuse, *Light Transmission Optics*. New York, N.Y.: Van Nostrand Reinhold Company Inc., 2nd ed., 1982.

[51] A. W. Snyder and J. D. Love, *Optical Waveguide Theory*. New York, US: Chapman and Hall, 1983.

[52] A. Oraevsky, "Whispering-gallery waves," *Quantum Electronics*, 2002.

[53] C. P. K. Manchee, V. Zamora, J. Silverstone, J. G. C. Veinot, and A. Meldrum, "Refractometric sensing in fluorescent-core microcapillaries." Submitted to Optics Express, June 2011.

[54] A. Yalcin, K. Popat, J. C. Aldridge, T. A. Desai, M. S. Unlu, and B. B. Goldberg, "Optical sensing of biomolecules using microring resonators," *IEEE Journal of Selected Topics in Quantum Electronics*, vol. 12, no. 1, pp. 148–155, 2006.

[55] A. M. Armani, R. P. Kulkarni, S. E. Fraser, R. C. Flagan, and K. J. Vahala, "Label-free, single-molecule detection with optical microcavities," *Science*, vol. 317, no. 5839, p. 783, 2007.

[56] S. Arnold, S. I. Shopova, and S. Holler, "Whispering gallery mode bio-sensor for label-free detection of single molecules: thermo-optic vs. reactive mechanism," *Optics Express*, vol. 18, no. 1, pp. 281–287, 2010.

[57] P. Bianucci, J. R. Rodríguez, C. M. Clements, J. G. C. Veinot, and A. Meldrum, "Silicon nanocrystal luminescence coupled to whispering gallery modes in optical fibers," *J. Appl. Phys.*, vol. 105, p. 023108, 2009.

[58] F. Vollmer, S. Arnold, D. Braun, I. Teraoka, and A. Libchaber, "Multiplexed dna quantification by spectroscopic shift of two microsphere cavities," *Biophysical Journal*, vol. 85, pp. 1974–1979, 2003.

[59] I. M. White, H. Zhu, J. D. Suter, X. Fan, and M. Zourob, "Label-free detection with the liquid core optical ring resonator sensing platform," *Methods in molecular biology (Clifton, NJ)*, vol. 503, p. 139, 2009.

[60] V. Zamora, A. Díez, M. Andrés, and B. Gimeno, "Refractometric sensor based on whispering-gallery modes of thin capillaries," *Optics Express*, vol. 15, no. 19, pp. 12011–12016, 2007.

[61] G. Huang, V. A. Bolaños, F. Ding, and V. A. B. Quiñones, "Rolled-up optical microcavities with subwavelength wall thicknesses for enhanced liquid sensing applications," *ACS nano*, vol. 4, no. 6, pp. 3123–3130, 2010.

[62] F. Vollmer and S. Arnold, "Whispering-gallery-mode biosensing: label-free detection down to single molecules," *Nature Methods*, vol. 5, no. 7, pp. 591–596, 2008.

[63] I. White, H. Oveys, and X. Fan, "Liquid-core optical ring-resonator sensors," *Optics letters*, vol. 31, no. 9, pp. 1319–1321, 2006.

[64] I. White, H. Zhu, J. D. Suter, N. M. Hanumegowda, H. Oveys, M. Zourob, and X. Fan, "Refractometric sensors for lab-on-a-chip based on optical ring resonators," *IEEE Sensors Journal*, vol. 7, no. 1, pp. 28–35, 2007.

[65] H. Li and X. Fan, "Characterization of sensing capability of optofluidic ring resonator biosensors," *Applied Physics Letters*, vol. 97, p. 011105, 2010.

[66] G. Yang, I. White, and X. Fan, "An opto-fluidic ring resonator biosensor for the detection of organophosphorus pesticides," *Sensors and Actuators B: Chemical*, 2008.

[67] I. White, J. Suter, M. Zourob, and X. Fan, "Opto-fluidic micro-ring resonator for sensitive label-free viral detection," *Analyst*, vol. 133, pp. 356–360, 2008.

[68] A. Beltaos and A. Meldrum, "Whispering gallery modes in silicon-nanocrystal-coated silica microspheres," *Journal of Luminescence*, vol. 126, pp. 607–613, 2007.

[69] R. G. DeCorby, N. Ponnampalam, E. Epp, T. Allen, and J. N. McMullin, "Chip-scale spectrometry based on tapered hollow bragg waveguides," *Optics Express*, vol. 17, no. 19, pp. 16632–16645, 2009.

[70] E. Epp, N. Ponnampalam, J. McMullin, and R. DeCorby, "Thermal tuning of hollow waveguides fabricated by controlled thin-film buckling," *Optics Express*, vol. 17, no. 20, pp. 17369–17375, 2009.

[71] G. Huang, S. Kiravittaya, V. A. B. Quiñones, F. Ding, M. Beyoucef, A. Rastelli, Y. Mei, and O. Schmidt, "Optical properties of rolled-up tubular microcavities from shaped nanomembranes," *Applied Physics Letters*, vol. 94, p. 141901, 2009.

[72] Z. Lu, D. J. Lockwood, and J. M. Baribeau, "Quantum confinement and light emission in sio2/si superlattices," *Nature*, vol. 378, pp. 258–260, 1995.

[73] A. Nassiopoulos, S. Grigoropoulos, and D. Papadimitriou, "Electroluminescent device based on silicon nanopillars," *Applied Physics Letters*, vol. 69, no. 15, pp. 2267–2269, 1996.

[74] L. Canham, "Silicon quantum wire array fabrication by electrochemical and chemical dissolution of wafers," *Applied physics letters*, vol. 57, no. 10, pp. 1046–1048, 1990.

[75] C. M. Hessel, E. J. Henderson, and J. G. C. Veinot, "Hydrogen silsesquioxane: A molecular precursor for nanocrystalline si/sio2 composites and freestanding hydride-surface-terminated silicon nanoparticles," *Chem. Mater*, vol. 18, pp. 6139–6146, 2006.

[76] A. Alivisatos, "Perspectives on the physical chemistry of semiconductor nanocrystals," *The Journal of Physical Chemistry*, vol. 100, pp. 13226–13239, 1996.

[77] S. V. Gaponenko, *Optical Properties of Semiconductor Nanocrystals*. New York, US: Cambridge University Press, 1998.

[78] L. Pavesi, "Silicon-based light sources for silicon integrated circuits," *Advances in Optical Technologies*, vol. 2008, no. 416926, pp. 1–13, 2008.

[79] R. J. Walters, J. Kalkman, A. Polman, H. A. Atwater, and M. J. A. deDood, "Photo-luminescence quantum efficiency of dense silicon nanocrystal ensembles in sio2," *Phys. Rev. B*, vol. 73, no. 132302, 2006.

[80] Y. Wang, G. Kong, W. Chen, H. W. Diao, C. Y. Chen, S. B. Zhang, and X. B. Liao, "Getting high-efficiency photoluminescence from si nanocrystals in sio matrix," *Applied Physics Letters*, vol. 81, no. 22, pp. 4174–4176, 2002.

[81] W. Wilson, P. Szajowski, and L. Brus, "Quantum confinement in size-selected, surface-oxidized silicon nanocrystals," *Science*, vol. 262, pp. 1242–1244, 1993.

[82] L. E. Brus, P. F. Szajowski, W. L. Wilson, T. D. Harris, S. Schuppler, and P. H. Citrin, "Electronic spectroscopy and photophysics of si nanocrystals: relationship to bulk c-si and porous si," *Journal of the American Chemical Society*, vol. 117, pp. 2915–2922, 1995.

[83] A. Kholod, V. Borisenko, A. Saúl, F. A. d'Avitaya, and J. Fuhr, "Appearance of direct gap in silicon and germanium nanosize slabs," *Optical Materials*, vol. 17, pp. 61–63, 2001.

[84] D. J. Lockwood and L. Pavesi, "Silicon fundamentals for photonics applications," *Silicon Photonics, Topics in Applied Physics*, vol. 94, pp. 1–52, 2004.

[85] M. G. Albrecht and C. Blanchette, "Materials issues with thin film hydrogen silsesquioxane low k dielectrics," *Journal of the Electrochemical Society*, vol. 145, no. 11, pp. 4019–4025, 1998.

[86] C. M. Hessel, E. J. Henderson, and J. G. C. Veinot, "An investigation of the formation and growth of oxide-embedded silicon nanocrystals in hydrogen silsesquioxane-derived nanocomposites," *J. Phys. Chem C*, vol. 111, pp. 6956–6961, 2007.

[87] J. A. Kelly, E. J. Henderson, and J. G. C. Veinot, "Sol–gel precursors for group 14 nanocrystals," *Chem. Commun.*, vol. 46, pp. 8704–8718, 2010.

[88] E. Henderson, J. A. Kelly, and J. G. C. Veinot, "Influence of hsio1.5 sol-gel polymer structure and composition on the size and luminescent properties of silicon nanocrystals," *Chemistry of Materials*, vol. 21, pp. 5426–5434, 2009.

[89] C. M. Hessel, M. A. Summers, A. Meldrum, M. Malac, and J. G. C. Veinot, "Direct patterning, conformal coating, and erbium doping of luminescent nc-si/sio2 thin films from solution processable hydrogen silsesquioxane," *Adv. Mater.*, vol. 19, no. 21, p. 3513, 2007.

[90] J. R. Rodríguez, F. C. Lenz, J. G. C. Veinot, and A. Meldrum, "Mode structure in the luminescence of si-nc in cylindrical microcavities," *Physica E*, vol. 41, pp. 1107–1110, 2009.

[91] J. R. Rodríguez, J. G. C. Veinot, P. Bianucci, and A. Meldrum, "Whispering gallery modes in hollow cylindrical microcavities containing silicon nanocrystals," *Applied physics letters*, vol. 92, p. 131119, 2008.

[92] Polymicro Technologies. http://www.polymicro.com.

[93] Dow Corning Inc., Trade name Fox15.

[94] Sigma Aldrich. Product number: S9378-500G, http://www.sigmaaldrich.com.

[95] Z. Karny and O. Kafri, "Refractive-index measurements by moire deflectometry," *Applied optics*, vol. 21, no. 18, pp. 3326–3328, 1982.

[96] W. Yunus and A. Rahman, "Refractive index of solutions at high concentrations," *Applied optics*, vol. 27, no. 16, pp. 3341–3343, 1988.

[97] D. Charles, "Refractive indices of sucrose-water solutions in the range from 24 to 53pp. 405–406, 1965.

[98] Thermo Fisher Scientific. Density, refractive index and concentration data for sucrose at 20°C, molecular weight = 342.3, http://www.piramoon.com/sucrose.php.

[99] R. C. Weast and M. J. Astle, eds., *CRC Handbook of Chemistry and Physics*. Boca Raton, Florida: CRC Press, Inc., 63rd ed., 1982.

[100] International Chemical Safety Card 1507, Geneva: International Programme on Chemical Safety, November 2003, http://www.inchem.org.

[101] PE tubing 0.015" ID, Fisher Scientific, Product number: 3032515P01, https://www.fishersci.ca.

[102] T. Carmon, L. Yang, and K. Vahala, "Dynamical thermal behavior and thermal self-stability of microcavities," *Optics Express*, vol. 12, no. 20, pp. 4743–4750, 2004.

[103] J. D. Suter, I. M. White, H. Zhu, and X. Fan, "Thermal characterization of liquid core optical ring resonator sensors," *Applied optics*, vol. 46, no. 3, pp. 389–396, 2007.

[104] S. M. A. Durrani, M. F. Al-Kuhaili, and E. E. Khawaja, "Characterization of thin films of a-siox (1.1< x< 2.0) prepared by reactive evaporation of sio," *Journal of Physics: Condensed Matter*, vol. 15, pp. 8123–8135, 2003.

[105] D. Amans, S. Callard, A. Gagnaire, J. Joseph, G. Ledoux, and F. Huisken, "Ellipsometric study of silicon nanocrystal optical constants," *J. Appl. Phys.*, vol. 93, no. 7, p. 4173, 2003.

[106] A. W. Poon and R. K. Chang, "Spiral morphology-dependent resonances in an optical fiber: effects of fiber tilt and focused gaussian beam illumination," *Optics letters*, vol. 23, no. 14, pp. 1105–1107, 1998.

[107] A. L. Stancik and E. B. Brauns, "A simple asymmetric lineshape for fitting infrared absorption spectra," *Vibrational Spectroscopy*, vol. 47, no. 1, pp. 66–69, 2008.

[108] M. K. El-Adawi, M. A. Abdel-Naby, and S. A. Shalaby, "Laser heating of a two-layer system with constant surface absorption: an exact solution," *International Journal of Heat Mass Transfer*, vol. 38, no. 5, pp. 947–952, 1995.

[109] Z. H. Shen, S. Y. Zhang, J. Lu, and X. W. Ni, "Mathematical modeling of laser induced heating and melting in solids," *Optics & laser technology*, vol. 33, pp. 533–537, 2001.

[110] RSoft Design Group Inc., *Fullwave v6.1*, 2008.

[111] H. Zhu, I. M. White, J. D. Suter, P. S. Dale, and X. Fan, "Analysis of biomolecule detection with optofluidic ring resonator sensors," *Optics Express*, vol. 15, no. 15, pp. 9139–9146, 2007.

[112] S. Pang, R. Beckham, and K. Meissner, "Quantum dot-embedded microspheres for remote refractive index sensing," *Applied Physics Letters*, vol. 92, p. 221108, 2008.

[113] I. M. White and X. Fan, "On the performance quantification of resonant refractive index sensors," *Optics Express*, vol. 16, no. 2, pp. 1020–1028, 2008.

[114] D. E. Gomez, I. Pastoriza-Santos, and P. Mulvaney, "Tunable whispering gallery mode emission from quantum-dot-doped microspheres," *Small*, vol. 1, no. 2, pp. 238–241, 2005.

[115] A. Weller, F. C. Liu, R. Dahint, and M. Himmelhaus, "Whispering gallery mode biosensors in the low-q limit," *Applied Physics B: Lasers and Optics*, vol. 90, pp. 561–567, 2008.

[116] O. Schmidt, P. Kiesel, S. Mohta, and N. M. Johnson, "Resolving pm wavelength shifts in optical sensing," *Applied Physics B: Lasers and Optics*, vol. 86, pp. 593–600, 2007.

[117] J. W. Silverstone, S. McFarlane, C. P. K. Manchee, and A. Meldrum, "Ultimate resolution for refractometric sensing with optical microcavities." Submitted to Optics Express, August 2011.

[118] F. K. Lutgens and E. J. Tarbuck, *Essentials of Geology*. Prentice Hall, 7th ed., 2000.

[119] J. Popplewell, S. King, J. Day, P. Ackrill, L. K. Fifield, R. G. Cresswell, M. diTada, and K. Lui, "Kinetics of uptake and elimination of silicic acid by a human subject: a novel application of 32si and accelerator mass spectrometry," *Journal of Inorganic Biochemistry*, vol. 69, pp. 177–180, 1998.

[120] State of California-Department of Toxic Substances Control, "Cadmium in Children's Jewlery," http://www.dtsc.ca.gov/PollutionPrevention/ToxicsInProducts/Cadmium.cfm.

[121] N. W. Ashcroft and N. D. Mermin, *Solid State Physics*. US: Brooks/Cole, 1976.

[122] S. Coffa and L. Tsybeskov, "Silicon-based optoelectronics," *MRS Bulletin*, vol. 23, no. 4, pp. 16–17, 1998.

[123] L. Brus, "Nanocrystal spectroscopy and photophysics: direct gap cdse and indirect gap silicon," *Proceedings of SPIE*, vol. 2125, pp. 381–385, 1994.

[124] L. Brus, "Luminescence of silicon materials: chains, sheets, nanocrystals, nanowires, microcrystals, and porous silicon," *The Journal of Physical Chemistry*, vol. 98, pp. 3575–3581, 1994.

[125] M. Fox, *Quantum Optics: An Introduction*. Oxford, GBR: Oxford University Press, 2006.

[126] A. Meldrum, P. Bianucci, and F. Marsiglio, "Modification of ensemble emission rates and luminescence spectra for inhomogeneously broadened distributions of quantum dots coupled to optical microcavities," *Optics Express*, vol. 18, no. 10, pp. 10230–10246, 2010.

Appendix A

Peak fitting

The WGM resonant wavelengths were obtained by peak fitting. The peaks were fit in frequency-space and the results were translated back to wavelength for visualization. Spectra were translated to frequency using the equations

$$\nu = \frac{c}{\lambda} \tag{A.1}$$

$$S(\nu) = S(\lambda)\frac{c}{\nu^2} \tag{A.2}$$

Peak fitting was performed after calibration and blackbody correction.

The fitting required the isolation of each peak. First, the background was subtracted from the spectrum. Using an approximate FSR as a guide, the maxima and minima in the spectrum were found in a leap-frog manner. The background was obtained by fitting the minima to a Gaussian curve. This background was then subtracted from the spectrum. Peaks were extracted by "chopping" the spectrum at each minimum.

Table A.1: Peak fitting lineshapes and parameters

Lineshape	FCM	$I(\nu)$		Free parameters
Lorentzian	Type-II	$\frac{A}{1+(\frac{\nu-\nu_0}{\gamma})^2} + C$	4	A, ν_0, γ, C
skewed Lorentzian	Type-I	$\frac{A}{1+(\frac{\nu-\nu_0}{\gamma(\nu)})^2} + C$ $\gamma(\nu) = \frac{(1+b_2)\gamma_0}{1+b_2 e^{-b_1(\nu-\nu_0)}}$	6	A, ν_0, γ_0, b_1, b_2, C
two Lorentzians	Type-I	$\frac{A_1}{1+(\frac{\nu-\nu_1}{\gamma_1})^2} + \frac{A_2}{1+(\frac{\nu-\nu_2}{\gamma_2})^2} + C$	7	A_1, ν_1, γ_1, A_2, ν_2, γ_2, C

Peaks were fit to the desired lineshape (Table A.1) using a non-linear least squares

method, where the residuals were minimized through iterative adjustment of the fitting parameters. Starting values for the peak frequency and linewidth were approximated from the extracted minima and maxima (described above). Each peak was individually normalized and shifted such that $A \approx 1$ and $C \approx 0$. In the case of the two Lorentzians, the starting values for the amplitude, frequency, and width of the side band (peak "2") were estimated by $A_2 = \frac{1}{2}A_1$, $\nu_2 = \nu_1 + \frac{1}{2}\gamma_1$, and $\gamma_2 = \gamma_1$, respectively. These starting values were found to allow faster convergence of the fit. Errors in the peak fitting parameter were calculated from the fit residuals.

As a test, each peak was fit to the sum of multiple lines to account for the overlap from neighbouring modes. The results were consistent with those obtained when fitting each peak in isolation.

Appendix B

Optical properties of silicon

The relative low cost and abundance of silicon,[1] combined with it's unique semiconducting properties, resulted in it being the semiconductor of choice during the electronic/technological boom of the past half-century. Today, silicon is the backbone of nearly every piece of technology as it is the primary component in all integrated circuits. Recently, however, a significant research effort has been dedicated towards the integration of silicon-based optical components into integrated circuits in an attempt to overcome the speed, power, and space limitations of current electronic microchips. For biomolecular/optofluidic applications, a silicon-based light source would be preferred over other semiconductors for its low toxicity and high biocompatibility [119]. Other semiconductors pose significant health risks due to their heavy metal constituents, such as Cd and As, which are restricted in commercial good by many global regions, including Europe and California [120]. Unfortunately, silicon is a poor light emitter, exhibiting quantum efficiencies orders of magnitudes lower than of semi-conductors like GaAs and CdSe. The poor optical properties of silicon are a result of its electronic structure, as silicon is an indirect bandgap semiconductor [78].

The electronic properties of a bulk solid are heavily governed by its lattice structure. The periodic nature of the lattice generates a periodic potential that modifies the wavefunction[2] of electrons in the solid. This modification is described by **Bloch's theorem**, which states that the wavefunction ψ of an electron in the solid should have the same periodicity as the potential:

---

[1] Silicon is the second most abundant element in the earth's crust at 27.7% by mass, first is oxygen [118]

[2] the wavefunction of an electron is an eigenstate ψ of the one-electron Hamiltonian $H = -\hbar^2\nabla^2/2m + U(\mathbf{r})$, where, given a lattice periodicity of $\mathbf{R}$, $U(\mathbf{r}) = U(\mathbf{r} + \mathbf{R})$ [121].

$$\psi(\mathbf{r} + \mathbf{R}) = e^{i\mathbf{k}\cdot\mathbf{R}}\psi(\mathbf{r}) \tag{B.1}$$

where $\mathbf{R}$ is a lattice vector (representative of the periodicity of the lattice. Each Hamiltonian eigenstate wavefunction has a corresponding wavevector $\mathbf{k}$ and energy E (*i.e.*, the eigenvalue of the Hamiltonian). Bloch's theorem results in the separation of allowed energy states into bands. An important factor in determining the electronic properties of a solid is the Fermi energy, which dictates the energy up to which electrons occupy. This, in combination with the shape of the bands, determines whether a solid is a conductor, insulator, or semi-conductor. In this case of insulators and semi-conductors, the lower-energy (valence) band is completely filled, while the higher-energy (conduction) band is completely empty (Fig. B.1a). The energy difference between bands of a material is not constant for all values of $\mathbf{k}$[3]; it is the minimum energy difference which is most often referred to as the bandgap of the material. If the energy maximum of the valence band and minimum of the conduction band are aligned in $\mathbf{k}$-space, then the transition is direct, requiring only a change in the electron's energy. If the valence and conduction bands are not aligned in $\mathbf{k}$-space then transition is indirect, requiring a change in both energy and wave vector $\mathbf{k}$ (momentum). Photons carry a negligible amount of momentum, so, while they contribute the majority of the energy requirements for the electronic transition, the change in momentum required for indirect transitions must be supplied from another source. Most often the momentum is supplied by lattice vibrations, known as phonons. Figure B.1b compares the band structure of indirect and direct bandgap semiconductors (Si and GaAs, respectively). In silicon, most optical transitions must be phonon assisted, resulting in long radiative lifetimes ($\sim \mu s - ms$), small absorption cross-sections, and poor quantum efficiencies compared to direct bandgap semiconductors [76, 82, 122].

When an electron is promoted into the conduction band of a semiconductor, its absence in the valance band can behave with some particle-like properties. This "particle" is termed a hole. In fact, the generated electron-hole ($e-h$, or $e^- - h^+$) pair can interact through the electrostatic Coulomb force and form a bound state. This bound state is called an exciton. The decay of an exciton, *i.e.* recombination of the $e - h$ pair, results in the emission of radiation. Since electrons and holes have charges of $-e$ and $+e$, respectively, excitons can be treated mathematically in much the same way as the hydrogen atom, except with a modified

---

[3]The wave vector $\mathbf{k}$ is intrinsically related to both the momentum of the electron and the reciprocal lattice, and so $\mathbf{k}$-space is sometimes referred to as momentum space or reciprocal space.
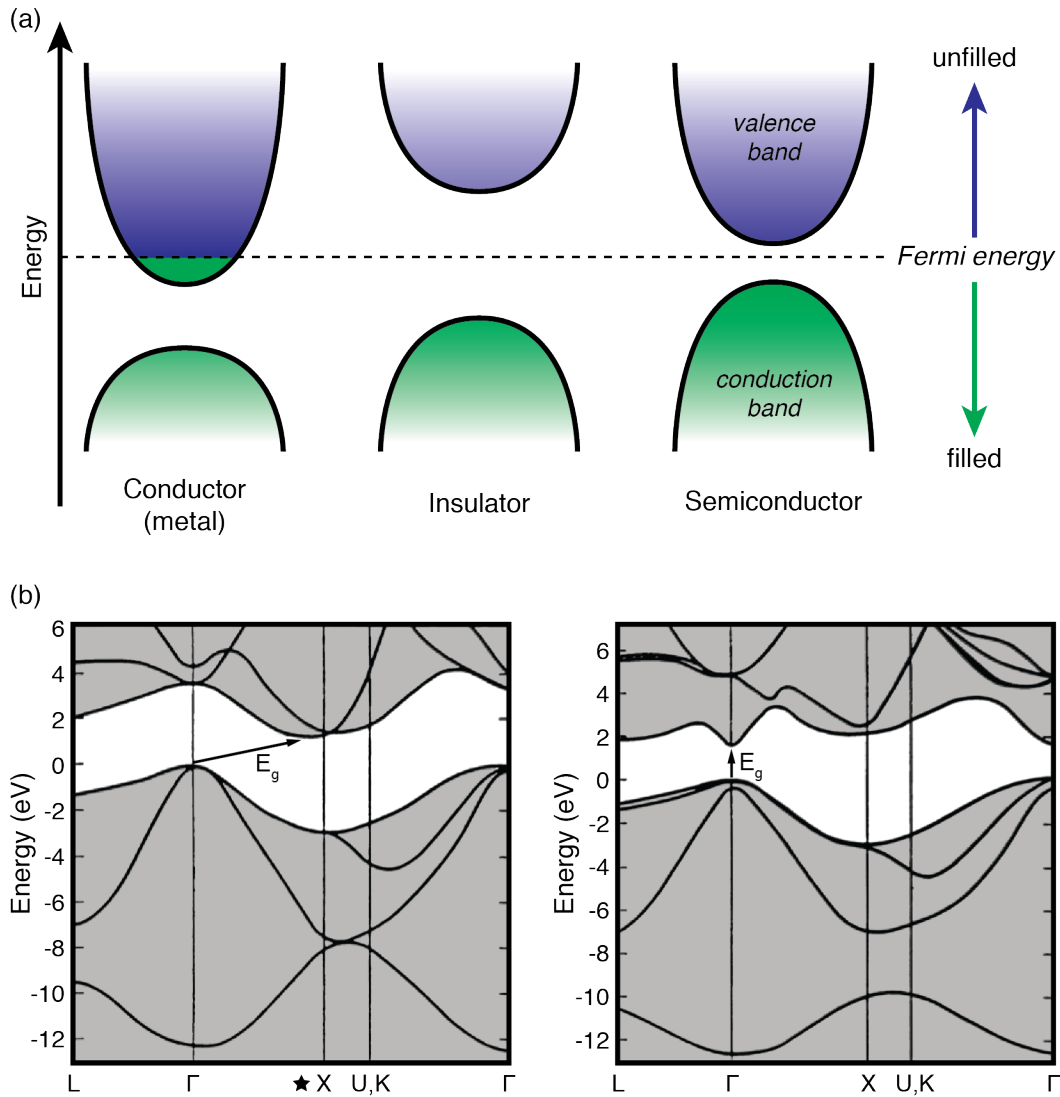
Figure B.1: (a) Band diagram of conductor, insulators, and semiconductors. Electrons fill energy levels up to the Fermi energy. (b) Band structure of the indirect semiconductor Si, and the direct semiconductor GaAs. Symbols along the bottom axes represent different values of $\mathbf{k}$ (or different positions in k-space). In the direct semiconductor the lowest energy transition occurs vertically in k-space, while in the indirect semiconductor the transition is offset in k-space. Modified from Ref. [123].

mass for the hole (the hole is assigned an effective mass, m^*, which depends of the curvature of the energy band). Analogous to the Bohr radius of the hydrogen atom, excitons posses a characteristic physical separation called the Bohr exciton radius a_b. In bulk Si, $a_b \simeq 4.3\,\mathrm{nm}$ and the binding energy is only $\sim 15\,\mathrm{meV}$ [77, 82, 124]. As a result, thermal energy is often enough break the bound state and separate the electron and hole.[4] This, combined with the long radiative lifetimes resulting from silicon's indirect bandgap, allow competing non-radiative decay mechanisms, such as Auger recombination and defect-state recombination, to dominate. Furthermore, at optical frequencies, the absorption cross-section of Si is very small, hundreds of times smaller than direct bandgap semiconductors (again stemming from its indirect bandgap). The cumulative result is poor photoluminescence (PL) efficiencies in bulk Si.

---

[4]Note: at room temperature thermal energy is $\sim 25\,\mathrm{meV}$.

Appendix C

Purcell effect

It is not immediately intuitive as to why one can observe the WGMs of an optical cavity, such as those discussed in Sec. 1.3.2.2, in an optical PL spectrum. A naive perspective of a resonance cavity would suggest that photons emitted at wavelengths that match the resonance wavelengths of the cavity would propagate for a longer time prior to emission than those that are emitted off-resonance. However, the spectroscopy methods used only provide information regarding the intensity (*i.e.,* total number of photons emitted over a period of time) of the light and not how long it was in the cavity (*i.e.,* the method is not lifetime resolved). This would result in a cavity emission spectrum identical to the free space spectrum; obviously this is not the case, evidenced by the visible WGMs in Sec. 3.4.1.

Explanation of this phenomenon is offered by the **Purcell effect**. First proposed by E.M. Purcell in 1946 (of whom the name in honour), the Purcell effect suggests that the spontaneous emission rate an emitter in an optical cavity is modified by the cavity. This effect can be enhancing or suppressing; the modified cavity rate W_{cav} is most commonly expressed as

$$W_{cav} = \frac{2\omega_0 \mu^2}{\hbar \varepsilon V_0} \xi^2 \frac{\Delta\omega_c}{4(\omega_0 - \omega_c)^2 + \Delta\omega_c^2} \tag{C.1}$$

where ω_c is the cavity resonance frequency, which has FWHM $\Delta\omega_c$ and mode volume V_0. ξ is a dipole orientation factor that averages to 1/3 in the case of randomly oriented dipoles, and μ is the transition dipole moment. The rate enhancement or suppression is given in terms of the **Purcell factor** [125]:

$$F_p = \frac{W^{cav}}{W^{free}} = \frac{3Q(\lambda/n)^3}{4\pi^2 V_0} \xi^2 \frac{\Delta\omega_c^2}{4(\omega_0 - \omega_c)^2 + \Delta\omega_c^2} \tag{C.2}$$

If $F_p > 1$ the rate is enhanced and if $F_p < 1$ the rate is suppressed. The primary result of Eq. (C.1) is that particles emitting on-resonance ($\omega_0 = \omega_c$) experience an enhanced spontaneous emission rate compared to those emitting off-resonance ($\omega_0 \neq \omega_c$). Thus, over a given collection time, more photons with wavelengths equal to the cavity resonances will have been emitted than those that are off-resonance. This results in an increased intensity signal for resonant-mode wavelengths, and thus visible WGMs in the PL spectrum. For more information regarding the Purcell effect in optical cavities see Refs. [125, 126].